

Design of Miniature Floating Platform for Marginal Fields

by

Sha Miao

B.S., Shanghai Jiao Tong University (2011)

Submitted to the Department of Mechanical Engineering
in partial fulfillment of the requirements for the degree of

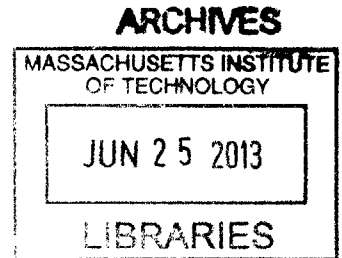
Master of Science in Mechanical Engineering

at the

MASSACHUSETTS INSTITUTE OF TECHNOLOGY

June 2013

© Massachusetts Institute of Technology 2013. All rights reserved.




Author


Department of Mechanical Engineering

May 20th, 2013

Certified by


Dick K.P. Yue
Philip J. Solondz Professor of Engineering
Thesis Supervisor

Certified by ..


Yuming Liu
Principal Research Scientist
Thesis Supervisor

Accepted by

David E. Hardt
Chairman, Department Committee on Graduate Students

Design of Miniature Floating Platform for Marginal Fields

by

Sha Miao

Submitted to the Department of Mechanical Engineering
on May 10th, 2013, in partial fulfillment of the
requirements for the degree of
Master of Science in Mechanical Engineering

Abstract

This thesis presents the design of a novel type of miniature floating offshore platforms with a heave plate attached at the keel, suitable for developing deep-water marginal fields. This design features a small displacement, easy fabrication, reduced cost and a favourable motion performance in waves. The design process includes the preliminary estimation, hydrodynamic analysis and hull optimization. A self-developed model “Discrete Vortex Ring Model” (DVRM) to efficiently estimate the viscous drag due to the vortex shedding of the oscillatory heave plate is presented in details. This new model DVRM combined with the standard radiation/diffraction code WAMIT is used to analyse the effect of different geometric parameters on the motion behaviour of the platform. Finally, these two models are integrated into a genetic optimization algorithm to obtain a final optimal design.

Thesis Supervisor: Dick K.P. Yue
Title: Philip J. Solondz Professor of Engineering

Thesis Supervisor: Yuming Liu
Title: Principal Research Scientist

Acknowledgements

I would like to express my deep gratitude to my advisor, Professor Dick K.P. Yue, for his continuous guidance and patience throughout the first two years of my graduate study. I have benefited greatly working with him not only from his profound knowledge and insightful research advice, but also from his research attitude. He helps me to gradually turn into a good researcher who should have critical and deep thinking, creativity, perseverance and systematicness. All of these would help me a lot in the rest of my graduate study and my future career.

In addition, I want to direct my thanks to Dr. Yuming Liu. Whenever I have questions and problems, he is there to help. Whenever I am frustrated by slow research progress, he is also there to encourage me and push me forward.

Gratitude also goes to all the members in Vortical Flow Research Laboratory for their tireless answering of my questions. I also would like to thank all my friends for their accompany and assistance.

Finally, I would like to thank my parents Wei MIAO and Qin XUE, for their endless love, understanding and support.

Contents

1	Introduction	21
1.1	Motivations	21
1.2	Wave loads on offshore platform	22
1.2.1	Linear wave-induced motion and loads	23
1.2.2	Partially nonlinear wave-induced motion and loads	24
1.2.3	Fully nonlinear wave-induced motion and loads	25
1.2.4	Viscous damping	25
1.3	Objectives and overview	28
2	Preliminary Design Considerations for the Mini-platform	31
2.1	Functions and configurations of the mini-platform	31
2.2	Estimation of the weight distribution of the mini-platform	34
2.2.1	Statistics of the weight distribution of the present mini-platforms	34
2.2.2	Topsides payload of the mini-platform (W_P)	34
2.2.3	Displacement of the mini-platform (Δ)	36
2.2.4	Hull weight of the mini-platform (W_H)	37
2.2.5	Ballast of the mini-platform (W_B)	38
2.2.6	Summary in the weight distribution of the mini-platform . . .	38
2.3	Estimation of the main dimensions of the mini-platform	38
2.3.1	Waterplane radius of the mini-platform (R_1)	39
2.3.2	Freeboard of the mini-platform (H_f)	39
2.3.3	Dimensions of the decks of the mini-platform	41
2.3.4	Draft of the mini-platform (H)	41

2.3.5	Dimensions of the heave plate of the mini-platform	42
2.3.6	Summary in the main dimensions of the mini-platform	42
2.4	Estimation of the inertial parameters of the mini-platform	43
2.4.1	Vertical centre of gravity of the mini-platform (VCG)	43
2.4.2	Radius of gyration of the mini-platform (R_g)	44
3	Hydrodynamic Models and Numerical Methods	45
3.1	Equation of motion of a floating body in regular waves	45
3.2	Potential flow model for the linear wave-body problem	47
3.2.1	Hydrostatic force of a freely floating body	48
3.2.2	Radiation problem of an oscillatory body in calm water	49
3.2.3	Diffraction problem of a fixed body in regular waves	50
3.2.4	Panel method for the radiation/diffraction problem	51
3.3	Vortex damping model for the viscous drag on the heave plate	54
3.3.1	Viscous drag of a 2D oscillatory thin plate	55
3.3.2	Viscous drag of a circular oscillatory thin plate	70
3.4	Solution to the motion equation in regular waves	76
3.4.1	Procedure of solving the motion equation	76
3.4.2	Derivation of the RAO	78
3.5	Motion Response in Ocean Environments	83
3.5.1	Description of ocean waves	83
3.5.2	Motions of general bodies in irregular waves	85
4	Conceptual Design and Analysis for the Mini-platform	87
4.1	Hull shape evolution of the mini-platform	87
4.1.1	Reduce the stiffness	89
4.1.2	Increase the added mass	89
4.1.3	Reduce the wave exciting force	90
4.1.4	Increase the viscous damping	92
4.2	An example of the mini-platforms compared with the spar in heave	93
4.2.1	Comparison in the RAO's	94

4.2.2	Comparison in the response in various sea-states	95
4.3	Effect of the geometric parameters of the mini-platform on heave . . .	97
4.3.1	Effect of the draft on heave	98
4.3.2	Effect of the axial distribution of the displacement on heave .	100
4.3.3	Effect of the radial distribution of the displacement on heave .	104
5	Hull Optimization for the Mini-platform	113
5.1	Optimization parameters for automatic generation of the hull shape .	114
5.2	Constraints for the mini-platform designs	117
5.3	Objective functions for the hull shape optimization	117
5.4	Optimization algorithm	118
5.4.1	Two concepts: Pareto frontier and ϵ -dominance	118
5.4.2	Optimization flow based on $\epsilon - MOGA$	121
5.5	Final hull shape for the mini-platform	124
6	Summary and Recommendations	129
6.1	Summary	129
6.2	Recommendations	131

List of Figures

2-1	General configuration and definition of the coordinate system for our miniature floating platform	32
2-2	Upper and lower bounds of the topside facility weight for typical floaters as a function of oil production rate, Gulf of Mexico (from Chakrabarti 2005; Vol.1, Ch.7, Sec.7.3)	35
2-3	Displacement/payload ratio as a function of the displacement for different types of floating platforms (from Wybro 2006)	37
2-4	Statistics of the diameters of the existing spars (Barton, n.d.)	40
3-1	Definition of the coordinate systems and sketch of body motions in six degrees of freedom, where $\xi_1 \sim \xi_6$ represent the displacement in the corresponding modes (from Newman 1977)	46
3-2	Sketch of the domain for the boundary value problem and the definition of the coordinate system, where S_F is the free surface, S_B is the wetted body surface, S_∞ is the surrounding surface at infinity and S_ϵ is an infinitely small surface surrounding a singular point. \vec{n} is the normal vector pointing out of the fluid.	52
3-3	A two dimensional infinitely thin plate with a length D oscillates in an unbounded and inviscid fluid.	55
3-4	A sketch of the distribution of the singularities on the plate and the free layers. The definition of Ψ is illustrated (adapted from Jones 2003)	58

3-5	Sequence of phase-averaged spanwise vorticity and velocity vectors showing vortex pair formation for $KC = 1.07$. The phase of the oscillation, θ , is given in degrees at the top of each frame. The contour represents the strength of the vorticity. Note the ejection of a single vortex pair in the positive x/η direction, which is a repeatable feature for each cycle (from Canals & Pawlak 2011).	64
3-6	The sketch of the “single vortex” approximation. The whole vortex structure is represented by a single point vortex connected to the separation point by a cut. \vec{X}_Γ denotes the location of the point vortex.	65
3-7	Non-dimensional vortex decay time scale t_d as a function of Re_ν , which is defined in terms of the vortex circulation. Error bars denote one standard deviation, and the grey shade of each symbol represents the value of KC for that experiment (from Canals & Pawlak, 2011)	67
3-8	Comparison of the time variation of the total circulation shed at one edge of the plate $\Gamma(t)$, the vortex shedding rate $d\Gamma(t)/dt$ and the total force coefficient $C(t)$ for $KC = 3.8$. The blue solid line is the result of VSM, the green solid line is from DVM and the red dash line is the experimental result adopted from Keulegan & Carpenter (1958)	68
3-9	The wake induced by the sinusoidal oscillation of a flat plate in an otherwise stationary fluid with $KC = 3.8$ and $V(t) = V_0 \sin(2\pi t/T)$. The positions of the plate and the free vortex sheets at times $t = 0.5KC, 1.25KC, 1.5KC, 2KC, 2.25KC,$ and $2.5KC$ are shown. The first row is the result adopted from Jones (2003). The second row is the result from our VSM. Our VSM uses a slightly different Kutta condition from the vortex sheet method used in Jones (2003).	69
3-10	Comparisons of the time variation of the total force coefficient $C(t)$ between DVM and experimental data for $KC = 1.7, 2.7, 4.7$ and 6.6 . The experimental data is retrieved from Keulegan & Carpenter (1958)	70

3-11	Difference in the average of peak values of the total force coefficient between DVM prediction and the experimental data for different KC 's. The experimental data is retrieved from Keulegan & Carpenter (1958)	71
3-12	Time variation of the force coefficient due to vortex shedding C_{FV} of an infinitely thin circular disk oscillating in an unbounded, inviscid, and otherwise undisturbed fluid based on DVRM, for $KC = 0.5, 1, 2, 3$ and 5	75
3-13	Time variation of the force coefficient due to vortex shedding C_{FV} of an infinitely thin circular disk oscillating in an unbounded, inviscid, and otherwise undisturbed fluid based on VRSM, for $KC = 0.5, 1, 2, 3$ and 5	76
3-14	Time variation of the force coefficient due to vortex shedding C_{FV} of an infinitely thin circular disk oscillating in an unbounded, inviscid, and otherwise undisturbed fluid for $KC = 0.5, 1, 2, 3$ and 5 (from De Bernardinis et al. 1981)	77
3-15	Comparisons in Drag Coefficients C_D as a function of KC number in log scale. The left figure is the result from the codes used in this thesis. The blue line is from VRSM, while the green line is from DVRM. The right figure is the result adopted from De Bernardinis, et al. (1981)	78
3-16	The flow chart of solving the dynamic motion equation of a floating body in regular waves in combination of the potential flow theory (WAMIT) and the vortex damping model (DVRM)	79
4-1	Variation of the heave added mass coefficient as a function of the dimensionless oscillation frequency and R_2/R_{avg} for a floating body composed of two cylinders with radius R_1 and R_2 respectively. The displacement and the draft of the body are fixed. R_{avg} is the radius of a circular cylinder with the same displacement and draft. The calculation results are from WAMIT.	90

4-2	Variation of the heave added mass coefficient as a function of $(R_2/R_{avg})^3$ for a floating body composed of two cylinders with radius R_1 and R_2 respectively. The displacement and the draft of the body are fixed. R_{avg} is the radius of a circular cylinder with the same displacement and draft. The red curve is the linear fitting line based on the scattered points obtained from WAMIT.	91
4-3	Sketch of the result of phase I of the hull evolution from a circular cylinder. We shrink the water-plane area, enlarge the keel radius and attach a heave plate at the keel to achieve soft stiffness and large added mass in heave motion.	92
4-4	The heave exciting force coefficients for different H_1/H from WAMIT. The black curve is the result for a circular cylinder with $H = 30 m$ and $R_{avg} = 11.3 m$. The zero force coefficients at low frequencies for the designs with a shoulder justify the cancellation effect of the exciting force due to this shoulder.	93
4-5	Sketch of the result of phase II of the hull evolution from a circular cylinder, to two cylinders with a high even shoulder, and to two cylinders connected by an oblique shoulder. Such a design utilizes the cancelling effect of the heave exciting force, and avoids an abrupt fluctuation in the cross section.	94
4-6	Variation of the heave exciting force coefficient for a floating body of two cylinders connected by a shoulder with different inclination α 's. The draft of the body H and the length of the lower cylinder H_3/H are fixed. The calculation results are from WAMIT.	95
4-7	Summary of all the phases of the hull evolution from a circular cylinder to the final configuration of the mini-platform	96
4-8	Sketch of the miniature platform and the spar with the same displacement $\Delta = 13,000 ton$ and the same draft $H = 30 m$	97

4-9	Comparison of the heave RAO of our mini-platform B and the spar A. The blue curve is the RAO without viscous damping for A. The green curve is the RAO without viscous damping for B. Both of these two curves are obtained from WAMIT. The red curve is the modified RAO with viscous damping defined in equation (3.107) based on the combination of WAMIT and DVRM. The red curve has a much smaller peak value compared with the other two curves.	98
4-10	Modified Pierson-Moskowitz spectrum used for design. The blue curve is for the operation condition with $H_s = 4.0\text{ m}$ and $T_p = 10.0\text{ s}$. The green curve is for the survival condition with $H_s = 12.0\text{ m}$ and $T_p = 14.0\text{ s}$	99
4-11	Variation of heave motion amplitude ξ_s/H_s for the mini-platform as a function of the total draft $H/\nabla^{1/3}$, where $\nabla = 13,000\text{ m}^3$, $H_1/H_2 = H_2/H_3 = 1$, $R_2/R_1 = 1.5$ and $R_3/R_2 = 1.3$.The results are from equation (3.122) based on WAMIT and DVRM.	100
4-12	Variation of the stiffness, added mass coefficients and resonant frequencies for the mini-platform as a function of the total draft $H/\nabla^{1/3}$, where $\nabla = 13,000\text{ m}^3$, $H_1/H_2 = H_2/H_3 = 1$, $R_2/R_1 = 1.5$ and $R_3/R_2 = 1.3$. The results are from WAMIT.	101
4-13	Variation of the wave exciting force coefficient for the mini-platform as a function of the total draft $H/\nabla^{1/3}$, where $\nabla = 13,000\text{ m}^3$, $H_1/H_2 = H_2/H_3 = 1$, $R_2/R_1 = 1.5$ and $R_3/R_2 = 1.3$.The results are from WAMIT.	102
4-14	Contours of the dimensionless heave motion amplitude ξ_s/H_s for the mini-platform as a function of H_1/H and H_3/H , while $\nabla = 13000\text{ m}^3$, $H/\sqrt[3]{\nabla} = 1.5$, $R_2/R_1 = 1.5$ and $R_3/R_2 = 1.5$. The results are from equation (3.122) based on WAMIT and DVRM.	103
4-15	Contours of the heave added mass coefficients as a function of H_1/H and H_3/H , while $\nabla = 13000\text{ m}^3$, $H/\sqrt[3]{\nabla} = 1.5$, $R_2/R_1 = 1.5$ and $R_3/R_2 = 1.5$. The data is obtained from WAMIT.	104

4-16	Contours of the dimensionless stiffness as a function of H_1/H and H_3/H , where $\forall = 13000 \text{ m}^3$, $H/\sqrt[3]{\forall} = 1.5$, $R_2/R_1 = 1.5$ and $R_3/R_2 = 1.5$. The results are from WAMIT.	105
4-17	Contours of the wave exciting force coefficients as a function of H_1/H and H_3/H , while $\forall = 13000 \text{ m}^3$, $H/\sqrt[3]{\forall} = 1.5$, $R_2/R_1 = 1.5$ and $R_3/R_2 = 1.5$. The results are from WAMIT.	106
4-18	Contours of the dimensionless heave motion amplitude ξ_s/H_s for the mini-platform as a function of R_2/R_1 and R_3/R_2 , while $\forall = 13000 \text{ m}^3$, $H/\sqrt[3]{\forall} = 1.5$, $H_1/H = 0.55$ and $H_3/H = 0.3$. The results are from equation (3.122) based on WAMIT and DVRM.	107
4-19	Contours of the added mass coefficient for the mini-platform as a function of R_2/R_1 and R_3/R_2 , while $\forall = 13000 \text{ m}^3$, $H/\sqrt[3]{\forall} = 1.5$, $H_1/H = 0.55$ and $H_3/H = 0.3$. The results are from WAMIT.	108
4-20	Contours of the viscous damping coefficients for the mini-platform as a function of R_2/R_1 and R_3/R_2 , while $\forall = 13000 \text{ m}^3$, $H/\sqrt[3]{\forall} = 1.5$, $H_1/H = 0.55$ and $H_3/H = 0.3$. The results are from DVRM.	109
4-21	Contours of the dimensionless softness for the mini-platform as a function of R_2/R_1 and R_3/R_2 , while $\forall = 13000 \text{ m}^3$, $H/\sqrt[3]{\forall} = 1.5$, $H_1/H = 0.55$ and $H_3/H = 0.3$. The results are from WAMIT.	110
4-22	Contours of the dimensionless resonance frequencies in heave for the mini-platform as a function of R_2/R_1 and R_3/R_2 , while $\forall = 13000 \text{ m}^3$, $H/\sqrt[3]{\forall} = 1.5$, $H_1/H = 0.55$ and $H_3/H = 0.3$. The results are from WAMIT.	111
4-23	Contours of the wave exciting force coefficients for the mini-platform as a function of R_2/R_1 and R_3/R_2 , while $\forall = 13000 \text{ m}^3$, $H/\sqrt[3]{\forall} = 1.5$, $H_1/H = 0.55$ and $H_3/H = 0.3$. The results are from WAMIT.	112
5-1	Framework of the parametric optimization of hull shape	114
5-2	Setup of the mini-platform for the hull optimization.	115

5-3	Illustration of the Pareto frontier. The black circles represent the feasible designs, the green circles are designs of Pareto frontiers, and the red crosses denote the infeasible designs violating the constraints. . .	119
5-4	Illustration of the concept of usual-dominance and ϵ -dominance (from Deb et al., 2003)	120
5-5	Illustration of the single point cross over for two parents to generate two children	122
5-6	Illustration of the procedure of ϵ -MOEA (from Deb et al., 2003) . . .	124
5-7	Final Pareto frontier of the Multi-objective optimization for the hull shape of the mini-platform when the population number reaches 350. The objective functions are evaluated based on the combination of WAMIT and DVRM.	125
5-8	Hull shape of the selected designs from the final Pareto frontier of a population of 350.	126

List of Tables

2.1	Statistics of the weight distribution of the payloads, hull weight and displacement of the present mini-platforms, where W_P is the topsides payload, W_H is the self-weight of the hull, and Δ is the displacement (from Hudson & Vasseur 1996; Wilhoit 2010; Kibbee et al. 1999; Kibbee & Snell 2002; Koon et al. 2002; Ronalds 2002; Cermelli et al. 2004)	34
2.2	Statistics of the draft H of the present mini-platforms (from Wilhoit 2010; Kibbee et al. 1999; Kibbee & Snell 2002; Koon et al. 2002; Cermelli et al. 2004)	41
2.3	An example of the estimation of the VCG of the platform based on the weight distribution of different components at the initial stage, where the coordinate	43
4.1	Dimensions of the spar A and newly designed mini-platform B.	94
4.2	The characteristic parameters of the design condition of the sea-states. H_s is the significant wave height. T_p is the peak period of the wave spectrum. The data is retrieved from ITTC.	95
4.3	Comparison of the significant heave motion height ξ_s in various sea-states for spar A and mini-platform B, where GM denotes the hydrostatic metacentric height, and T_n is the natural periods in heave. The result is obtained from the combination of WAMIT and DVRM.	96
5.1	Upper and lower limits of the five free optimization variables to describe the hull shape	116

5.2 Dimensions and optimization objectives of the selected designs of the mini-platforms from the final Pareto frontier of a population of 350. . 126

Chapter 1

Introduction

1.1 Motivations

Humans' demand for hydrocarbons is expected to increase by 5% per year for the following decades, but very large oil and gas fields are fewer and fewer. Therefore, oil and gas companies are transitioning to look for means of developing their proven smaller reserves, which are so-called "marginal fields". A lot of such reserves have already been discovered in the deep water of Gulf of Mexico recently. However, the expenses of a stand-alone deep-water field development, including a platform and pipeline infrastructure, are usually beyond the value of the oil or gas it contains. Nowadays, providing surface support to deep water developments is mainly achieved by three types of platforms, all of which are costly.

Semi-submersible platforms are moored floating structures composed by multiple columns connected by pontoons. This kind of platforms achieves its stability by large displacement, normally exceeding 20,000 tons. Therefore, such platforms can support a large payload, but at the same time their cost is high. In addition, their large displacement requires very large mooring system, which increases significantly in size and cost with water depth.

Spars are a hollow vertical cylindrical structure moored to the sea bed. Such platforms usually have a very deep draft to minimize heave motion, but this also increases the system cost. In addition, another inherent problem of such concept is that the

cylinder suffers greatly from Vortex Induced Motions (VIM) in the current. These induced oscillations would reduce the fatigue life of the mooring system, resulting in operational concerns. One of the most common mitigation devices is strake. But strakes increase the wetted surface of the platform and the strength requirements of the mooring system. The spar installation and fabrication costs are also high.

Finally, tension leg platforms (TLP) have also been widely used to support deep water facilities in depth extending to almost 5,000 ft. TLPs are connected to the sea-bed by a set of vertical steel tendons, like an inverted pendulum. These tensioned tendons limit the heave and pitch motion very well. Due to the motivation from the marginal fields, a lot of mini-TLPs were invented, such as Seastar mini-TLP and Modec mini-TLP. However, TLP cannot be extended to the ultra deep water greater than 5,000 ft and the installation of these tendons is very expensive. In addition, the tendons are subject to Vortex-Induced Vibrations (VIV), which makes their design challenging.

The existing floaters are all very large and costly. Marginal fields cannot support these costs. This motivates the industry to seek for a clever design of a novel miniature floating platform with loose mooring systems, of which the displacement is around 10^4 ton. In addition, such mini-platforms should also have a good motion performance in waves. However, it is quite challenging to achieve both goals at the same time. This thesis would focus on how to find such an economic but also safe design.

1.2 Wave loads on offshore platform

It is essential to predict the wave-induced loads and motion in both design and operation of the offshore platforms. Motions of floating platforms usually involve six degrees of freedom. The rigid-body translatory motions are surge, sway, and heave. The angular motions are referred as roll, pitch and yaw.

To date, the majority of research has assumed that the water can be considered as incompressible and inviscid, and that the flow around the body remains irrotational. Under this assumption, the Laplace equation is valid everywhere in the fluid domain

and the hydrodynamic forces acting on the body can be considered as the solution to the boundary value problem. However, this is not implying that viscous effects are not important. On the contrary, for certain phenomena they are dominant. However, the inviscid fluid problem is an order of magnitude easier to solve and therefore has been the basis for much of the research in the area. For many types of problems and geometries the inviscid assumption gives quite an acceptable accuracy (Beck 1994).

1.2.1 Linear wave-induced motion and loads

Under operational conditions when the amplitudes of incident waves and body motions are relatively small, linear theory in the frequency domain generally gives good predictions for wave body interactions. Based on the linear wave theory, a sea state is usually described by a wave spectrum and a floating body's response to this random sea can be approximated by superposing the body's response to each regular incident wave component in the spectrum (St. Denis & Pierson 1953). The solution of regular incident wave interactions with floating bodies can be obtained by solving the boundary value problem which can be further split into seven sub-problems: a radiation problem associated with forced harmonic oscillations in six modes of rigid body motion, and a diffraction problem when the body is fixed in incident regular waves. In each of these sub-problems, a velocity potential is found as the solution of the Laplace equation subject to a body boundary condition applied on the mean wet surface, a sea-bottom condition, the classical linearized free surface condition and a radiation condition at far field. For a general body shape, numerical schemes are usually used, including finite difference, finite element, finite volume, and boundary element methods. Among all these numerical schemes, the potential-flow based boundary element methods (panel methods) using a Green function technique have gained great popularity due to their efficiency, accuracy, and flexibility (King 1987; Newman & Sclavounos 1988; Newman 1992). From the linear theory, wave-induced body motion reserves wave frequency and has the motion amplitude linearly proportional to the incident wave amplitude.

For the linear problems, the time-domain and frequency-domain solutions are

complementary via Fourier transforms. However, the conventional frequency-domain approach is computationally much faster than the time-domain approach. In addition, the linear method in frequency domain can capture most of the leading order effects in a mild sea condition. Therefore, it is widely used to explore the design space at the preliminary design phase, to understand the system responses and to obtain fundamental insights into the optimization of the systems' design. Since this thesis focuses on the concept design and preliminary optimization of a novel floating platform, the standard linear Radiation/Diffraction theory in the frequency domain is used.

1.2.2 Partially nonlinear wave-induced motion and loads

The biggest limitation of a frequency domain analysis based on the linear wave and linear dynamics theory is that the amplitudes of ambient wave and body motions have to be small compared to the ambient wavelength. However, extreme wave environments under nonlinear effects could also be of importance.

The most common way to solve the nonlinear wave body interaction problem is to use perturbation analysis with the ratio of wave amplitude and wavelength as a small parameter. If we extend the linear theory to the second order, i.e., the free surface and body boundary conditions are satisfied up to the second order in the wave steepness, we could obtain nonlinear wave forces of sum- and difference-frequencies. If these frequencies are close to the natural frequencies of the system, resonance would also occur (Faltinsen 1990).

There are other studies taking partial nonlinearity effects into account in the wave-body interactions. One is the body-exact numerical method which is usually for practical problems involving large-amplitude body motions but relatively small incident and diffraction waves. The body boundary condition is implemented on the exact instantaneous wet body surface while the free surface condition is linearized at the undisturbed water surface (Lin & Yue 1991; Faltinsen & Chezhian 2005). The other is called "weak-scatter theory". This theory linearizes the free surface boundary condition on the incident wave profile, and still satisfies the exact body

boundary condition. This is one step further than the body-exact theory, but still has limitations on the nonlinearity of disturbance flow (Pawlowski 1992; Huang 1997). Since the body boundary condition is satisfied on the instantaneous wet surface, time domain analysis is the convenient alternative, but much more time consuming in computation.

1.2.3 Fully nonlinear wave-induced motion and loads

For problems like slamming, green water on deck and wave over-topping, fully nonlinear numerical simulation is required. However, because of the computational cost and complexity in modelling the multi-scale nonlinearities, such three-dimensional fully nonlinear results for general bodies are still limited. One of the most popular methods is the mixed-Eulerian-Lagrangian (MEL) approach combined with a boundary element method (BEM). At each time step, the BEM is first used to solve the BVP, and the MEL is then used to update the nonlinear free surface (Dommermuth & Yue 1987; Liu, Xue & Yue 2001). Finite difference methods or finite volume methods, which are much more computationally expensive than the BEMs, are at present not practical in the study of fully nonlinear wave-body interaction for the design of offshore structures.

1.2.4 Viscous damping

Viscous damping is of importance in the design of offshore platforms because it can be utilized for suppressing the motion of the platform. However, the state of the art in calculating the viscous loads on offshore structures is not satisfactory. Traditionally, Morison's equation (Morison et al. 1950) has been widely used to calculate wave and current loads on cylindrical structures. The inertia and drag coefficients have to be empirically or experimentally determined. In addition, Morison's equation cannot predict the oscillatory forces due to vortex shedding. This motivates numerous researches in developing more rational methods for estimating the viscous damping effects.

The simplest model to use is a single-vortex model. This is an inviscid method that models the flows with thin vortex sheets separated from sharp corners at high Reynolds numbers and low Keulegan Carpenter numbers (KC). This model represents the vortex sheet by a single vortex and a cut joining this single vortex and the adjacent separation point. Brown & Michael (1955) first applied the condition of total zero force on the sum of the single vortex and the cut to determine the location of the vortex. Kutta condition is satisfied at the separation point to determine the strength of the vortex. Faltinsen & Sortland (1987) used a similar idea to study drag coefficients for an arbitrary two-dimensional bodies with sharp corners and obtained good results compared to the experiments. Stiassnie et al. (1984) applied the single vortex method on oscillating problems to estimate the energy dissipation due to the vortex shedding at the lower sharp edge of a vertical plate in waves. They assumed only one pair of vortices shed per period and neglected the influence of previously shed vortices, focusing on one half cycle only. The result has the same trend compared to the experiment, but the error is not trivial. In addition, his method is limited to 2D simple geometry with known analytical solution for the same problem with no vortex. Graham (1977) also attempted to apply this simple method on more general oscillatory flow, but the calculation becomes invalid if the vortex shedding rate changes the sign. Long time calculation will lead to a divergent result.

Graham (1980) later carried out a semi-analytical analysis for $KC \rightarrow 0$. He assumed that the vortex flow for a small KC number depends on the local flow around the sharp edge only. He found out a qualitative relation between the drag coefficient and the KC number. However, the analysis is for the 2D problems and only gives qualitative results.

Usually Reynold's number associated in hydrodynamic problems for marine structures is very large. Therefore, when vortex shedding occurs, the boundary layer is very thin. This motivates researchers to use vortex sheet method to model the separation phenomenon. A vortex sheet is actually a line of distribution of vorticity. For 2D problems, Jones (2003) proposed a general computational method for the flow separation of a plate based on the work of Krasny (1991). He distributed vortex blobs

on both sheets and the plate, and did not use conformal mapping method which is widely used for solving 2D problems. Hence such method can be generalized to tackle 3D problems. However, his method cannot do the simulation for long time. As for 3D axisymmetric problems, not too much work has been done until now. De Bernardinis et al. (1981) and Nitsche & Krasny (1994) applied the vortex ring method to some axisymmetric problems. For 3D problem, vortex sheet method is commonly used in BEM to distribute the dipoles or vorticity on body and the vortex sheet. Kutta condition is applied on each time step to determine the strength of the newly shed sheet. Such scheme can predict the drag coefficients accurately but very time-consuming.

In addition to the numerical methods, another popular approach is to measure the drag coefficients by experiments and plug them into the Morison's equation. As for experiments, Keulegan & Carpenter (1958) measured the force of a fixed 2D thin plate in oscillating flow and found that the drag coefficient is a function of KC number. Very recently, Canals and Pawlak (2011) also studied this 2D problem experimentally, but focusing more on the vortex dynamics. He et al. (2008) studied the hydrodynamics of a thin 3D circular plate oscillating by experiments, and found that the viscous damping coefficient depends on both KC number and the diameter-thickness ratio of the plate. However, we should note that it is impossible to do experiments to obtain the viscous damping force for every case of the design at the initial stage.

As we can see, the separated flow around the marine structure is such a complicated phenomenon that a general feature of the existing methods is that a simple model will have deficiencies, therefore leading to more complicated numerical models. The result of this trend is that one ends up wanting to solve numerically the Navier-Stokes equations for turbulent flows. However, the solution of NS equations with turbulence is still unrealistic (Rodi 1985). It is not a wise choice to spend much time and computation power only to obtain a drag coefficient while all the other major hydrodynamic coefficients can be obtained by standard radiation/diffraction method within a minute. So rather than following the trend with a more and more complicated model, one may be attempted to go the opposite way and try to find a simple model which can capture the important features of separated flow.

In this thesis, we propose a simple model based on the single vortex idea to estimate the drag coefficient due to the vortex shedding very quickly, both for 2D and 3D axisymmetric cases. The results agree with the experiments satisfactorily. We then combine this simple model with the standard Radiation/Diffraction method to obtain an optimum design of a miniature offshore platform for marginal fields.

1.3 Objectives and overview

The research objectives of this thesis would include the following three parts. The first thing is to come up with a new design of a mono-column mini-platform from hydrodynamic analysis. Since we hope to utilize the viscous damping effects to improve the motion behaviour of the platform in waves, a quick model accounting for this damping effects would be developed. Finally, we would combine the hydrodynamic analysis and viscous damping model to carry out the optimization to obtain the optimum design.

This thesis is organized into six chapters.

Chapter 1 provides an introduction of the motivation and research goals of the present work. A brief literature review of the calculation of the hydrodynamic loads is also given.

Chapter 2 would concentrates on some preliminary considerations on design, including the estimation of the main dimensions and weight distribution.

In Chapter 3, we would present the hydrodynamic models and methods used for design in details: the linear Radiation/Diffraction method (WAMIT), and the newly developed vortex damping model. For the viscous damping problem, we would first discuss the widely-used vortex sheet method in 2D problems, and then focus on the self-developed new model, called “Discrete Vortex Method” (DVM). Then this new model will be extended to 3D axisymmetric problems, called “Discrete Vortex Ring Method” (DVRM), and compared with the widely-used vortex ring sheet method. Finally, we combine this new model DVRM with WAMIT to derive the solution to the hydrodynamic equation of motion.

Chapter 4 applies the models and methods to the design of hull shape of our mini-platform. We first discuss the evolution of the hull shape of our platform from a spar with the same displacement and draft. Next, we presents an initial design of our platform compared with the spar in the heave motion quantitatively to show the advantage of our design, using the combination of WAMIT and DVRM. Finally, how different geometric parameters influence the motion performance is discussed to provide some guides for the following optimization.

Next in Chapter 5, we use a multi-objective genetic optimization algorithm to find the optimal hull shape for our mini-platform. The combination of WAMIT and DVRM is integrated into the optimization algorithm to achieve an efficient and automatic calculation.

Finally Chapter 6 summarizes the whole thesis and provides some recommendation for the future work.

Chapter 2

Preliminary Design Considerations for the Mini-platform

This chapter will discuss several important considerations in the initial design phase. Our objective is to design a mono-column floating platform for deep water with displacement around 10^4 ton and satisfactory motion performance. For floating structures, in addition to the hydrodynamic response in waves, the weight control and stability are also key design challengers. Therefore, before we perform any hydrodynamic analysis, the first job is to determine the size and weight distribution of the platform to guarantee that such a design satisfies the hydrostatic stability criteria and is compatible with its function.

2.1 Functions and configurations of the mini-platform

In the design of a platform, a clear knowledge of the functions should be in hand. This will strongly influence the configuration of the platform. Production, storage, drilling and workover are the four major functions currently performed by floating platforms (Chakrabarti 2005; Vol.1, Ch.7, Sec.7.2.2). Since we target at designing a floating platform with a displacement around 10,000 ton, the carrying capacity of our platform is limited. Therefore, the function of our platform is defined for production only, similar to mini-TLPs (Ronalds 2002). The oil production for the

present miniature platforms usually ranges from 30 ~ 40k barrels per day (bpd) (Wilhoit 2010; Ronalds 2002). Here we initially set the oil production rate for our mini-platform to be 30k bpd.

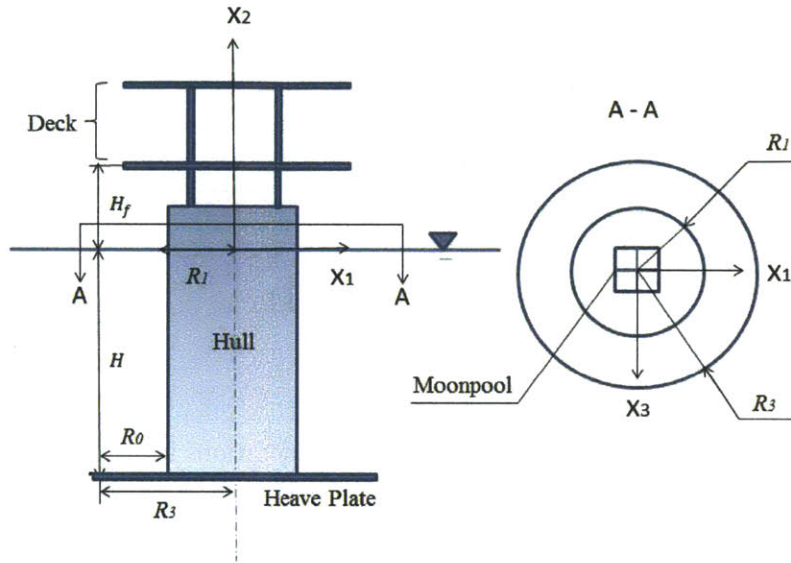


Figure 2-1: General configuration and definition of the coordinate system for our miniature floating platform

The general configuration of our platform is shown in Figure 2-1. We define a coordinate system with the origin at the mean waterline and the vertical coordinate x_2 coinciding with the axis of symmetry. As can be seen, the mini-platform is composed of three parts: deck structures above the waterline, a hull with a moonpool inside, and a heave plate attached at the bottom of the hull. The topsides deck is a multi-level structure supported by the submersible part. It is mainly used for supporting the weights due to the facilities for oil production. The submersible part is called “hull”. For such kind of single-column floating platforms, there is normally an opening with several well slots inside the hull, called “moonpool” (Chakrabarti 2005; Vol.1, Ch.7, Sec.7.7). The function of this moonpool is to allow technicians to lower pipes and instruments into the sea. Finally, the thin plate attached at the keel is called “heave plate”, which is a commonly used device to mitigate the motion amplitude of the

platform.

The main dimensions of the platform is also provided in Figure 2-1.

- H_f is called “freeboard”, which is the distance between the waterline and the lowest deck level;
- H is the total draft of the submersible part of the platform;
- R_1 is the radius of the water-plane area;
- R_3 is the radius of the heave plate;
- R_0 is the dimension of the extension of the heave plate relative to the hull.

The weights of the different components of the platform are defined as follows:

- W_P is the topsides payload, representing the sum of the carrying capacity of a platform and the self-weight of its deck structures;
- W_H is the weight of the hull;
- Δ is the displacement, a representative of the scale of a platform. It refers to the total mass of the sea water displaced by the submersible hull.

Another two important parameters reflecting the inertia of the platform are also in need at the initial stage.

- VCG stands for the vertical coordinate of the centre of gravity;
- R_g is the radius of gyration for pitch (or roll), which is usually used to describe the mass distribution around the axis of symmetry;

In the following sections, we will discuss how to distribute weight among different configurational components, how to estimate the main dimensions, and how to obtain the parameters of inertia.

Name	Type	W_P/t	W_H/t	Δ/t
Minifloat IV	semi	4,000	–	12,698
Morpeth	mini-TLP	3,175	2,540	10,605
Allegheny	mini-TLP	3,719	2,359	10,605
Typhoon	mini-TLP	3,810	2,817	12,157
Prince	mini-TLP	5,533	3,175	13,097
Matterhorn	mini-TLP	12,208	5,352	14,881
Marco Polo	mini-TLP	12,700	5,216	24,947

Table 2.1: Statistics of the weight distribution of the payloads, hull weight and displacement of the present mini-platforms, where W_P is the topsides payload, W_H is the self-weight of the hull, and Δ is the displacement (from Hudson & Vasseur 1996; Wilhoit 2010; Kibbee et al. 1999; Kibbee & Snell 2002; Koon et al. 2002; Ronalds 2002; Cermelli et al. 2004)

2.2 Estimation of the weight distribution of the mini-platform

2.2.1 Statistics of the weight distribution of the present mini-platforms

There are numerous miniature platforms to date and most of them are mini-TLPs. Table 2.2.1 shows the statistics of weight distribution for the present miniature platforms (from Hudson & Vasseur 1996; Wilhoit 2010; Kibbee et al. 1999; Kibbee & Snell 2002; Koon et al. 2002; Ronalds 2002; Cermelli et al. 2004)). These data can provide us a guide for the initial estimation. In the following context in this section, emphasis is put on the estimation of W_P , W_H and Δ .

2.2.2 Topsides payload of the mini-platform (W_P)

The topsides payload is the total weight above the waterline, which measures the carrying capacity of a platform. It can be further divided into three parts: facilities weight, drilling or workover weight, and the deck structure weight (Chakrabarti 2005; Vol.1, Ch.7, Sec.7.3).

Facility weight of the mini-platform

Facility weights represent the maximum fixed plus the variable payload weights carried by the hull, normally excluding drilling. These weights can be estimated according to the export production of the platform. Figure 2-2 shows the typical range of facility weights for the Gulf of Mexico (GOM) floaters as a function of oil production rate (Chakrabarti 2005; Vol.1, Ch.7, Sec.7.3).

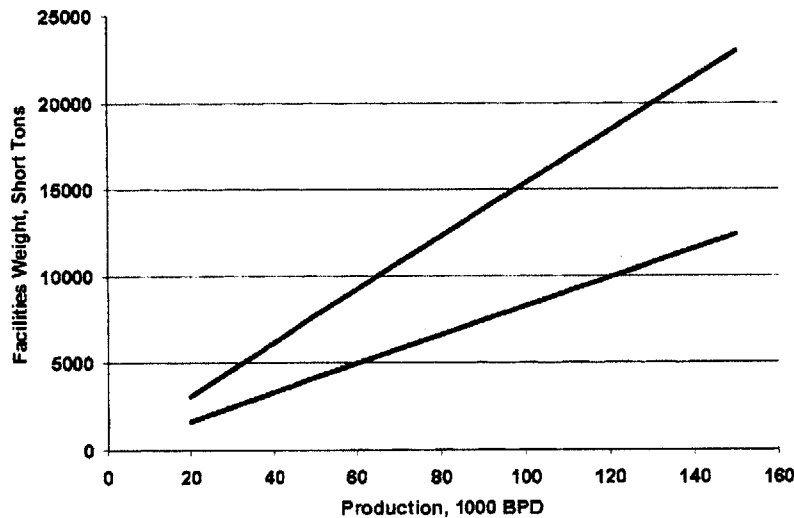


Figure 2-2: Upper and lower bounds of the topside facility weight for typical floaters as a function of oil production rate, Gulf of Mexico (from Chakrabarti 2005; Vol.1, Ch.7, Sec.7.3)

The oil production rate in our case is 30 k bpd, so the facility weight can be estimated to be around 2,500 st, i.e., 2,300 ton.

Drilling or workover weights of the mini-platform

Drilling or workover weights are the self-weights of the drilling or workover rigs. Since our platform is designed for production instead of drilling or completion, we can ignore this weight.

Deck structure weight of the mini-platform

Usually the self-weight of the deck structure is 30 ~ 40% of the weight of facilities and drilling equipment (Chakrabarti 2005; Vol.1, Ch.7, Sec.7.3). Therefore, this weight item is at least around 700t.

The sum of the above three items arrives at a total weight of the topsides around 3,000 ton. We can also justify the reasonableness of this value from the statistics in Table 2.2.1 and the principles of stability for different types of platforms. Table 2.2.1 shows that for the present mini-platforms (mini-TLPs and a semi-submersible) with a displacement less than 13,000 ton, their payloads normally range from 3,000 to 4,000 ton. Since the stability of the TLPs is mainly achieved by tendons, and that of semi-submersibles is by the restoring moment of the multiple columns, i.e., “column-stabilized”, both of them allow the centre of gravity above the centre of buoyancy. Contrarily, for single-body floating platforms like Spars, or our mini-platform, the gravity centre must be lower than the buoyancy centre to guarantee enough stability. This implies that TLPs have the highest gravity centre, semi-submersibles come the second, and Spars own the lowest in general. Therefore, TLPs generally have a relatively larger payload-displacement ratio compared to other types of platforms. In other words, with the same displacement, mini-TLPs hold a larger topsides capacity than our platform. Hence 3,000 ton should be a reasonable estimation for the topsides payload in our case if we assume the displacement is also no more than 13,000 ton.

2.2.3 Displacement of the mini-platform (Δ)

Our design purpose is a miniature platform, so the displacement of the platform should be limited. Referring to the previous statistics in Table 2.2.1, we can see that most of the mini-platforms have a displacement of 10,000 ~ 15,000 ton. Similarly, we should confine our platform within this range.

We can also estimate the displacement according to the displacement/payload ratio and the topsides payload obtained in the previous subsection.

Figure 2-3 (from Wybro 2006) shows that for conventional platforms, TLPs own

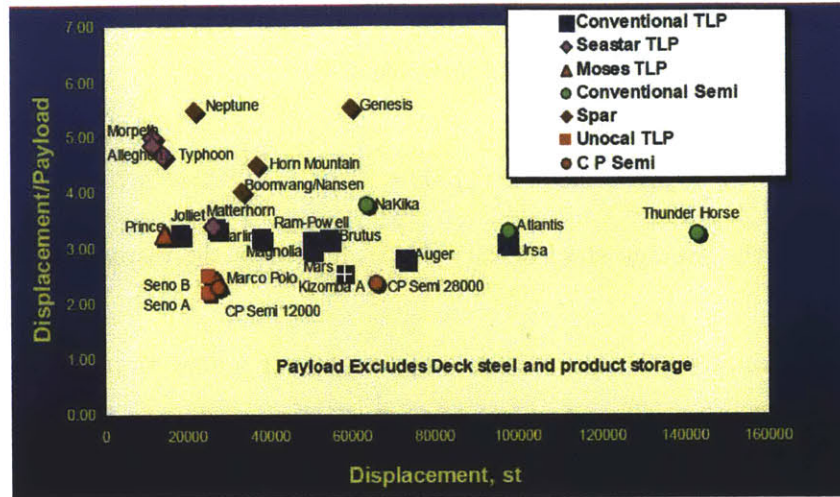


Figure 2-3: Displacement/payload ratio as a function of the displacement for different types of floating platforms (from Wybro 2006)

the smallest displacement/payload ratio, semi-submersibles take the second place, and Spars have the largest ratio. This is consistent with the previous statement inferred from the principles of stability of these three types of platforms. We can also see from Figure 2-3 (Wybro 2006) that for mini-platforms with displacement below 20,000 ton, mainly mini-TLPs, their displacement/payload ratio are mostly near 5.0. Therefore, it is reasonable to assume the ratio of our platform slightly larger, about 5 ~ 6. The payload (excluding deck steel) for our platform is 2,300 ton, so the displacement Δ should be around 11,500 ~ 13,800 ton. Here we can set it to be 13,000 ton.

2.2.4 Hull weight of the mini-platform (W_H)

In practice, the approaches of estimating the hull steel weight for a semi-submersible and a TLP in the initial design stage are similar (Chakrabarti 2005; Vol.1, Ch.7, Sec.7.5-7.6). Here we also apply this estimation approach to our mini-platform. At this stage we know little about the structure of the hull, one common way is to use a steel density for the enclosed hull volume. For semi-submersibles, values of between $10 \text{ lb}/\text{ft}^3$ in the upper sections to $15 \text{ lb}/\text{ft}^3$ in the pontoons are typical (Chakrabarti 2005; Vol.1, Ch.7, Sec.7.5). Here we can use an averaging density of $13 \text{ lb}/\text{ft}^3$, i.e.,

$\rho_s = 0.208 t/m^3$, and ignore the volume between the topsides and mean water line which is small compared to the submersible part.

$$W_H = \rho_s \forall = 0.208 \times (11500 \sim 13800) = 2392 \sim 2870.4 \text{ ton} \quad (2.1)$$

where ρ_s is the average steel density of the hull; \forall is the displaced volume of the platform.

In addition, from Table 2.2.1, the hull weights for miniature platforms usually lie at 2000 \sim 3000 ton. Therefore, we can set W_H to be 2800 ton in the initial design phase.

2.2.5 Ballast of the mini-platform (W_B)

The ballast is needed to adjust the vertical centre of gravity to ensure enough stability. The weight of the ballast W_B should be the difference between the total loads exerted on the platform and the displacement Δ .

2.2.6 Summary in the weight distribution of the mini-platform

In summary, the weight distribution would be:

- (1) Δ : 13,000 t
- (2) W_P : 2,500 t
- (3) W_H : 2,800 t

2.3 Estimation of the main dimensions of the mini-platform

Having obtained the weight distribution of the platform, we pay our attention on the dimensions defined in section 2.1 in this section.

2.3.1 Waterplane radius of the mini-platform (R_1)

As mentioned earlier, such kind of mono-column platforms normally have a moonpool in the centre of the hull (see Figure 2-1). For mini platforms, well counts are generally 4 – 6 (Kibbee et al. 1999). Spars can be referred to to estimate the size of the centerwell. To date, all the centerwells of spars have been square, leading themselves to 4×4 , 5×5 , or 6×6 well slots. Slot spacing for existing centerwells ranges from $8ft$ to $14ft$. The size increases with water depth because of the higher tensions required. The recommended spacings for spars would be (Chakrabarti 2005; Vol.1, Ch.7, Sec.7.6):

Up to $3000ft$ water depth	$12ft$
$3000 - 5000ft$	$13ft$
Greater than $5000ft$	$14ft$ or more

For our platform, we assume a moonpool of 2×2 square and use $12ft$ as the slot spacing. Then the dimension of the centerwell is around $2 \times 12ft \simeq 7.2m$. Based on the Figure 2-4 (Barton, n.d.), the diameter of the spar is usually 2 times the dimension of the centerwell. Therefore, R_1 should be at least 7 m.

2.3.2 Freeboard of the mini-platform (H_f)

Freeboard H_f is defined as the distance from the mean water line to the lowest deck level (see section 2.1). The estimation of this dimension is determined by the estimation of the “Air Gap (H_a)”. Air gap means the distance between the highest wave crest and the deck. For the US GOM conditions, API RP2A (1993, 2000) recommends that this air gap should be a minimum of 5 ft, i.e., $H_a = 1.5$ m. The highest wave, or the crest level above still water, is specified with the design wave height H_s . For deep water, we usually estimate the crest level above mean water line to be $\frac{2}{3}H_s$ (Chakrabarti 2005; Vol.1, Ch.7, Sec.7.5). For survival condition (100-year return period), we consider the significant wave height (H_s) to be 12.0 m, and the peak wave period (T_p) to be 14.0 s. Thus the extreme crest elevation H_c :

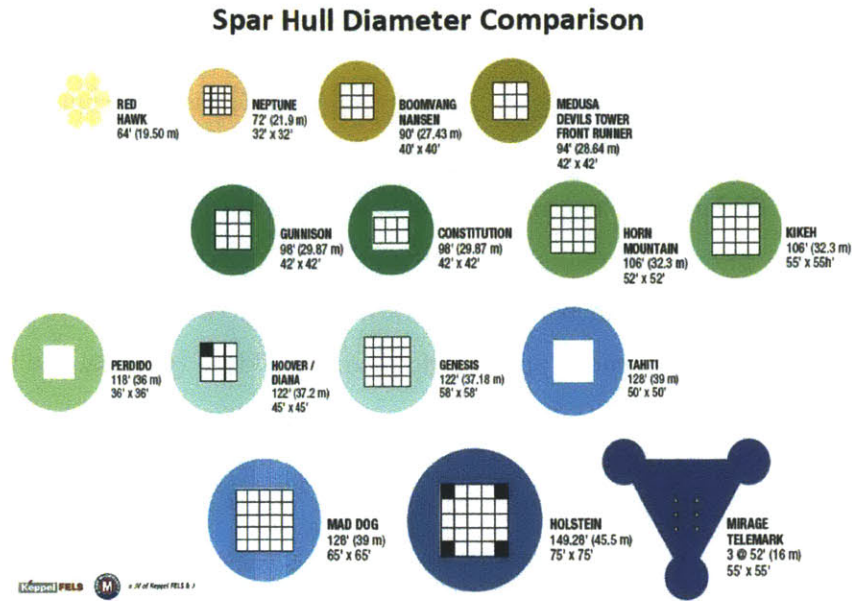


Figure 2-4: Statistics of the diameters of the existing spars (Barton, n.d.)

$$H_c = \frac{2}{3} H_s = \frac{2}{3} \times 12 = 8 \text{ m} \quad (2.2)$$

However, there can be too much air gap. Excessive air gap raises the centre of gravity and thereby impairs the payload performance. Determination of the effective free-board should take the relative motions of the hull into account. For large, long period waves, such a floating platform will tend to rise and fall synchronously with the waves, possibly as much as 20% of the wave height. To recognize this, in initial design, it can be conservatively assumed that the platform rises 10% of the wave height. Then setting the calm water deck height at 5 ft plus 90% of H_c should suffice (Chakrabarti 2005; Vol.1, Ch.7, Sec.7.5). Thus the free-board H_f should be at least:

$$H_f = H_a + 90\% H_c = 1.5 + 0.9 \times 8 = 8.7 \text{ m} \quad (2.3)$$

Thus, we can finally set the H_f to be 9 m.

name	description	draft H/m
minifloat IV	semi	30
Morpeth	mini-TLP	27.7
Allegheny	mini-TLP	27.7
Typhoon	mini-TLP	27.7
Matterhorn	mini-TLP	32
–	mini-TLP	28.51
WADO	mini-TLP	28.5
Prince	mini-TLP	34.75
Marco Polo	mini-TLP	39.6

Table 2.2: Statistics of the draft H of the present mini-platforms (from Wilhoit 2010; Kibbee et al. 1999; Kibbee & Snell 2002; Koon et al. 2002; Cermelli et al. 2004)

2.3.3 Dimensions of the decks of the mini-platform

Due to the limit of small water plane area, the deck usually has two or three levels for mono-column floaters (Chakrabarti 2005; Vol.1, Ch.7, Sec.7.6) . Here we can refer to the topsides of SeaStar miniTLP which is also a mono-column small production platform. The deck has two levels. The dimensions of the deck is $27.4 \text{ m} \times 27.4 \text{ m}$ (Kibbee et al. 1994). Since we hope to lower the gravity as much as possible, we initially choose 6 m to be the distance between the two levels.

2.3.4 Draft of the mini-platform (H)

Our platform is similar to spars in achieving hydrostatic stability by placing the gravity centre below the buoyancy centre. The product of inertia of the water plane usually contributes little. Therefore deeper draft is beneficial for lowering the centre of gravity. In addition, deeper draft tends to decrease the area of waterplane, thereby reducing hydrodynamic motions. However, large draft would result in heavier steel for the lower part of the hull. Hulls with shorter drafts and larger diameters have less surface area and less steel. Referring to Table 2.3.4 (from Wilhoit 2010; Kibbee et al. 1999; Kibbee & Snell 2002; Koon et al. 2002; Cermelli et al. 2004), we can see that most of the drafts of the present miniature platforms are around 30 m. Hence we can initially select the draft H around 30 m.

2.3.5 Dimensions of the heave plate of the mini-platform

As mentioned in section 2.1, heave plates are one of the most common motion-suppression devices in offshore floating platforms. They can increase heave added mass and viscous damping effectively without increasing too much displacement. Larger R_3 tends to generate larger added mass, beneficial for the hydrodynamic motion. For smaller R_3 , interference of the hull boundary on the vortex formation and shedding process at the edge of the heave plate suppresses the vortices, resulting in lower damping (Tao & Cai 2004). However, since the draft of our platform is not too deep, larger plate would induce larger wave exciting force. Also, large heave plate would bring inconvenience in transportation and installation of the platform. Therefore, we need to make a trade-off when selecting the dimension of the heave plate.

As for thickness, thinner plates generally have more significant damping effects. This is because small thickness enhances the interaction of the vortices formed during any two successive half cycles (Tao & Thiagarajan 2003; Tao & Cai 2004). Therefore, we should try to minimize the thickness. Let us set it within $0.2 \sim 0.7$ m at this initial phase.

2.3.6 Summary in the main dimensions of the mini-platform

In summary, the main dimensions of our platform would be:

- (1) Waterplane: $R_1 \geq 7.0m$
- (2) Freeboard: $H_f \sim 9m$
- (3) Deck: $27.4m \times 27.4m \times 6m$
- (4) Draft: $H \sim 30m$

Items	Weight/t	x_2/m
Topside Payload	3,000	11.0
Hull	2,800	-20.0
Heave Plate	1,000	-30.0
Ballast+Mooring	6,200	-30.0
Total	13,000	-18.4

Table 2.3: An example of the estimation of the VCG of the platform based on the weight distribution of different components at the initial stage, where the coordinate

2.4 Estimation of the inertial parameters of the mini-platform

2.4.1 Vertical centre of gravity of the mini-platform (VCG)

After sizing the platform and obtaining the weight distribution, we can estimate the vertical centre of gravity (VCG) and check whether it satisfies the hydrostatic stability requirement. The estimation of VCG requires us to list the weight and the centre of gravity for different items (Li & Ou, 2010) (see Table 2.3). For the arrangement of the topsides, we try to place the heavy facilities on the lowest deck level (cellar deck) as much as possible. Here we can consider its VCG is about 2 m above the cellar deck. For the ballast and mooring, we assume the VCG to be at the keel of the platform.

Table 2.3 is an example to illustrate how to obtain the vertical coordinate of the gravity centre of the platform at this initial phase based on the standard weighting method. The dimensions and weights shown in the Table 2.3 can be further adjusted within the frame of the general scale in the following design stages. The centre of buoyancy (VCB) is the geometric centre of the submersible volume. Ignoring the contribution from the water-plane area, it is easy to obtain the rough value of the metacentric height GM based on VCG and VCB. According to ABS rules (ABS 2012), the metacentric height for MODUs should satisfy:

$$0 < GM < 2.24 \text{ m} \tag{2.4}$$

Larger GM provides better hydrostatic stability. However, we should also keep in mind that GM also measures the stiffness of the pitch motion. Smaller GM tends to result in smaller natural frequency in pitch motion. Therefore, we again need to make a trade-off between the hydrostatic stability and the hydrodynamic motions when determining GM. Here we choose GM as small as possible while not smaller than 1 m.

2.4.2 Radius of gyration of the mini-platform (R_g)

In addition to the gravity centre, the radius of gyration is another important parameter of inertia. Given that the vertical distribution of important items have already be determined (see Table 2.3), it is straightforward to capture the radius of gyration around x_1/x_3 (Li & Ou 2010).

As the conceptual design, we suppose the mass is uniformly distributed around x_2 when estimating the R_g around x_2 .

Chapter 3

Hydrodynamic Models and Numerical Methods

In the previous chapter, we have estimated the main dimensions and weight distribution of our mini-platform. The next phase of design is to obtain a geometry that has a satisfactory motion response in waves within the frame of the previous sizing. In this chapter, the models and methods for describing the motion response of a floating body in ocean waves would be presented. We start with the simplest case where the incident waves are plane progressive waves of small amplitude. The result of this case is the response of a floating body in regular waves. Later the prediction of the response in irregular based on the solution to the problem of regular waves will be given.

3.1 Equation of motion of a floating body in regular waves

Let us first derive the equation of motion of a free floating body in regular waves by equating all the hydrodynamic forces to the inertial forces. Here at the very initial stage of the design, we ignore the forces due to risers and moorings. Assume the platform is rigid, unrestrained, and already in a state of stable equilibrium when in

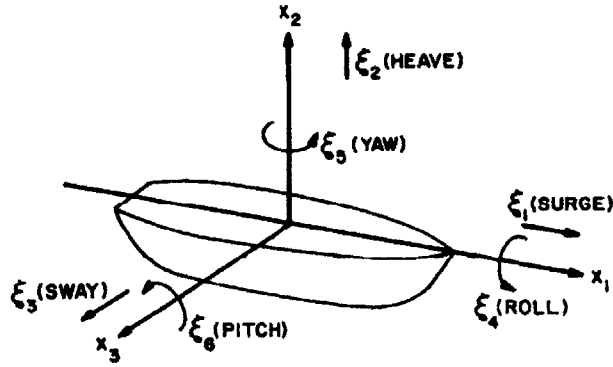


Figure 3-1: Definition of the coordinate systems and sketch of body motions in six degrees of freedom, where $\xi_1 \sim \xi_6$ represent the displacement in the corresponding modes (from Newman 1977)

clam water. The response of the platform to the action of waves including six degrees of freedom and the coordinate system are illustrated in Figure 3-1 (from Newman 1977). It is well known that the equations of motion for free oscillations of a rigid body in plane progressive waves of frequency ω are in the following form (Newman 1977):

$$(M_{ij} + A_{ij})\ddot{\xi}_j + B_{ij}^P \dot{\xi}_j + B_{ij}^V |\dot{\xi}_j| \dot{\xi}_j + C_{ij} \xi_j = AX_i \quad (i, j = 1, 2, \dots, 6) \quad (3.1)$$

Where: M_{ij} is the mass matrix;

A_{ij} is the added mass coefficients;

B_{ij}^P is the linear wave damping coefficients;

B_{ij}^V is the viscous damping coefficients;

C_{ij} is the restoring force coefficients;

A is the amplitude of the linear incident wave;

X_i is the wave exciting force on the body in the i -th direction per incident wave amplitude;

ξ_j is the amplitude of the body response in the j -th direction.

The forces in this equation of motion (3.1) imply that we can decompose this

problem into two sub-problems. One is the well-known wave radiation/diffraction problem which associates with all the linear hydrodynamic coefficients. For this problem, the most common way is to apply the potential flow model. The other is the viscous damping problem involving the nonlinear damping term $B_{ij}^V|\dot{\xi}_j|\dot{\xi}_j$. As mentioned in Chapter 1, a new model is developed in this thesis to quickly estimate the viscous damping coefficient B_{ij}^V .

3.2 Potential flow model for the linear wave-body problem

For this sub-problem, we assume the flow to be inviscid, incompressible and irrotational. Therefore, potential-flow theory is valid. Due to the linearity of this problem, the total velocity ϕ can be decomposed into the following form (Newman 1977; Mei et al. 2005):

$$\phi(x, y, z, t) = Re\left(\sum_{j=1}^6 \xi_j \phi_j(x, y, z) + A\phi_A(x, y, z)\right)e^{i\omega t} \quad (3.2)$$

In the above, ϕ_j represents the radiation potential associated with the harmonic motion of a rigid body in the j -th direction, which is forced with unit amplitude in the calm water. For example, if the body is forced to oscillate in heave with unit amplitude, the resulting velocity potential is denoted as ϕ_2 . The potentials $\phi_j, j = 1, 2, \dots, 6$ are the solutions of the so-called “radiation” problem.

The potential ϕ_A for the flow due to the interaction of a fixed body with incident waves. This is regarded as the wave “diffraction” problem.

Let us define the following symbols:

- L is the length scale of the floating body;
- ∇ is the displaced volume;
- S_B is the wetted body surface;

- S_F is the free surface;
- \mathbf{n} is the unit normal vector, directed out of the fluid;
- \mathbf{r} is the position vector (x_1, x_2, x_3) ;
- A_{ij}^* is the dimensionless added mass coefficient;
- B_{ij}^{P*} is the dimensionless linear wave damping coefficient;
- C_{ij}^* is the dimensionless restoring coefficient;
- X_i^* is the dimensionless wave exciting force;

3.2.1 Hydrostatic force of a freely floating body

For a freely floating body, the hydrostatic force can be written as (Lee 1995):

$$F_{s_i} = - \sum_{j=i}^6 C_{ij} \xi_j, \quad i = 1, 2, \dots, 6 \quad (3.3)$$

here C_{ij} is 6×6 restoring coefficient matrix with nonzero elements:

$$C_{22} = \rho g S \quad (3.4)$$

$$C_{44} = \rho g \nabla [(S_{33}/\nabla) + x_2^B - x_2^G] \quad (3.5)$$

$$C_{66} = \rho g \nabla [(S_{11}/\nabla) + x_2^B - x_2^G] \quad (3.6)$$

Here x_2^B is the VCB, x_2^G is the VCG (defined in Chapter 2, section 2.4), S is the waterplane area, and the waterplane moments are defined as:

$$S_{ij} = \iint_S x_i x_j dS \quad (3.7)$$

The corresponding nondimensional form of the restoring coefficients are:

$$C_{22}^* = C_{22}/\rho g L^2 \quad (3.8)$$

$$C_{44}^* = C_{44}/\rho g L^4 \quad (3.9)$$

$$C_{66}^* = C_{66}/\rho g L^4 \quad (3.10)$$

As can be seen, there is no hydrostatic restoring force or moments in surge, sway and yaw, so these are neutrally stable modes. On the contrary, heave, pitch and roll are self-restored modes. These three modes are statically stable if the corresponding C_{ij} are positive.

3.2.2 Radiation problem of an oscillatory body in calm water

For the radiation problem, the governing equations are (Newman 1977; Lee 1995; Mei et al. 2005):

$$\nabla^2 \phi_j = 0, \quad \text{in fluids,} \quad j = 1, 2, \dots, 6. \quad (3.11)$$

$$-\frac{\omega^2}{g} \phi_j + \frac{\partial \phi_j}{\partial y} = 0, \quad \text{on } y = 0, \quad j = 1, 2, \dots, 6. \quad (3.12)$$

$$\frac{\partial \phi_j}{\partial \mathbf{n}} = i\omega \mathbf{n}_j, \quad \text{on } S_B, \quad j = 1, 2, 3. \quad (3.13)$$

$$\frac{\partial \phi_j}{\partial \mathbf{n}} = i\omega(\mathbf{r} \times \mathbf{n})_j, \quad \text{on } S_B, \quad j = 4, 5, 6. \quad (3.14)$$

$$\phi_j \rightarrow 0, \quad \text{as } y \rightarrow -\infty, \quad j = 1, 2, \dots, 6. \quad (3.15)$$

$$\phi_j \propto R^{-1/2} e^{-ikR}, \quad \text{as } R \rightarrow \infty, \quad j = 1, 2, \dots, 6. \quad (3.16)$$

Here $R = (x_1^2 + x_3^2)^{1/2}$, and k is the wavenumber corresponding to the frequency ω .

The pressure due to the radiation potential can be derived from the Bernoulli's equation provided that ϕ_j 's are solved. Integrating the pressure over S_B and retaining only the first order linear terms, we can obtain the added mass coefficient and the

linear wave damping coefficients:

$$A_{ij}^* - iB_{ij}^{P*} = \frac{1}{L^k} \iint_{S_B} n_i \phi_j dS \quad (3.17)$$

$$A_{ij}^* = \frac{A_{ij}}{\rho L^k} \quad (3.18)$$

$$B_{ij}^{P*} = \frac{B_{ij}^P}{\rho L^k \omega} \quad (3.19)$$

where $k = 3$ for $i, j = 1, 2, 3$, $k = 4$ for $i = 1, 2, 3, j = 4, 5, 6$ or $i = 4, 5, 6, j = 1, 2, 3$ and $k = 5$ for $i, j = 4, 5, 6$.

3.2.3 Diffraction problem of a fixed body in regular waves

The governing equations for the diffraction problem is (Newman 1977; Lee 1995; Mei et al. 2005):

$$\phi_A = \phi_0 + \phi_7, \quad (3.20)$$

$$\nabla^2 \phi_j = 0, \quad \text{in fluids,} \quad (3.21)$$

$$-\frac{\omega^2}{g} \phi_j + \frac{\partial \phi_j}{\partial y} = 0, \quad \text{on } y = 0, \quad (3.22)$$

$$\frac{\partial \phi_7}{\partial n} = -\frac{\partial \phi_0}{\partial n}, \quad \text{on } S_B, \quad (3.23)$$

$$\phi_j \rightarrow 0, \quad \text{as } y \rightarrow -\infty \quad (3.24)$$

$$\phi_j \propto R^{-1/2} e^{-ikR}, \quad \text{as } R \rightarrow \infty. \quad (3.25)$$

where ϕ_0 is the incident wave potential, which is known. ϕ_7 is the scattering potential to represent the disturbance of the incident waves by the fixed body. $R = (x_1^2 + x_3^2)^{1/2}$.

Similarly, the pressure is given by the Bernoulli's equation. Integrate the pressure over the wetted surface, we can obtain the wave exciting force and moment on the body:

$$X_i^* = -\frac{1}{gL^m} \iint_{S_B} (\phi_0 + \phi_7) \frac{\partial \phi_i}{\partial n} dS \quad (3.26)$$

where $m = 2$ for $i = 1, 2, 3$ and $m = 3$ for $i = 4, 5, 6$.

Therefore, as long as we can solve the boundary value problems governing $\phi_i, i = 1, 2, \dots, 7$, we can obtain all the linear hydrodynamic coefficients in equation 3.1. In our design, we use the standard Radiation/Diffraction code WAMIT to solve for all these coefficients.

3.2.4 Panel method for the radiation/diffraction problem

In WAMIT, the boundary value problems for $\phi_j, j = 1, 2, \dots, 7$ defined above are solved by the boundary integral equation methods (Lee 1995).

To derive the integral equation, we introduce a Green Function G which satisfies the following conditions (John 1950; Lee 1995):

$$\nabla^2 G = 0, \quad \text{in fluids for } (x_1, x_2, x_3) \neq (x_1^0, x_2^0, x_3^0) \quad (3.27)$$

$$-\frac{\omega^2}{g} G + \frac{\partial G}{\partial y} = 0, \quad \text{on } y = 0 \quad (3.28)$$

$$G \rightarrow 0, \quad \text{as } y \rightarrow -\infty \quad (3.29)$$

$$G - \frac{1}{R} \quad \text{is bounded for } (x_1, x_2, x_3) \rightarrow (x_1^0, x_2^0, x_3^0) \quad (3.30)$$

where $R = \sqrt{(x_1 - x_1^0)^2 + (x_2 - x_2^0)^2 + (x_3 - x_3^0)^2}$

One solution of G is:

$$G(\mathbf{x}; \mathbf{x}^0) = \frac{1}{R} + \frac{1}{R'} + \frac{2k}{\pi} \int_0^\infty d\kappa \frac{e^{\kappa(x_2 + x_2^0)}}{\kappa - k} J_0(\kappa r) \quad (3.31)$$

$$R' = \sqrt{(x_1 - x_1^0)^2 + (x_2 + x_2^0)^2 + (x_3 - x_3^0)^2} \quad (3.32)$$

$$r = \sqrt{(x_1 - x_1^0)^2 + (x_3 - x_3^0)^2} \quad (3.33)$$

where J_0 is the Bessel function of zero-th order. $\mathbf{x} \equiv (x_1, x_2, x_3)$, while $\mathbf{x}^0 \equiv (x_1^0, x_2^0, x_3^0)$.

According to the Green's Theorem:

$$\iiint_{\Omega} (\phi_j \nabla^2 G - G \nabla^2 \phi_j) = \iint_{\partial\Omega} (\phi_j \frac{\partial G}{\partial n} - G \frac{\partial \phi_j}{\partial n}) dS \quad j = 1, 2, \dots, 7 \quad (3.34)$$

Now consider a control volume of fluid Ω , bounded by the free surface S_F , body surface S_B , a surface at infinity S_∞ , and an infinitely small spherical surface S_ϵ surrounding the singular point (x_1^0, x_2^0, x_3^0) (see Figure 3-2). Then equation (3.34) can be further expanded in the following way:

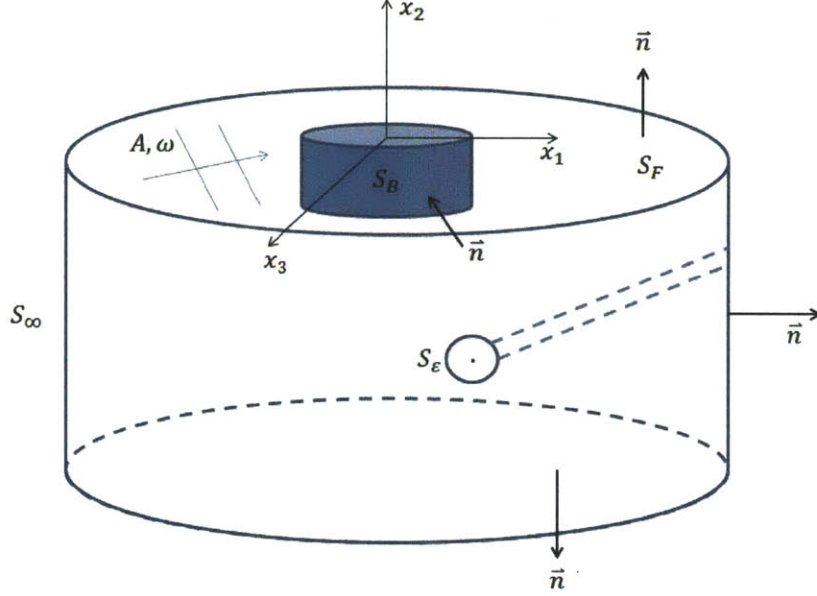


Figure 3-2: Sketch of the domain for the boundary value problem and the definition of the coordinate system, where S_F is the free surface, S_B is the wetted body surface, S_∞ is the surrounding surface at infinity and S_ϵ is an infinitely small surface surrounding a singular point. \vec{n} is the normal vector pointing out of the fluid.

$$\iiint_{\Omega} (\phi \nabla^2 G - G \nabla^2 \phi) d\Omega = \iint_{S_F + S_B + S_\infty + S_\epsilon} \left(\phi \frac{\partial G}{\partial n} - G \frac{\partial \phi}{\partial n} \right) dS \quad (3.35)$$

Where ϕ represents $\phi_j, j = 1, 2, \dots, 7$.

Since G satisfies the same boundary condition as ϕ at free surface and infinity,

$$\iint_{S_F} = \iint_{S_\infty} = 0 \quad (3.36)$$

We thus have:

$$\iiint_{\Omega} (\phi \nabla^2 G - G \nabla^2 \phi) d\Omega = \iint_{S_B + S_\epsilon} \left(\phi \frac{\partial g}{\partial n} - G \frac{\partial \phi}{\partial n} \right) dS = 0 \quad (3.37)$$

If (x_1^0, x_2^0, x_3^0) is on S_B , then S_ϵ becomes a hemisphere with radius of ϵ , and we obtain:

$$2\pi\phi(x_1^0, x_2^0, x_3^0) = - \iint_{S_B} \left(\phi \frac{\partial G}{\partial n} - G \frac{\partial \phi}{\partial n} \right) dS \quad (3.38)$$

To be more specific, if we plug in the kinematic boundary conditions for radiation and diffraction velocity potentials, we can arrive at:

$$2\pi\phi_j(\mathbf{x}_0) + \iint_{S_B} \phi_j(\mathbf{x}) \frac{\partial G(\mathbf{x}; \mathbf{x}^0)}{\partial n_x} d\mathbf{x} = \iint_{S_B} n_j G(\mathbf{x}; \mathbf{x}^0) d\mathbf{x} \quad j = 1, 2, \dots, 6 \quad (3.39)$$

$$2\pi\phi_A(\mathbf{x}^0) + \iint_{S_B} \phi_A(\mathbf{x}) \frac{\partial G(\mathbf{x}; \mathbf{x}^0)}{\partial n_x} d\mathbf{x} = 4\pi\phi_0(\mathbf{x}) \quad (3.40)$$

where n_x is the normal vector evaluated at point \mathbf{x} .

After obtaining the integral equations (3.39) and (3.40), we solve these two equations by using the so-called ‘‘Panel Method’’. Since the integrals are evaluated on S_B , we approximate the body surface by a collection of quadrilaterals, i.e., ‘‘panels’’. Each panel is defined by four vertices, lying on the body surface. Then ϕ is approximated by a constant over each panel. Based on this discretization, the continuous integral equations (3.39) and (3.40) are reduced to a set of linear equations for the unknown values of the potentials over the panels (Lee 1995; Lee & Newman 2005). For the radiation velocity potential:

$$2\pi\phi(\mathbf{x}_i) + \sum_{k=1}^N D_{ik}\phi_k = \sum_{k=1}^N S_{ik} \left(\frac{\partial \phi}{\partial n} \right)_k, \quad (3.41)$$

where $i = 1, 2, \dots, N$ with N being the total number of panels. For the diffraction potentials,

$$2\pi\phi(\mathbf{x}_i) + \sum_{k=1}^N D_{ik}\phi_k = 4\pi\phi_0(\mathbf{x}_i) \quad (3.42)$$

The influence coefficient matrices D_{ik} and S_{ik} are defined as:

$$D_{ik} = \iint_{s_k} \frac{\partial G(\mathbf{x}; \mathbf{x}_i)}{\partial n_x} d\mathbf{x} \quad (3.43)$$

$$S_{ik} = \iint_{s_k} G(\mathbf{x}; \mathbf{x}_i) d\mathbf{x} \quad (3.44)$$

where s_k denotes the surface of the k th panel. The collocation points \mathbf{x}_i , where the integral equations are enforced, are located at the panel centroids. The evaluation of these matrices on panels are discussed in Newman (1986).

Therefore, solving the linear systems of equations (3.41) and (3.42), we obtain the potentials anywhere on the wetted surface body, thereby obtaining the added mass, wave damping coefficients and wave exciting forces in equation (3.1).

3.3 Vortex damping model for the viscous drag on the heave plate

Our design combines features of a spar and a heave plate at the keel, to provide a small floating platform with excellent motion characteristics (see Chapter 2, section 2.1). The heave plate can increase the viscous damping significantly through vortex shedding. However, this effect cannot be captured by the potential flow model. In addition, as discussed in Chapter 1, there is no satisfactory model nowadays that can predict B_{ij}^V efficiently and accurately. In this section, we would present a newly developed model “Discrete Vortex Model (DVM)” or “Discrete Vortex Ring Model (DVRM)”, which is capable of providing a reliable estimation of the viscous damping coefficient efficiently.

3.3.1 Viscous drag of a 2D oscillatory thin plate

Problem formulation

Let us start with a simplified problem. Consider a two dimensional infinitely thin plate with a length of D oscillating in an unbounded and inviscid fluid. The velocity of the plate is prescribed as:

$$V(t) = V_0 \sin\left(\frac{2\pi}{T}t\right) \quad (3.45)$$

The flow separates at the two edges of the plate, shedding vortices into the flow. The Reynolds number (Re) in this problem is infinite. The two dimensionless parameters governing this 2D problem are Keulegan-Carpenter number (KC) and total force coefficient (C).

$$KC = \frac{V_0 T}{D} \quad (3.46)$$

$$C = \frac{F}{\frac{1}{2}\rho|V_0|^2 D} \quad (3.47)$$

where F is the total hydrodynamic force on the plate and ρ is the fluid density.

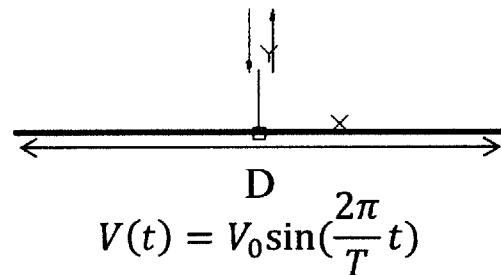


Figure 3-3: A two dimensional infinitely thin plate with a length D oscillates in an unbounded and inviscid fluid.

For typical offshore platforms, KC number is normally less than 10 (Faltinsen 1993). The maximum displacement of fluid particles in the undisturbed flow is small compared with the characteristic length of the body. This physically means that the viscous force is small compared to the inertia force in general. This justifies the assumption that the fluid is inviscid.

In this problem, separation occurs at the edges of the plate, and will give rise to two free shear layers in the flow. At the edges, the flow cannot negotiate with the high curve and thus separates, thereby forming free shear layers of thickness comparable to that of the thin boundary layer. Therefore, the effects of viscosity are important in the formation of the free layers, but only confined to a small region close to the boundaries of the plate (De Bernardinis et al., 1981). Since we assume the Reynolds number to be infinite, we expect that the separated shear layers do not diffuse and thicken, but remain thin for all the time. This serves as the basis of representing the two free shear layers by two free vortex sheets. This is the common method to deal with the vortex shedding problems now, as mentioned in Chapter 1. Next we will review the existing known vortex sheet model (VSM), and then present the development of the new model Discrete Vortex Method (DVM).

Vortex sheet model (VSM)

In this subsection, we follow the general outline of Jones (2003) and Krasny (1991) to illustrate this commonly used model VSM.

Assume a bound vortex sheet lies on the plate, and is shed at the two separation points as two free vortex sheets (Krasny 1991; Hou et al. 2006; Jones 2003). The problem of finding the associated drag force on the plate can be divided into three parts: (1) the potential flow solution, (2) the inviscid flow separation and (3) the evolution of the free vortex sheet.

Define the following symbols:

- $l_{=}$ is the oscillating plate;
- l_{\pm} are the free layers shed into the fluid;
- $x_{e\pm}$ are the two edges of the plate from which the vortex sheets are shed;
- \vec{n} is the normal vector pointing into the fluid;
- γ is the strength of the vortices distributed on the plate and the free layers.

(1) Potential Flow Solution

The governing equation for an ideal, inviscid and irrotational flow is the Laplace equation:

$$\nabla^2 \phi = 0 \quad (3.48)$$

where ϕ is the velocity potential. The potential should satisfy the kinematic boundary condition on the plate all the time:

$$\frac{\partial \phi}{\partial n} = \vec{V} \cdot \vec{n} \quad \text{on } l_- \quad (3.49)$$

where \vec{V} is the velocity of the plate.

A boundary integral method can be used to solve the boundary value problem for ϕ . Basically we distribute bound vortices on l_- and free vortices on l_+ . The position of $l_-(t)$ is known since it coincides with the plate at any time t . However, the position of the free vortex sheets $l_\pm(t)$ are only known initially, and need to be determined at later times. The strength of the vortices on these sheets is determined by imposing the kinematic boundary conditions on the plate.

$$\left(\int_{l_+} \gamma(\vec{\xi}, t) \frac{\vec{k} \times \vec{r}}{2\pi|\vec{r}|^2} ds + \int_{l_-} \gamma(\vec{\xi}, t) \frac{\vec{k} \times \vec{r}}{2\pi|\vec{r}|^2} ds \right) \cdot \vec{n}_x = V_0 \sin(\omega t) \quad (\vec{x} \in l_-) \quad (3.50)$$

where $\vec{r} = \vec{x} - \vec{\xi}$, \vec{x} is the point in which the kinematic boundary condition is imposed, and $\vec{\xi}$ is the point where the vorticity strength γ is evaluated.

Now let us define a function $\Psi(\vec{x}, t)$ in the following form.

$$\Psi(\vec{x}, t) = \begin{cases} \int_B d\gamma, & \text{for } \vec{x} \in l_+(t) \\ \int_{l_+} d\gamma + \int_{x_{e+}}^x d\gamma, & \text{for } \vec{x} \in l_-(t) \\ \int_{l_+} d\gamma + \int_{l_-} d\gamma + \int_{x_{e-}}^x d\gamma, & \text{for } \vec{x} \in l_-(t) \end{cases}$$

Ψ is the circulation around the contour which includes one free end B , and intersects the boundaries once at point \vec{x} . Such a contour is shown in Figure 3-4. Based on Kelvin's Theorem, for a flow starting from the rest, the total circulation around

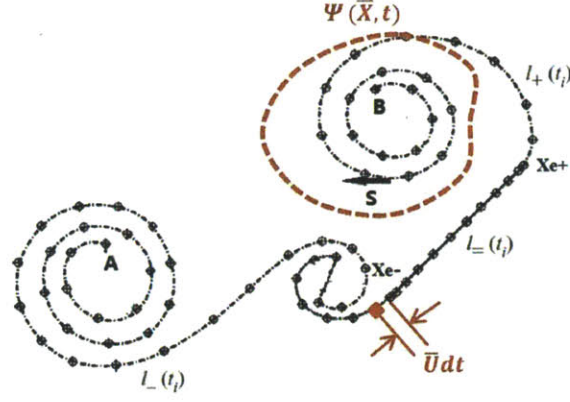


Figure 3-4: A sketch of the distribution of the singularities on the plate and the free layers. The definition of Ψ is illustrated (adapted from Jones 2003)

a closed contour which does not intersect $l(t)$ should be conserved to be zero all the time. Therefore, the following condition should be guaranteed:

$$\int_{l_-} d\gamma + \int_{l_=} d\gamma + \int_{l_+} d\gamma = 0 \quad (3.51)$$

Note that a vortex sheet is such a line in the fluid that across it the normal velocity is continuous, whereas the tangential velocity and potential is discontinuous. Therefore, the expression of the tangential velocity at the upper and lower sides of the boundary would be:

$$V_t^\pm(\vec{x}, t) = \left(\int_{l_\pm + l_=} \gamma(\vec{\xi}, t) \frac{\vec{k} \times \vec{r}}{2\pi|\vec{r}|^2} ds \right) \cdot \vec{t}_x \mp \frac{1}{2} \frac{\partial \Psi(\vec{x}, t)}{\partial s} \quad (3.52)$$

where \vec{s} is the tangential vector along the sheet (see Figure 3-4). Therefore, the jump of the tangential velocity across the sheets can be expressed as:

$$\Delta V_t(\vec{x}, t) = \frac{\partial \Delta \phi(\vec{x}, t)}{\partial s} = \frac{\partial \Psi(\vec{x}, t)}{\partial s} \quad (3.53)$$

By integration along the sheet, we can also obtain the potential jump across the sheet.

$$\Delta \phi(\vec{x}, t) = \Delta \phi(B, t) + \int_l \frac{\partial \Psi(\vec{x}, t)}{\partial s} ds = \Psi(\vec{x}, t) \quad (3.54)$$

Knowing the potential jump and the tangential velocity jump across the plate, we can derive the pressure jump by applying the Bernoulli's equation.

$$\Delta p(\vec{x}, t) = -\rho \left\{ \frac{\partial \Psi(\vec{x}, t)}{\partial t} + \frac{1}{2} (V_t^{+2} - V_t^{-2}) \right\} \quad (3.55)$$

Therefore, the total drag coefficient on the plate is:

$$C(t) = \frac{\int_{l_-} \Delta p(\vec{x}, t) ds}{\frac{1}{2} \rho |V_0|^2 D} \quad (3.56)$$

Thus the key is to solve the integral equation (3.50) for unknown vortex strength. Equation (3.50) is a Fredholm equation of the first kind. We can obtain an numerical solution of this equation by discretizing the plate l_- into N segments δl_j , and then approximate the continuous distribution of vorticity γ by $N+1$ bound point vortices situated at the ends of these N segments with strength:

$$\Gamma_j^b = \bar{\gamma}_j \delta l_j, \quad j = 1, 2, \dots, N+1 \quad (3.57)$$

Also, the two free vortex sheets can be approximated by a set of free point vortices in the fluids with strengths Γ_m^f to be determined by Kutta condition. This will be presented later. Therefore, equation (3.50) becomes a $N \times N$ linear equations evaluated at the midpoint \vec{x}_i of each segment.

$$\sum_{j=1}^{N+1} \Gamma_j^b \left(\frac{\vec{k}_j \times \vec{r}_{i,j}}{2\pi |\vec{r}_{i,j}|^2} \cdot \vec{n}_i \right) = V_{ni} - \sum_m \Gamma_m^f \left(\frac{\vec{k}_m \times \vec{r}_{i,m}}{2\pi |\vec{r}_{i,m}|^2} \cdot \vec{n}_i \right) \quad i = 1, 2, \dots, N \quad (3.58)$$

Similarly, equation (3.51) can be written as:

$$\sum_j \Gamma_j^b + \sum_m \Gamma_m^f = 0, \quad j = 1, 2, \dots, N+1 \quad (3.59)$$

Note that in our case, the problem is symmetric. Thus we need to consider half of the plate only.

Equation (3.58) and equation (3.59) together can also be written in a matrix form:

$$\mathbf{A}\boldsymbol{\Gamma} = \mathbf{B} \quad (3.60)$$

Therefore, the solution would be:

$$\boldsymbol{\Gamma} = \mathbf{A}^{-1}\mathbf{B} \quad (3.61)$$

Here the matrix \mathbf{A} only depends on the geometry of the boundaries.

After obtaining the strengths of all the singularities, we can solve for the tangential velocity and the pressure jumps across the plate from equation (3.52) and equation (3.55).

The accuracy of this method depends on the the use of the number of the elements and the distribution of the quantities over each element (Hess & Smith 1966). We should pay attention on the geometrical singularities in the boundaries, i.e., the ends of the plate. As the distance along the boundary from the singularity decreases, the size of the element should decrease to ensure the accuracy of the solution.

(2) Inviscid Flow Separation

In this problem, the viscosity effect is important in producing vortices, but only confined to a small region. This effect is handled by imposing the so-called Kutta condition in potential theory to determine the vortex shedding rate and the position of the nascent vortices.

It is known in the potential flow theory that if the flow passed an edge of zero angle without separation, there is a square-root singularity in velocity at that edge (Newman 1977). This is not allowed in the real physical problem. Thus the Kutta condition is derived from the central physical principle that the velocity field should be bounded everywhere (Bearman 1984). There are many versions of Kutta conditions, including steady Kutta condition and unsteady ones. Here we impose one of the unsteady Kutta conditions following the work of Krasny (1991). It is different from the one used in Jones (2003).

This Kutta condition contains two requirements:

- Pressure jump at the edge must vanish;
- The vortex is shed from the edge tangentially.

Due to the symmetry of this problem, here we consider one edge of the plate x_{e+} as illustration. The vortex shedding rate can be determined by the following equation:

$$\frac{d\Gamma}{dt} = \frac{d\Psi(x_{e+}, t)}{dt} = \frac{1}{2}(V_t^{-2} - V_t^{+2}) \quad (3.62)$$

where V_t^- and V_t^+ are the one-sided velocities at the edge. The slip velocities satisfy:

$$V_t^- + V_t^+ = \bar{V}_t, \quad \frac{1}{2}(V_t^- - V_t^+) = \gamma(x_{e+}) \quad (3.63)$$

where \bar{V}_t is the averaged velocity, and $\gamma(x_{e+})$ is the vortex sheet strength at the edge. The average velocity \bar{V}_t is the induced velocity due to all the singularities in the fluids. $\gamma(x_{e+}) \sim \partial\Psi(x_{e+})/\partial s$ is calculated by a finite difference formula applied to Ψ . Specific procedures are:

(i) Solve the linear system equation (3.58) to obtain the bound vortices strength near the edge, thereby obtaining $\gamma(x_{e+})$ via finite difference method;

(ii) Calculate the averaged slip velocity at the edge \bar{V}_t using the discretized form of equation (3.52):

$$\bar{V}_t(\vec{x}_{e+}, t) = \sum_m \Gamma_m^f \left(\frac{\vec{k} \times \vec{r}_{m, x_{e+}}}{2\pi |\vec{r}_{m, x_{e+}}|^2} \cdot \vec{t}_{x_{e+}} \right). \quad (3.64)$$

where \vec{k} is the unit vector of the vorticity of the m-th point vortex. \vec{r} is the vector from the m-th point vortex to x_{e+} , and $\vec{t}_{x_{e+}}$ is the tangential unit vector at x_{e+} .

(iii) Use equation (3.63) to obtain V_t^- and V_t^+ . Note that the shedding rate (3.62) is insensitive to the sign of the slip velocity. However, a negative value of V_t^- or V_t^+ represents an attached slip flow on that side of the plate, while a positive value denotes a separating flow. Therefore, if either $V_t^- < 0$ or $V_t^+ < 0$, we set the value of the sided slip velocity to be 0 to prevent an attached slip flow.

(iv) Obtain the vortex shedding rate using the new values of V_t^- and V_t^+ from

equation (3.62).

The continuous shedding process is simulated by releasing free point vortices from the edge at regular time intervals δt . The strength of the m -th vortex shed satisfies $\Gamma_m^f = d\Gamma/dt \cdot \delta t$. When a nascent free vortex is produced at the edge, let it convect with velocity $(u, v) = (V_n(x_{e+}, t), \bar{V}_t(x_{e+}, t))$. This determines the position of the newly shed vortex, and also guarantees the tangential shedding condition required previously.

(3) Free Vortex Sheet Evolution

After shed into the fluids, the free vortices convect with the local flow velocity. However, there is a singularity when calculating the induced velocity due to all the vortices. In order to avoid the singularity associated with this induced velocity of a thin vortex sheet, the desingularization method of Krasny (1987) is applied. The induced velocity of the m -th free vortices is given by:

$$\left(\frac{dx_m}{dt}, \frac{dy_m}{dt}\right) = \left(\sum_i \frac{-(y_m - y_i), (x_m - x_i))\Gamma_i^b}{2\pi[(x_m - x_i)^2 + (y_m - y_i)^2]}, \sum_{k \neq m} \frac{-(y_m - y_k), (x_m - x_k))\Gamma_k^b}{2\pi[(x_m - x_k)^2 + (y_m - y_k)^2 + \delta^2]}\right) \quad (3.65)$$

where δ is the desingularization factor and $0 \leq \delta \leq 1$. It can be proved that when δ approaches to zero, this induced velocity approaches to the true value (Krasny 1987).

In summary, equations (3.65) and (3.62) form a coupled system of ordinary differential equations for the motion of the free vortex sheets and the variation of the total shed circulation $\Psi(x_{e+}, t)$. We solve this system numerically. At each time step the solution procedure consists of four steps:

- (i) Solve the linear equation system (3.58) for the strength of the bound point vortices Γ_j^b ;
- (ii) Evaluate the velocity of the free vortices $(dx_m/dt, dy_m/dt)$ from equation (3.65);
- (iii) Evaluate the vortex shedding rate $d\Gamma/dt$ and the averaged slip velocity \bar{V}_t at the edge from equation (3.62) and (3.63);

(iv) Update the free vortex sheets including newly shed vortex and the new positions of the previously shed vortices, preparing for the next time step.

By simulating the vortex shedding process associated with the oscillating thin plate is oscillating from the rest, we obtain the time variation of the total drag coefficient from equation (3.56).

Discrete vortex model (DVM)

(1) Motivation

The above VSM has two severe limitations. The first issue is that this method is very inefficient in calculation. Using VSM to obtain for determination of the viscous damping coefficient B^V in equation (3.1) takes about 50 times longer in computational time than the evaluation of the other hydrodynamic coefficients in WAMIT. This is because as the simulation time increases, more and more point vortices need to be tracked. Another issue is that VSM cannot run for sufficient long time for determining B^V . As Jones (2003) points out, as the plate is oscillating, the shed vortices do not convect away but remain in the vicinity of the plate. Hence, these vortices will interfere with the shedding process. Some of them may even hit the plate. These two limits of VSM motivates us to seek for a new model which can predict the damping coefficient B^V quickly and accurately.

Canals and Pawlak (2011) recently conducted an interesting experiment associated the vortex dynamics in oscillatory flow separation. According to their observations as illustrated in Figure 3-5, during the first half cycle of the oscillation, a shear layer is produced at the separation point and gradually rolls up into one vortex structure. This vortex structure keeps growing until the flow reverses. At the second half cycle, this vortex structure stops growing but breaking away from the edge of the plate. This vortex does not lose its strength, and is driven to the other side of the plate. At the same time, another opposite vortex structure starts to grow and rolls up at the edge just as the first one. Due to the interaction between the previous vortex and the plate, the growth of this opposite vortex structure is enhanced. By the end of the

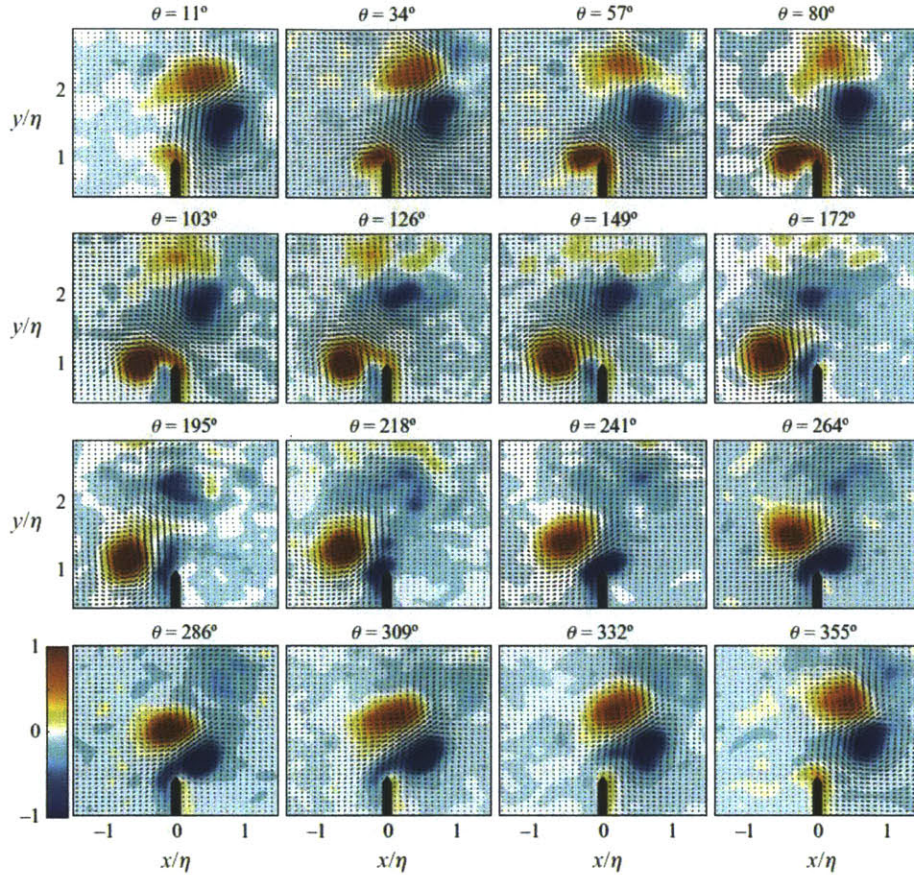


Figure 3-5: Sequence of phase-averaged spanwise vorticity and velocity vectors showing vortex pair formation for $KC = 1.07$. The phase of the oscillation, θ , is given in degrees at the top of each frame. The contour represents the strength of the vorticity. Note the ejection of a single vortex pair in the positive x/η direction, which is a repeatable feature for each cycle (from Canals & Pawlak 2011).

whole cycle, these two vortex structures both break away from the plate, and pair up. The vortex pair causes a self-induced motion from the plate at a particular shedding angle. In addition, this pair decay fairly fast, almost invisible after one period. This unidirectional vortex pairing process repeats with each cycle of oscillation. The overall vortex shedding patterns repeat from cycle to cycle.

Based on this observation, we develop a much simpler model – “Discrete Vortex Model” (DVM).

(2) The “Single Vortex” Approximation

In order to simplify the description, we again focus on one edge of the plate. In this model, the whole “rolled-up” vortex structure is replaced by a single concentrated point vortex. All the shed vortices are assumed to be accumulated to a point vortex $\Gamma(t)$. Since this point vortex represents a growing spiral vortex sheet attached to the edge of the plate, it should be connected to the edge by a cut representing the sheet, as shown in Figure 3-6. Such a structure of a point vortex plus cut is first proposed by Brown & Michael (1955) in studying the spiral vortex above the leading edge of a slender wing.

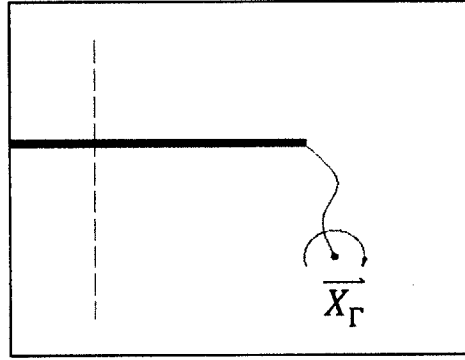


Figure 3-6: The sketch of the “single vortex” approximation. The whole vortex structure is represented by a single point vortex connected to the separation point by a cut. \vec{X}_Γ denotes the location of the point vortex.

(3) Growth of the Vortex

While the point vortex $\Gamma(t)$ is growing, the growth rate of the strength $d\Gamma/dt$ is determined by the Kutta condition just as before:

$$\frac{d\Gamma}{dt} = \frac{1}{2}(V_t^{-2} - V_t^{+2}) \quad (3.66)$$

where V_t^- and V_t^+ are the one-sided velocities at the edge.

When $d\Gamma/dt$ changes the sign, which means the magnitude of this vortex reaches the maximum, we break the cut and force this vortex to stop growing. At the same time, a new opposite vortex plus cut structure starts to grow similarly as the previous one until the growth rate $d\Gamma/dt$ changes the sign again. Therefore, different from VSM,

DSM has only two vortices to track during one cycle. This enhances the calculation efficiency considerably.

While the vortex is growing, its location should be easily determined by its local fluid velocity at the first thought. However, a free vortex with a growing strength in the fluid is incompatible with the Kelvin's Theorem. The original vortex sheets cannot sustain any forces. If we represent the whole vortex spiral into a concentrated point vortex only without the cut, its strength should not change with time, or if Γ changes, an unbalanced pressure jump will exist on any cut connecting the vortex and the edge of the plate. Brown & Michael (1954) proposed an approach in dealing with this issue. Let the vortex not be free, but subject to a Joukowski force, which cancels the unbalanced force on the cut. Based on this, the velocity of the vortex can be determined to be:

$$\vec{V}(\vec{x}_\Gamma) = \frac{1}{\Gamma} \left\{ \frac{d(\vec{x}_\Gamma \Gamma)}{dt} - \vec{x}_e \frac{d\Gamma}{dt} \right\} \quad (3.67)$$

(4) Decay of the Vortex

As observed in the experiments in Canals and Pawlak (2011), after the vortex structures break away from the plate, they pair up and decay fairly quickly (see Figure 3-5). The decay time scale t_d is of order of a period $O(T)$ (see Figure 3-7). According to Canals and Pawlak (2011), such a decay is not due to the viscosity diffusion, but the elliptical and centrifugal instability of the vortex structure. These vortex structures transitioned to 3-D turbulence rapidly before the viscous effects set in. The decay time scale t_d does not vary significantly with Re_ν , indicating that the three dimensional instability dominates over the viscous effects. In addition, we can see from Figure 3-7 that smaller KC results in a slightly longer t_d . This implies that t_d is a function of KC number. From the governing equation of vorticity is:

$$\frac{D\vec{\omega}}{Dt} = \vec{\omega} \cdot \nabla \vec{v} + \nu \nabla^2 \vec{\omega} \quad (3.68)$$

It is clear that the decay of the vortex strength should be an exponential function of viscosity. In our problem, there is no viscosity, but as mentioned before, KC

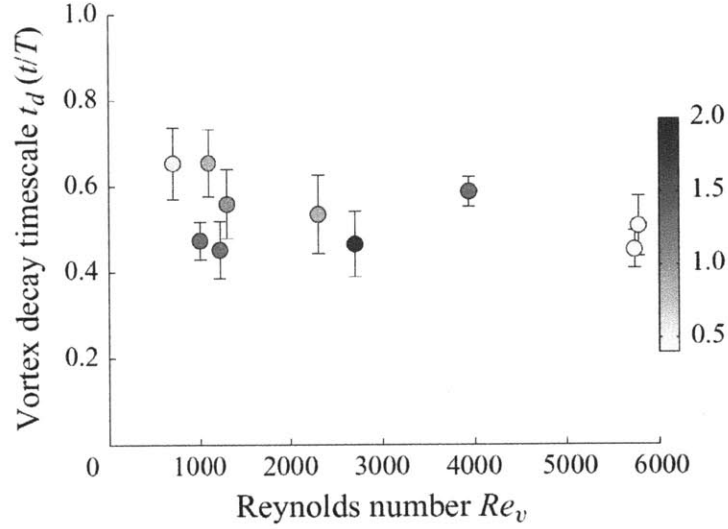


Figure 3-7: Non-dimensional vortex decay time scale t_d as a function of Re_ν , which is defined in terms of the vortex circulation. Error bars denote one standard deviation, and the grey shade of each symbol represents the value of KC for that experiment (from Canals & Pawlak, 2011)

number is defined as the ratio between the viscous effects and inertia effects. Based on these, we propose the following decay model:

$$\Gamma(t) = \Gamma_0 \cdot e^{-KC \frac{t-t_0}{T}} \quad (3.69)$$

where Γ_0 is the strength when the vortex breaks away from the plate at time t_0 . As for the location of the vortex when it is decaying, we set it to be free, convecting with the local fluid velocity.

Comparison and verification of VSM and DVM

For verification, we compare the predictions of VSM and DVM with the experimental data of Keulegan & Carpenter (1958). The experiments were designed to measure the unsteady hydrodynamic force on a submerged flat plate in a time-periodic flows.

Here we first use run number 42 as an example, in which the Reynolds number is 11400, and KC number is 3.8. Note that in our problem, KC is defined so that the non-dimensional period of oscillation is $2KC$.

In the experiment the plate is fixed while the fluid moves. In our computation, the plate moves in an otherwise calm water. Since the displacement of the plate can be neglected, the hydrodynamic force in these two cases are equivalent. Figure 3-8 shows the comparison of the total force coefficient $C(t)$ computed by these two methods with the experimental measurements. The vortex shedding rate $d\Gamma/dt$ and the total circulation shed at one edge $\Gamma(t)$ are also compared between VSM and DVM predictions. As shown in Figure 3-8, both models match the experimental data well. The accuracy of these two models is comparable. However, DVM is much more computationally efficient and can continue the simulation over many periods.

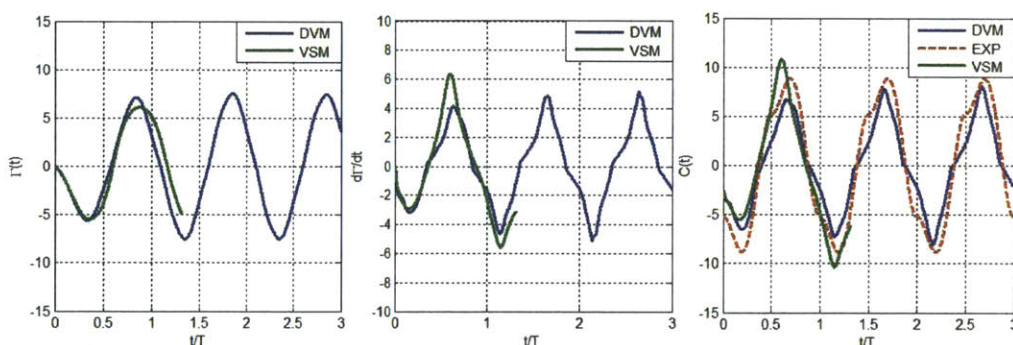


Figure 3-8: Comparison of the time variation of the total circulation shed at one edge of the plate $\Gamma(t)$, the vortex shedding rate $d\Gamma(t)/dt$ and the total force coefficient $C(t)$ for $KC = 3.8$. The blue solid line is the result of VSM, the green solid line is from DVM and the red dash line is the experimental result adopted from Keulegan & Carpenter (1958)

In addition to the force, VSM can also predict the wake shape. Figure 3-9 plots the positions of the plate and the free vortex sheets at different times during one cycle of oscillation. The black line in the first row is the results from Jones (2003). He used a similar vortex sheet model but with another version of unsteady Kutta condition. The second row in blue, however, is the calculation from VSM used in this thesis. As can be seen, the wake shapes are similar, verifying our VSM model.

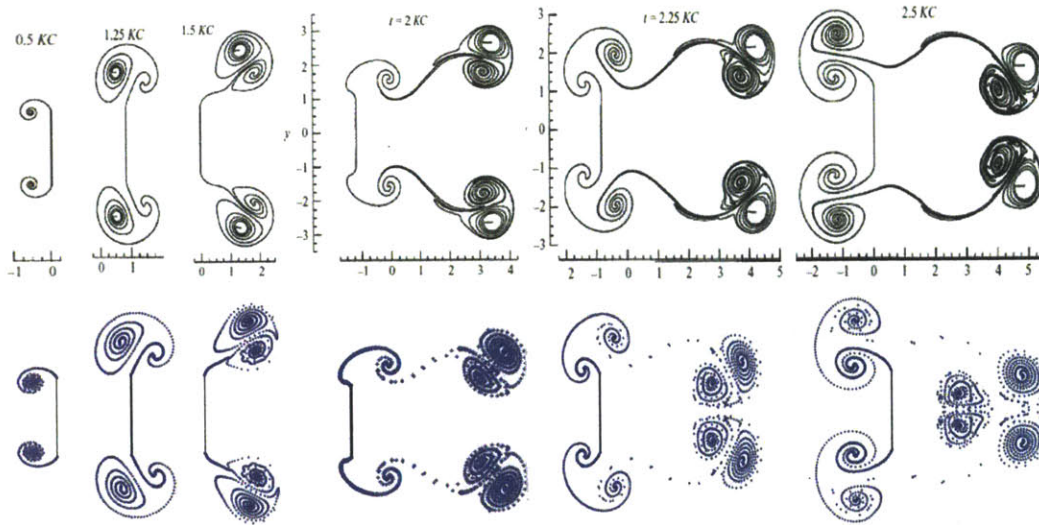


Figure 3-9: The wake induced by the sinusoidal oscillation of a flat plate in an otherwise stationary fluid with $KC = 3.8$ and $V(t) = V_0 \sin(2\pi t/T)$. The positions of the plate and the free vortex sheets at times $t = 0.5KC$, $1.25KC$, $1.5KC$, $2KC$, $2.25KC$, and $2.5KC$ are shown. The first row is the result adopted from Jones (2003). The second row is the result from our VSM. Our VSM uses a slightly different Kutta condition from the vortex sheet method used in Jones (2003).

Based on these comparisons, we can see that both methods can calculate the vortex induced drag of an oscillating plate. In addition, VSM can also predict the wake shape, but DVM can calculate the force much more quickly than VSM.

More comparisons of the DVM prediction with the experimental data are shown in Figure 3-10 for different KC numbers. The errors in the averaged peak value over a number of cycles of the DVM prediction compared to the experimental data are shown in Figure 3-11.

As can be seen from Figure 3-10 and 3-11, DVM with vortex decay model can correctly predict the trend of the drag coefficient as KC number varies. The error is less than 5% for $KC < 4$ and becomes larger when KC number increases but within 25% for KC up to near 10. This is because when KC is larger, the viscosity effects becomes more important. The vortex pattern would also become different. Rather than one vortex per half cycle, the flow past the body would form a wake containing a

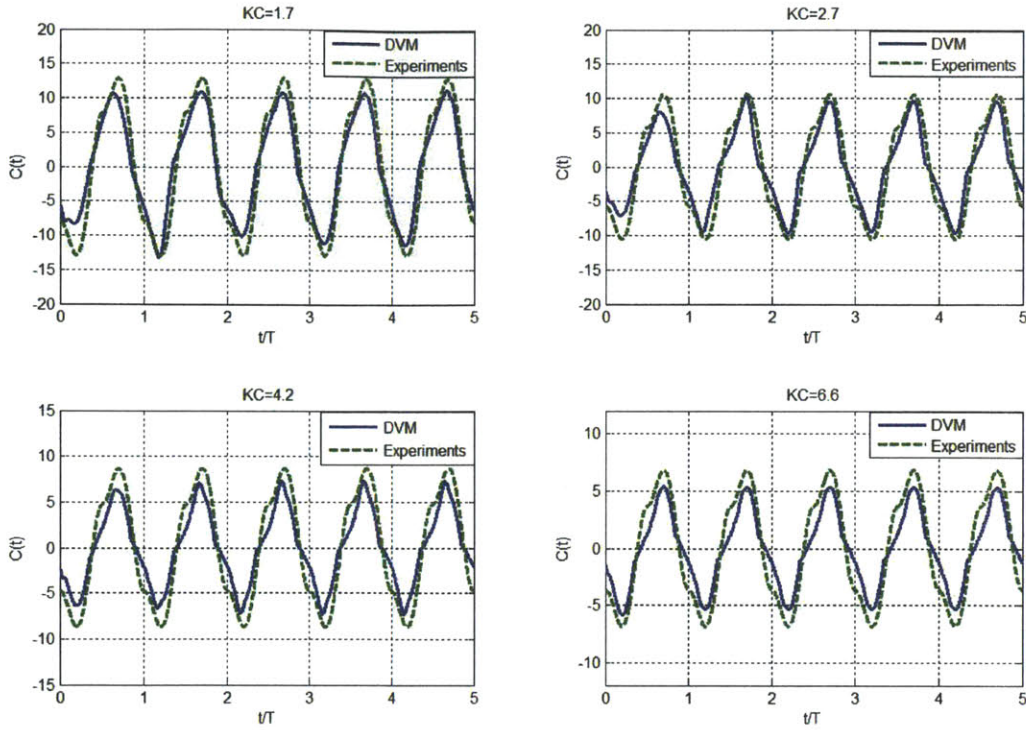


Figure 3-10: Comparisons of the time variation of the total force coefficient $C(t)$ between DVM and experimental data for $KC = 1.7, 2.7, 4.7$ and 6.6 . The experimental data is retrieved from Keulegan & Carpenter (1958)

number of vortices staggered as in the Von Karman Street. Then the “single vortex” approximation is no longer valid, so the error would become larger. Hence we here restrict our study within the low KC range ($KC \leq 10$).

3.3.2 Viscous drag of a circular oscillatory thin plate

In reality, the heave plate is a circular disk instead of an infinitely long plate. Therefore, we need to extend our models to the 3D axisymmetric cases. Such extension is straightforward but non-trivial. There will be a much more complicated interaction between vortices, and the self-induced velocity of a vortex ring. The key idea is to replace the point vortices in both VSM and DVM by vortex rings.

The problem formulation would be similar as before. An infinitely thin circular disk with radius R is oscillating with velocity $V = V_0 \sin \frac{2\pi}{T}t$ in an unbounded and

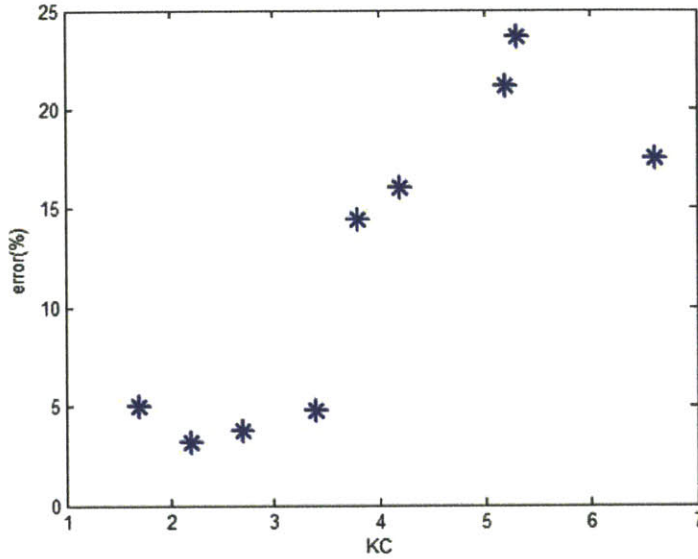


Figure 3-11: Difference in the average of peak values of the total force coefficient between DVM prediction and the experimental data for different KC's. The experimental data is retrieved from Keulegan & Carpenter (1958)

otherwise undisturbed fluid. We still assume infinite Reynold's number, and $KC \sim O(1)$, where $KC = V_0 T / R$.

Vortex ring sheet model (VRSM)

In this subsection, we follow the general idea of De Bernardinis et al. (1981) and Nitsche & Krasny (1994) who have already extended the vortex sheet model into 3D cases.

The basic idea is similar. We distribute a series of bound vortex rings with unknown strength Γ^b on the disk, and represent the vortex wake by a set of free vortex rings Γ^f of which the strengths are determined by the Kutta condition. In the following context, we use vortex ring sheet model (VRSM) to represent this idea. All the singularities of vortex rings should satisfy the kinematic boundary condition at N collocation points all the time.

$$\sum_j \Gamma_j^b [\tilde{v}_r n_r + \tilde{v}_z n_z] + \sum_m \Gamma_m^f [\tilde{v}_r n_r + \tilde{v}_z n_z] = V_{ni}, \quad i = 1, 2 \dots N \quad (3.70)$$

where $\vec{n} = (n_r, n_z)$ is the normal vector of the disk. V_{ni} is the normal velocity of the plate at the i -th collocation point. $(\tilde{v}_r, \tilde{v}_z)$ is the velocity at (r, z) induced by a unit vortex ring at (r', z') . This can be obtained from Lamb (1993):

$$\tilde{v}_z = \frac{1}{2\pi[(r-r')^2 + (z-z')^2 + \delta^2]^{\frac{1}{2}}} \left\{ \mathcal{K}(q) - \frac{r^2 - r'^2 + (z-z')^2 + \delta^2}{(r-r')^2 + (z-z')^2 + \delta^2} \mathcal{E}(q) \right\} \quad (3.71)$$

$$\tilde{v}_r = \frac{-(z-z')}{2\pi r[(r-r')^2 + (z-z')^2 + \delta^2]^{\frac{1}{2}}} \left\{ \mathcal{K}(q) - \frac{r^2 + r'^2 + (z-z')^2 + \delta^2}{(r-r')^2 + (z-z')^2 + \delta^2} \mathcal{E}(q) \right\} \quad (3.72)$$

where $\mathcal{K}(q)$ and $\mathcal{E}(q)$ are the complete elliptic integrals of the first and second kind with the argument:

$$q = \frac{4rr'}{(r+r')^2 + (z-z')^2 + \delta^2} \quad (3.73)$$

where δ is the vortex-blob smoothing parameter. $0 \leq \delta \leq 1$ if (r', z') is on the vortex ring sheets. δ is set to be zero if (r', z') is on the plate.

The circulation shedding rate at the edge of the disk is determined from the following unsteady Kutta condition used in Nitsche & Krasny (1994):

$$\frac{d\Gamma}{dt} = \frac{1}{2}(V_r^{-2} - V_r^{+2}) \quad (3.74)$$

where V_r^{-2} , V_r^{+2} are the slip velocity at the upper and lower edge of the disk. They satisfy:

$$V_r^- - V_r^+ = \gamma_e, \quad \frac{1}{2}(V_r^+ + V_r^-) = \bar{V}_r \quad (3.75)$$

where γ_e is the bound vortex sheet strength at the edge, and \bar{V}_r is the average slip velocity.

The nascent free vortex ring is shed from the edge at the velocity (\bar{V}_r, V_n) . Then it convects at the local fluid velocity.

Discrete vortex ring model (DVRM)

The extension of the DVM to discrete vortex ring model (DVRM) is similar. Such an extension is reasonable because similar vortex shedding pattern was also observed in experiments for a fixed thin disk in oscillatory flow at low KC number (Lake et al.,

2010; De Bernardinis et al. 1981). During the first half cycle, the vorticity shed tends to roll up into a single vortex ring. As the flow slows down, the flow at the edge of the disk reverses and a second vortex sheet of opposite magnitude starts to emanate, and be shed at the second half cycle. At the same time, the first vortex ring is interacting with part of the second ring to form a vortex ring pair, convecting away from the disk. The residual part of the second ring is not that strong, thereby amalgamated by the third vortex ring at the beginning of the second cycle. The third vortex sheet develops into an organized vortex ring similar to the first vortex ring. Thus this whole pattern is repeated from cycle to cycle. As for the vortex ring pair during the first cycle, they also decay fairly fast because of the instability and viscous diffusion, so it is very difficult to follow their motion at greater distances. These suggest that both the “single vortex ring” approximation and the decay model can be used in the 3D axisymmetric case.

We represent the vortex ring structure by a single vortex ring $\Gamma(t)$ plus a surface cut transporting the vorticity to this vortex ring. The vortex shedding rate satisfies the same unsteady Kutta condition. The position of this growing vortex ring is determined by the condition that the total force on the ring and the cut is zero. When $d\Gamma/dt$ changes the sign, this ring stops growing but start to decay, and move with the local velocity. The decaying rate is also the same as the 2D case. Meanwhile, a new opposite vortex ring starts to grow until the next change in sign of the vortex shedding rate.

Comparison and verification of VRSM and DVRM

Using both VRSM and DVRM, we can calculate the vorticity and velocity distribution, then obtain the pressure field based on the Bernoulli’s equation. The unsteady axial force acting on the disk is the integration of the pressure over the entire surface. However, it is usually convenient to decouple this force into two components. One associates with the inertia effects of the attached flow around the disk, i.e., the added mass. The other is due to the vorticity shedding. We can write this total force in the

form (Graham 1980):

$$F(t) = \frac{4}{3}\pi\rho\dot{V}R^3C_{M0} + \frac{1}{2}\pi\rho V^2R^2C_{FV}(t) \quad (3.76)$$

where C_{M0} is the inertia coefficient, and has a value of 0.637 for a circular disk. C_{FV} is the force coefficient due to vortex shedding.

Here we first compare C_{FV} for different KC 's based on VRSM, DVRM and the results in De Bernardinis et al. (1981). In De Bernardinis et al (1981), a similar vortex ring sheet model is used. As for the Kutta condition, they assumed that the vortex shedding is governed by the flow characteristics near to the geometrical singularity in the boundary. They considered the shedding to be locally two-dimensional, so a 2D Kutta condition is applied. Figure 3-12, 3-13 and 3-14 show the time evolution of the vortex force coefficients $C_{FV}(t)$ for different KC numbers based on different models. Figure 3-12 is the result from our DVRM code, Figure 3-13 is the result from VRSM, and Figure 3-14 is the calculation from De Bernardinis, et al. (1981).

Usually we write the force in the form of Morison's equation (Keulegan & Carpenter 1956):

$$F(t) = \frac{4}{3}\pi\rho R^3C_M + \frac{1}{2}\pi\rho V|V|R^2 \quad (3.77)$$

where

$$C_M = C_{M0} + \frac{3}{4\pi} \int_0^T C_{FV}(t) \cos \frac{2\pi}{T} t dt \quad (3.78)$$

$$C_D = \frac{3\pi}{4T} \int_0^T C_{FV}(t) \sin \frac{2\pi}{T} t dt \quad (3.79)$$

Figure 3-15 provides the comparison of C_D as KC number varies. The left figure is from our VRSM and DVRM codes, while the right one is the result from De Bernardinis et al. (1981).

Figure 3-12, 3-13, 3-14 and 3-15 show that both VRSM and DVRM agree well with the result of De Bernardinis et al. This verifies the extension of our simple model from 2D to 3D axisymmetric problems. As can be seen from Figure 3-15, the drag coefficient decreases as KC number increases. Note that DVRM is more reliable in

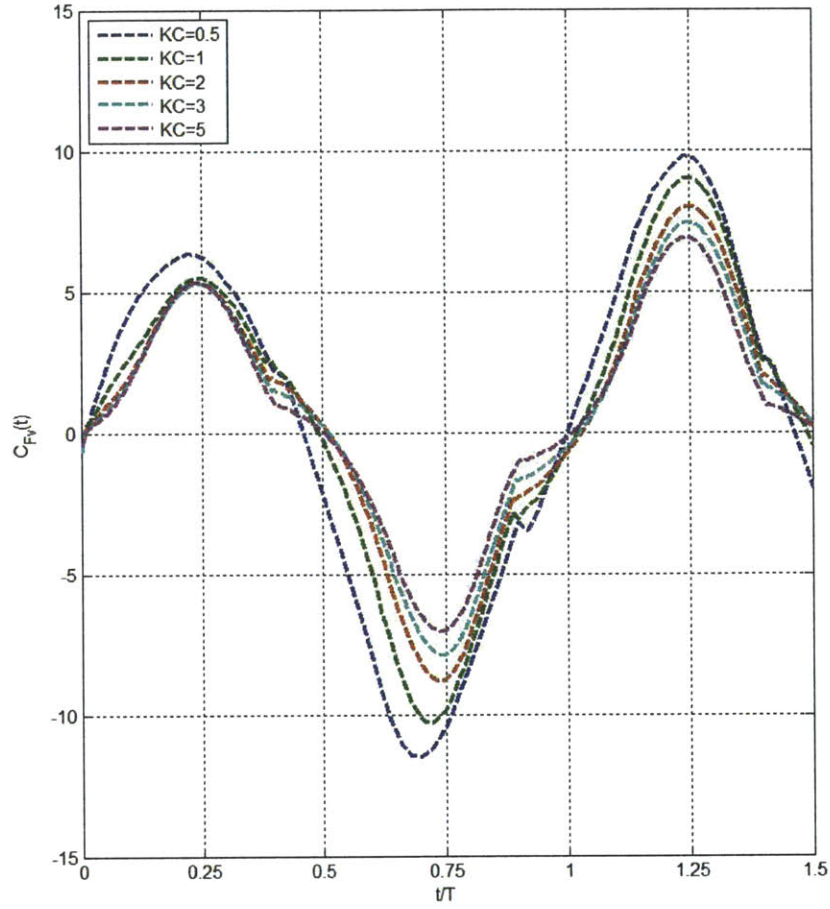


Figure 3-12: Time variation of the force coefficient due to vortex shedding C_{FV} of an infinitely thin circular disk oscillating in an unbounded, inviscid, and otherwise undisturbed fluid based on DVRM, for $KC = 0.5, 1, 2, 3$ and 5

obtaining the drag coefficient for $KC > 2$.

After obtaining this drag coefficient C_D , we can easily calculate the viscous damping coefficient B^V in equation (3.1) using the DVRM (Cozijn et al. 2005). For heave motion,

$$B_{22}^V = \frac{1}{2} \rho C_D A_s \quad (3.80)$$

where A_s is the extended area of the heave plate relative to the keel of the platform. KC is defined as:

$$KC = 2\pi \frac{\Xi_{20}}{R_0} \quad (3.81)$$

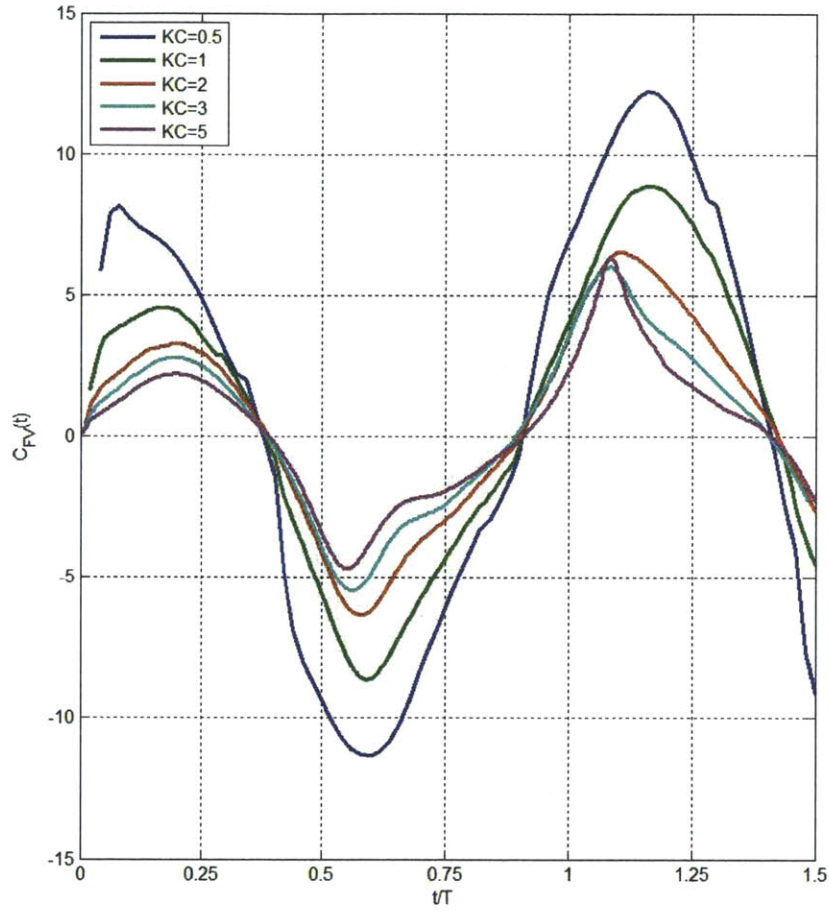


Figure 3-13: Time variation of the force coefficient due to vortex shedding C_{FV} of an infinitely thin circular disk oscillating in an unbounded, inviscid, and otherwise undisturbed fluid based on VRSM, for $KC = 0.5, 1, 2, 3$ and 5

where Ξ_{20} is the amplitude of the heave oscillation.

3.4 Solution to the motion equation in regular waves

3.4.1 Procedure of solving the motion equation

We are now in the position where we can handle all the hydrodynamic coefficients in equation (3.1). The solution to this equation would be derived in this section based on the combination of the potential flow theory (see section 3.2) and the vortex damping

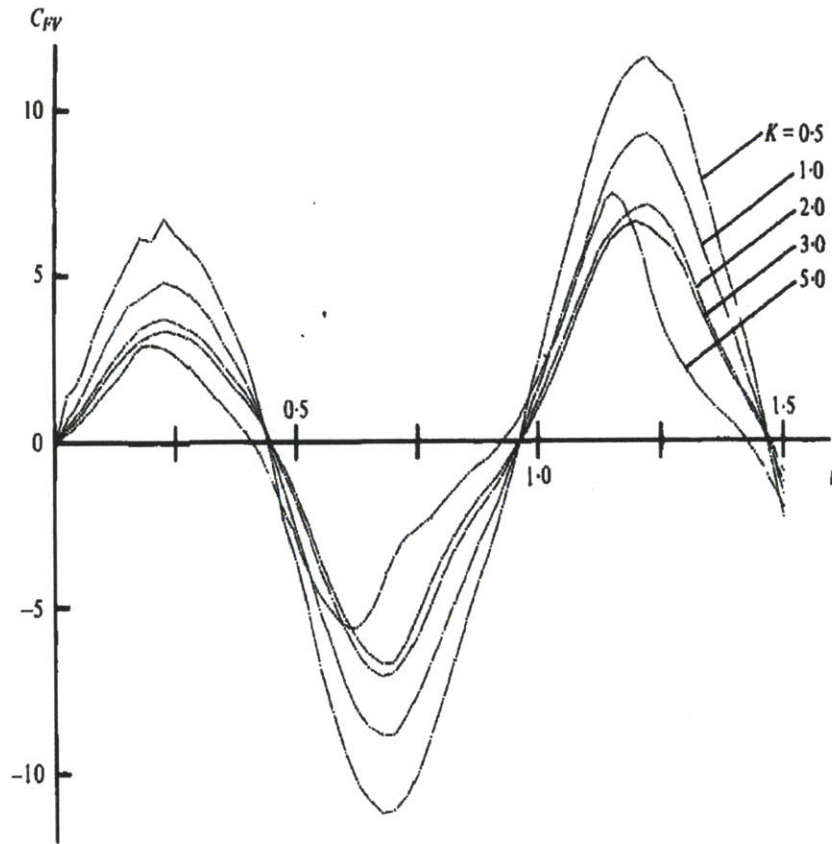


Figure 3-14: Time variation of the force coefficient due to vortex shedding C_{FV} of an infinitely thin circular disk oscillating in an unbounded, inviscid, and otherwise undisturbed fluid for $KC = 0.5, 1, 2, 3$ and 5 (from De Bernardinis et al. 1981)

model (see section 3.3). A flow chart of solving the equation of motion in regular waves (3.1) is illustrated in Figure 3-16. We first input the geometric information of the dimensions, weights and inertial parameters based on the estimations in Chapter 2. Then we obtain all the linear hydrodynamic coefficients including added mass $[A]$, linear wave damping $[B^p]$, restoring force $[C]$ and wave exciting force $[X]$ via WAMIT. The viscous damping coefficients due to the vortex shedding of the heave plate is obtained through our newly developed model DVRM. Plugging all these coefficients and the inertial parameters of the floating body into the equation of motion (3.1), we can obtain the solution which is usually called “response amplitude operator” (RAO). RAO is defined as the ratio between the amplitude of the motion

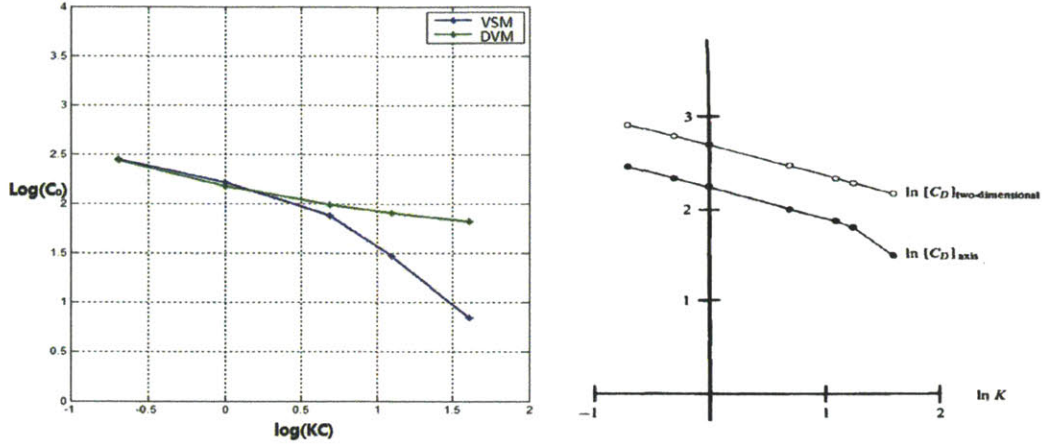


Figure 3-15: Comparisons in Drag Coefficients C_D as a function of KC number in log scale. The left figure is the result from the codes used in this thesis. The blue line is from VRSM, while the green line is from DVRM. The right figure is the result adopted from De Bernardinis, et al. (1981)

response and the amplitude of the incoming regular wave. In the next subsection, we will present the derivation of the RAO given that all the coefficients in the motion equation are known.

3.4.2 Derivation of the RAO

Let us first recall the equation of motion of a floating body in regular waves.

$$(M_{ij} + A_{ij})\ddot{\xi}_j + B_{ij}^P \dot{\xi}_j + B_{ij}^V |\dot{\xi}_j| \dot{\xi}_j + C_{ij} \xi_j = AX_i \quad (i, j = 1, 2, \dots, 6) \quad (3.82)$$

As can be seen from this equation, it is difficult to be solved because of the nonlinear term associated with the viscous damping. Let us first ignore this nonlinear term. Since for such spar-like platform the key mode is the heave motion ξ_{22} (Sclavounos 2013), the response amplitude operator (RAO) for heave motion without viscous damping would be:

$$\frac{\Xi_2}{A} = \frac{X_2}{-\omega^2(A_{22} + M) + i\omega B_{22}^P + C_{22}} \quad (3.83)$$

If we take the viscous term into consideration, we use the linearization technique

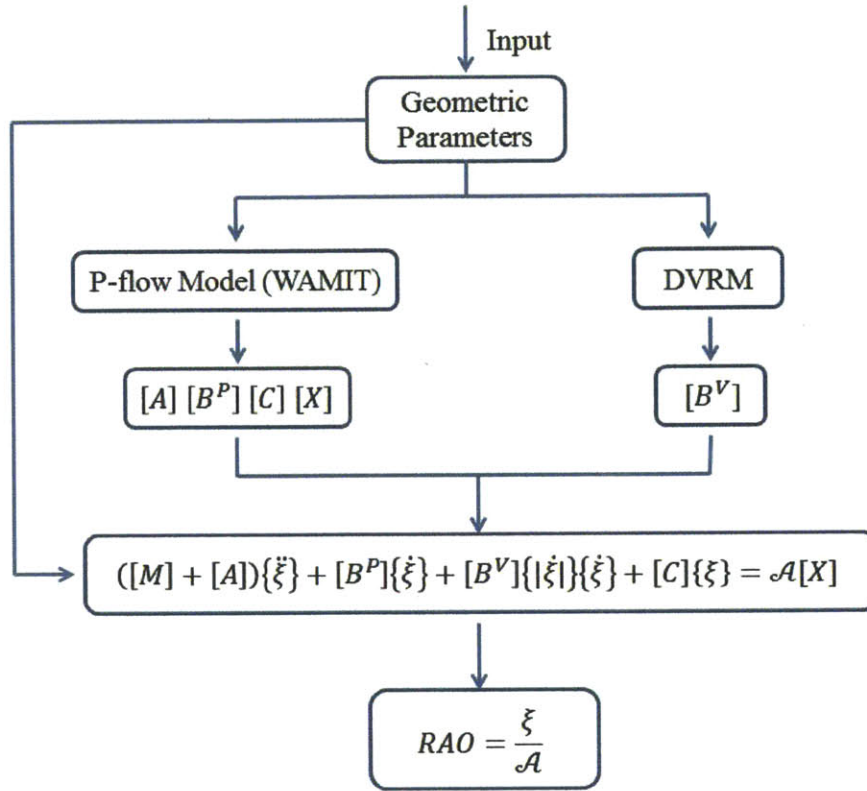


Figure 3-16: The flow chart of solving the dynamic motion equation of a floating body in regular waves in combination of the potential flow theory (WAMIT) and the vortex damping model (DVRM)

to this term in order to apply the frequency domain analysis based on the linear wave induced motion theory. Note that the viscous damping effect is much more important than the wave damping term, therefore we can ignore the B_{22}^P term for simplicity (Sadeghi et al. 2004). Assume the motion response ξ_2 and the wave exciting force X_2 to be:

$$\xi_2 = \Xi_{20} \cos(\omega t - \beta_2) \quad (3.84)$$

$$X_2 = X_{20} \cos(\omega t - \theta_2) \quad (3.85)$$

where ω is the incident wave frequency.

Then the motion equation in heave would be :

$$\begin{aligned} & [C_{22} - \omega^2(M + A_{22})]\Xi_{20} \cos(\omega t - \beta_2) \\ & - \omega^2 B_{22}^V \Xi_{20}^2 \sin(\omega t - \beta_2) |\sin(\omega t - \beta_2)| = X_{20} \cos(\omega t - \theta_2) \end{aligned} \quad (3.86)$$

Using the first term of the Fourier series expansion of $\sin(\omega t - \beta_2) |\sin(\omega t - \beta_2)|$, this nonlinear term can be approximated as:

$$\sin(\omega t - \beta_2) |\sin(\omega t - \beta_2)| \simeq \frac{8}{3\pi} \sin(\omega t - \beta_2) \quad (3.87)$$

Therefore, the original motion equation in heave can be written as:

$$(M + A_{22})\ddot{\xi}_2 + B_{22}^{eq}\dot{\xi}_2 + C_{22}\xi_2 = X_2 \quad (3.88)$$

where the equivalent damping term B_{22}^{eq} is defined as:

$$B_{22}^{eq} = \frac{8}{3\pi} \omega B_{22}^V \Xi_{20} \quad (3.89)$$

where B_{22}^V is derived in equation (3.80).

Equation (3.88) looks like a linear differential equation, but actually $B_{22}^{eq}\dot{\xi}_2$ is still a nonlinear term with respect to the motion amplitude.

The conventional methods of solving equation (3.88) is by iteration, but this equation can also be solved without iteration (Sadeghi et al. 2004). Let us first write the equation in the complex notation.

$$\begin{aligned} & [C_{22} - \omega^2(M + A_{22})]\Xi_{20} \operatorname{Re}\{e^{-i(\omega t - \beta_2)}\} \\ & - \omega^2 B_{22}^V \Xi_{20}^2 \operatorname{Re}\{ie^{-i(\omega t - \beta_2)}\} = X_{20} \operatorname{Re}\{e^{-i(\omega t - \theta_2)}\} \end{aligned} \quad (3.90)$$

or

$$\begin{aligned} & Re\{[C_{22} - \omega^2(M + A_{22})]\Xi_{20}e^{-i\omega t}e^{i\beta_2} \\ & - \frac{8}{3\pi}i\omega^2 B_{22}^V \Xi_{20}^2 e^{-i\omega t}e^{i\beta_2} - X_{20}e^{-i\omega t}e^{i\theta_2}\} = 0 \end{aligned} \quad (3.91)$$

or

$$\begin{aligned} & Re\{([C_{22} - \omega^2(M + A_{22})]\Xi_{20}e^{i\beta_2} \\ & - i\omega^2 \bar{B}_{22} \Xi_{20}^2 e^{-i\beta_2} - X_{20}e^{i\theta_2})e^{-i\omega t}\} = 0 \end{aligned} \quad (3.92)$$

where $\bar{B}_{22} = \frac{8}{3\pi}B_{22}^V$. Assuming that

$$Z_1 = [C_{22} - \omega^2(M + A_{22})]\Xi_{20}e^{i\beta_2} - i\omega^2 \bar{B}_{22} \Xi_{20}^2 e^{-i\beta_2} - X_{20}e^{i\theta_2} \quad (3.93)$$

$$Z_2 = e^{-i\omega t} \quad (3.94)$$

Therefore, equation (3.92) can be written as

$$Re(Z_1 Z_2) = 0 \quad (3.95)$$

$$Re(Z_1) \cos \omega t + Im(Z_1) \sin \omega t = 0 \quad (3.96)$$

To guarantee the above equation to be true for an arbitrary ω , it is necessary that $Re(Z_1) = 0$ and $Im(Z_1) = 0$. Equivalently,

$$Z_1 = 0 \quad (3.97)$$

Substituting for Z_1 we can obtain

$$[C_{22} - \omega^2(M + A_{22})]\Xi_{20}e^{i\beta_2} - i\omega^2 \bar{B}_{22} \Xi_{20}^2 e^{-i\beta_2} = X_{20}e^{i\theta_2} \quad (3.98)$$

or

$$[C_{22} - \omega^2(M + A_{22})]\Xi_{20} - i\omega^2 \bar{B}_{22} \Xi_{20}^2 = X_{20}e^{i(\theta_2 - \beta_2)} \quad (3.99)$$

Taking the modulus of both sides of equation (3.99) yields

$$\sqrt{[C_{22} - \omega^2(M + A_{22})]^2 \Xi_{20}^2 + [\omega^2 \bar{B}_{22}]^2 \Xi_{20}^4} = X_{20} \quad (3.100)$$

$$[\omega^2 \bar{B}_{22}]^2 \Xi_{20}^4 + [C_{22} - \omega^2(M + A_{22})]^2 \Xi_{20}^2 = X_{20}^2 \quad (3.101)$$

Let us introduce the following substitution.

$$x = \Xi_{20}^2 \quad (3.102)$$

Then equation (3.101) can be written as a quadratic equation in x , which can be solved without iteration.

$$ax^2 + bx - c = 0 \quad (3.103)$$

where

$$a = [\omega^2 \bar{B}_{22}]^2, \quad b = [C_{22} - \omega^2(M + A_{22})]^2, \quad c = X_{20}^2 \quad (3.104)$$

It is easy to solve this equation to obtain:

$$x = \frac{-b \pm \sqrt{b^2 + 4ac}}{2a} \quad (3.105)$$

Therefore,

$$\Xi_{20} = \sqrt{\frac{-b \pm \sqrt{b^2 + 4ac}}{2a}} \quad (3.106)$$

Then the response amplitude operator in regular waves (RAO) can be defined as the ratio between the response and the incident wave amplitude A .

$$RAO = \sqrt{\frac{-b \pm \sqrt{b^2 + 4ac}}{2a}} / A \quad (3.107)$$

Note that the RAO defined in equation (3.107) is obtained by direct solution of the nonlinear equation of motion for a particular wave amplitude because the wave exciting force X_{20} is proportional to the incident wave amplitude A . Therefore, the above RAO is different from the traditional one. It also varies with the wave

amplitude (Sadeghi et al. 2004). Here for simplicity we ignore this variation with the wave amplitude when predicting the motion performance in sea-states in the following section.

3.5 Motion Response in Ocean Environments

3.5.1 Description of ocean waves

RAO reflects the response of the platform to a regular plane wave with unit amplitude assuming that the platform is a linear system. However, what we need to know in reality is the response of the platform to the irregular waves. The complexity of ambient wave motions in the ocean is evident. They are not only dispersive, but random. However, in spite of the randomness, ocean waves can be modelled by a linear superposition of sinusoids of random phase which satisfy normality via the central limit theorem. Then the wave elevation is Gaussian distributed with zero mean and variance σ^2 . In this subsection, we will summarize the description of the ocean waves from Newman (1977).

In general, the ocean wave elevation can be expressed in the form:

$$\eta(x, z, t) = Re \int dA(\omega, \theta) \exp[-ik(x \cos \theta + y \sin \theta) + i\omega t] \quad (3.108)$$

where $A(\omega, \theta)$ represents the amplitude of a plane wave of frequency ω propagating in the direction of θ .

Given that in our case, the platform is axisymmetric, we need to consider the uni-directional wave spectrum:

$$\eta(x, t) = Re \int dA(\omega) \exp(-ikx + i\omega t) \quad (3.109)$$

Here the wave number k is defined in terms of the frequency ω by the dispersion relation in deep water.

$$\omega^2 = gk \quad (3.110)$$

Then the average energy density can be computed as follows:

$$\overline{\eta^2} = \frac{1}{2} \overline{\int dA(\omega) \exp[-ik(\omega)x + i\omega t] \times \int dA^*(\omega') \exp[ik'(\omega')x - i\omega't]} \quad (3.111)$$

where (*) represents the complex conjugate. Therefore,

$$\overline{\eta^2} = \frac{1}{2} \int dA(\omega)dA^*(\omega) = \int_0^\infty S(\omega)d\omega \quad (3.112)$$

where $S(\omega)$ is defined as the wave spectrum density. Then the total mean energy of the wave spectrum of the wave system per unit area of the free surface is:

$$\bar{E} = \rho g \int_0^\infty S(\omega)d\omega \quad (3.113)$$

Therefore, the wave spectrum density defined previously $S(\omega)$ represents the wave energy.

It can be proved that the variance of the wave elevation σ^2 satisfies:

$$\sigma^2 = \int_0^\infty S(\omega)d\omega \quad (3.114)$$

The wave spectrum can be estimated from wave measurements. It assumes that we can describe the sea as a stationary random process. This means in practice we consider a limited time period ranging from 0.5 hour to around 10 hours. This is usually referred to as a short-term description of the sea.

Usually we use the following two parameters to characterize the wave spectrum. One is the significant wave height H_s defined as the mean of the one third highest waves. The other is the peak wave period T_p corresponding to the peak frequency of the spectrum.

$$m_k = \int_0^\infty \omega^k S(\omega)d\omega \quad (3.115)$$

$$H_s = 4\sqrt{m_0} = 4\sigma \quad (3.116)$$

$$T_p = 1.408T_2 \quad (3.117)$$

where

$$T_2 = 2\pi(m_0/m_2)^{\frac{1}{2}} \quad (3.118)$$

The Pierson-Moskowitz spectrum is usually used for fully developed seas. In order to overcome the limitation of fully developed seas, a two parameter spectrum was developed which is called the Modified Pierson-Moskowitz spectrum (International Towing Tank Conference (ITTC); Michel 1999). In this thesis, we use this spectrum to predict the motion of our mini-platform.

$$S(\omega) = \frac{5H_s\omega_p^4}{16\omega^5} e^{-1.25(\frac{\omega}{\omega_p})^{-4}} \quad (3.119)$$

where $\omega_p = 2\pi/T_p$.

3.5.2 Motions of general bodies in irregular waves

With the spectral description of ocean waves given in the preceding subsection, we can use the RAO to predict the motion behaviour of a floating body in irregular seas. If the ocean waves are described by equation (3.109), and if the response of the body to each wave component is defined by a linear transfer function $RAO(\omega)$ in equation (3.107), then the body response would be (St Denis & Pierson 1953; Newman 1977):

$$\xi_j(t) = Re \int RAO_j(\omega) e^{i\omega t} dA(\omega) \quad (3.120)$$

The assumption used here is that everything is linear and therefore the linear superposition is used.

Like the waves, the response in equation (3.120) is also a random variable. Its variance is defined as (Sclavounos 2013):

$$\sigma_\xi^2 = \int_0^\infty S(\omega) |RAO(\omega)|^2 d\omega \quad (3.121)$$

Then similarly, we can define the significant motion response as:

$$\xi_s = 4\sigma_\xi \quad (3.122)$$

This significant value ξ_s is the mean motion height of the one third highest response, which can reflect the magnitude of the motion amplitude of a floating body in waves. In the next chapter, we will use the models and methods elaborated in this chapter to design the geometry of the hull for our mini-platform. ξ_s obtained in this chapter would be used as an important parameter to measure the motion performance of the platform.

Chapter 4

Conceptual Design and Analysis for the Mini-platform

In the last chapter, a description of the hydrodynamic models and numerical methods used for design is presented. In this chapter, we will apply these models and methods to seek for a hull shape for a small mono-column floating platform with a satisfactory motion behaviour.

The content of this chapter is as follows. First, we use the potential theory model (see Chapter 3, section 3.2) to obtain a general hull shape on the basis of a spar with the same displacement. Next, an example of initial design compared with the spar is given to show the advantage of our design in suppressing the motion in waves. Finally, we carry out a systematic analysis to study the effect of different geometric parameters on the heave motion of the platforms.

4.1 Hull shape evolution of the mini-platform

In this section, we will illustrate the evolution from a circular cylinder (spar) to the general shape of our mini-platform based on the potential flow theory.

Here we use the heave motion amplitude of a single-column floating platform as the design criteria. The heave motion is uncoupled with other modes. The RAO for heave mode without viscous damping is derived from equation (3.83).

$$\frac{\Xi_2}{A} = \frac{X_2}{-\omega^2(A_{22} + \Delta) + i\omega B_{22} + C_{22}} \quad (4.1)$$

The natural frequency in heave is:

$$\omega_n = \sqrt{\frac{C_{22}}{A_{22} + \Delta}} \quad (4.2)$$

When the incident wave frequency is at or close to this resonant frequency, the body would experience a response of large amplitude. Therefore, we should shift the natural frequency of the platform far from the peak frequency of the design wave spectrum. One way to do that is to increase the natural frequency of the platform. This requires to increase the stiffness of the body C_{22} . This is the idea used in the design of TLP, which achieves a high natural frequency by attaching several stiffeners at the keel of the platform to the sea floor. However, these tendons are costly in installing and limited by the water depth. Therefore, we choose to lower the natural frequency of the platform. In Gulf of Mexico, the general peak period of the waves is around 10 ~ 14s (ITTC), so the natural period of our platform in heave motion should be at least 20s. It is well known that spars achieve a small natural frequency by increasing the displacement in equation (4.2). In our case, the displacement is restricted. To achieve this purpose, we developed a new design based on modifications from spars.

In addition to shifting the natural frequency, we should also keep the RAO low for all the frequencies, especially near the resonance frequency. Based on equation (4.1), this requires to reduce the wave exciting force and increase the damping, in general.

In summary, the suppression of the heave motion can be achieved by:

- (1) Reducing the stiffness
- (2) Increasing the added mass
- (3) Reducing the wave exciting force
- (4) Increasing the damping

which all help move the heave natural frequency to the lower value.

We start with a preliminary design of a spar with draft $H = 30 \text{ m}$, radius $R_{avg} = 11.3 \text{ m}$, and displacement $\forall = 12,000 \text{ m}^3$. The dimensions for our platform are defined in Chapter 2, section 2.1 (see Figure 2-1).

4.1.1 Reduce the stiffness

C_{22} measures the stiffness of the platform in heave. $C_{22} = \rho g S$, where S is the water-plane area (see Chapter 3, section 3.2). Therefore, we should decrease the radius R_1 of the water plane area to reduce the stiffness.

4.1.2 Increase the added mass

For a quick estimation of the heave added mass of such a buoy, we assume the added mass is frequency-independent, and ignore the influence of the free surface (Sclavounos, 2013). The added mass of a spar-like floating body can be estimated as a half sphere at the bottom, i.e., $A_{22} \propto R_2^3$, where R_2 is the radius of the keel. Therefore, R_2 should be increased to achieve a large heave added mass.

To justify our estimation, let us consider a floating body composed of two circular cylinders with radius R_1 and R_2 . Here we fix the displacement and the draft of the body, and use WAMIT to examine the trend of the heave added mass of such a body as R_2/R_{avg} varies.

Figure 4-1 shows the variation of the heave added mass coefficient as a function of the dimensionless oscillation frequency and R_2/R_{avg} . The projection of the contour surface on the horizontal plane justifies the near independence of the added mass on the frequency. From the linear fitting line in Figure 4-2, we can see that $A_{22}/\rho\pi R_{avg}^3 \propto (R_2/R_{avg})^3$. This justifies the previous estimation and also implies that the heave added mass is mainly an end effect.

As mentioned in previous chapters, a thin heave plate is attached at the keel in our design to increase added mass. Therefore, at phase I of the hull evolution, we obtain a design of two cylinders with a heave plate (see Figure 4-3).

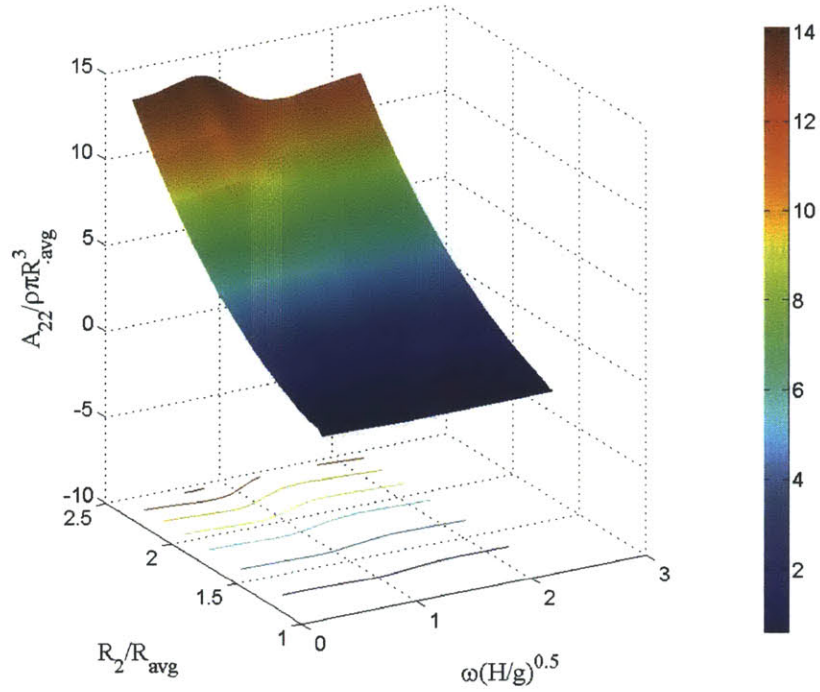


Figure 4-1: Variation of the heave added mass coefficient as a function of the dimensionless oscillation frequency and R_2/R_{avg} for a floating body composed of two cylinders with radius R_1 and R_2 respectively. The displacement and the draft of the body are fixed. R_{avg} is the radius of a circular cylinder with the same displacement and draft. The calculation results are from WAMIT.

4.1.3 Reduce the wave exciting force

Semi-submersibles and TLPs utilize the column/pontoon effect to cancel heave exciting force. This may suggest us to add a shoulder into our design (Haslum & Faltinsen, 1999). The dynamic pressure force acting on this shoulder to some extent can counteract the exciting force at the bottom (see Figure 4-5). Due to the exponential decay in pressure with depth, a higher shoulder can provide a greater cancellation effect in wave exciting force. This is verified by the following calculation. We still consider a body composed of two cylinders with radius R_1 and R_2 , respectively. The variation of the wave exciting force coefficient as the position of the shoulder H_1/H varies is plotted in Figure 4-4, where H_1 is the length of the upper cylinder. Here we fix R_1/R_{avg} , R_2/R_{avg} and H .

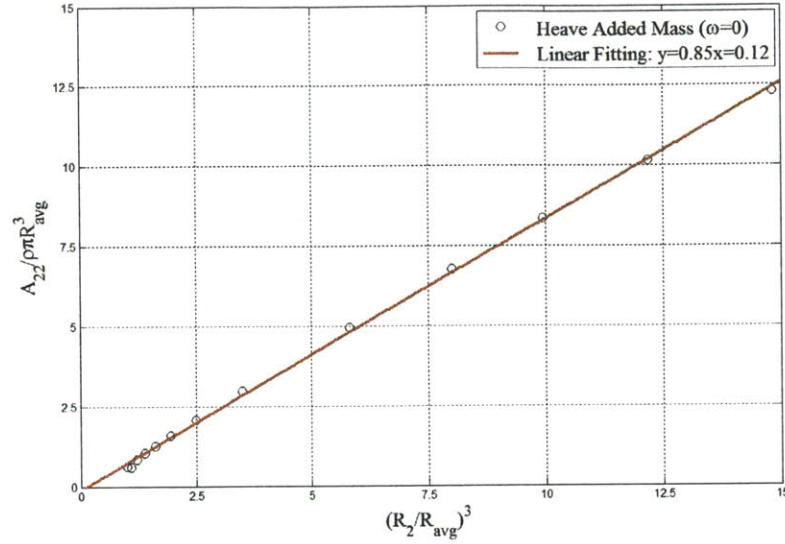


Figure 4-2: Variation of the heave added mass coefficient as a function of $(R_2/R_{avg})^3$ for a floating body composed of two cylinders with radius R_1 and R_2 respectively. The displacement and the draft of the body are fixed. R_{avg} is the radius of a circular cylinder with the same displacement and draft. The red curve is the linear fitting line based on the scattered points obtained from WAMIT.

Figure 4-4 shows the variation of the heave exciting force for designs with different shoulder positions and a cylinder with no shoulder. As can be seen, this shoulder results in a smaller wave exciting force at lower frequencies, especially near the resonance. In addition, a higher shoulder can result in a smaller exciting force in the lower frequencies, but also leads to a larger force in the higher frequencies. Note that RAO in heave motion is usually small in these high frequencies. Therefore, a high shoulder is appreciated in the design from the consideration of reducing exciting forces.

However, such a horizontal shoulder is a rapid variation in the cross section, so it should be deep enough to prevent it from penetrating the free surface. Furthermore, we should always guarantee the hydrostatic stability during all the design phases. These imply that we need to make a trade-off in determining the position of the shoulder. One trial is to modify the shoulder from a flat one to an oblique one. To see the effect of the inclination of the shoulder α on the wave exciting force, we calculate the heave exciting force for different α 's but with fixed draft H , H_3/H ,

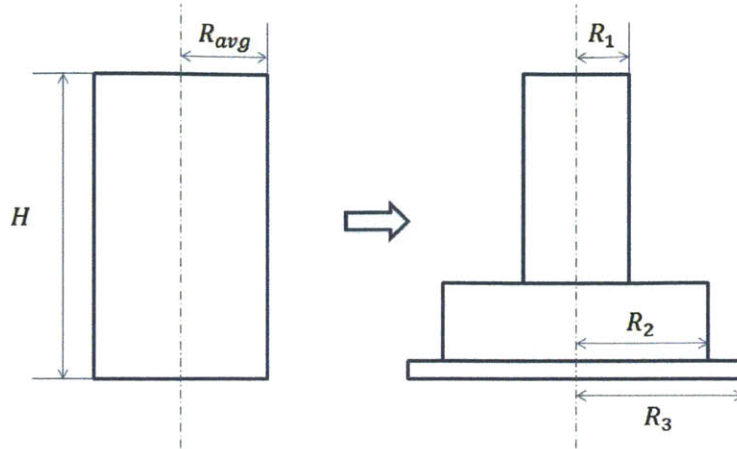


Figure 4-3: Sketch of the result of phase I of the hull evolution from a circular cylinder. We shrink the water-plane area, enlarge the keel radius and attach a heave plate at the keel to achieve soft stiffness and large added mass in heave motion.

R_1/R_{avg} and R_2/R_{avg} (see Figure 4-5).

From Figure 4-6 we can conclude that:

- (1) An oblique shoulder is equivalent to a horizontal shoulder in terms of the cancellation of the heave exciting force;
- (2) The hydrostatic stability can be achieved with less difficulties for a design with an inclined shoulder than that with an even shoulder.
- (3) Oblique shoulders avoid the rapid variation of the cross section.

In terms of the wave exciting force, we arrive at a design with two cylinders connected by an inclined shoulder at phase II of the evolution of the hull shape (see Figure 4-5).

4.1.4 Increase the viscous damping

The presence of the heave plate can also increase the viscous damping via shedding vortices at its edge, thus further reduce the heave motion of the platform. This effect is captured by DVRM (see Chapter 3, section 3.2).

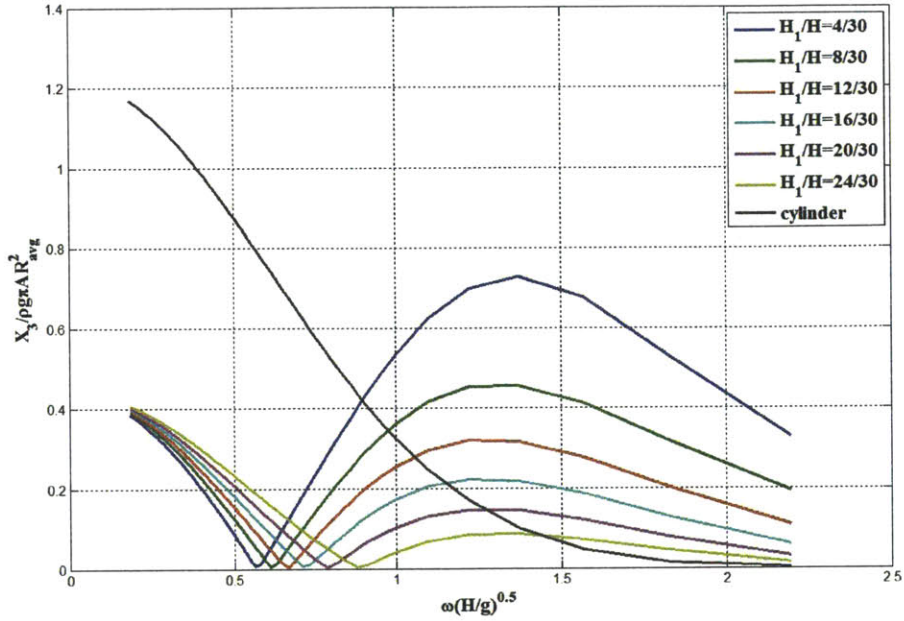


Figure 4-4: The heave exciting force coefficients for different H_1/H from WAMIT. The black curve is the result for a circular cylinder with $H = 30\text{ m}$ and $R_{avg} = 11.3\text{ m}$. The zero force coefficients at low frequencies for the designs with a shoulder justify the cancellation effect of the exciting force due to this shoulder.

In summary, the basic shape of our platform is shown in Figure 4-7.

4.2 An example of the mini-platforms compared with the spar in heave

We obtain the basic geometric shape of the hull on the basis of a spar with fixed displacement and draft. In this section, we will compare the heave motion performance of our platform with the spar quantitatively. The mini-platform and the spar have the same displacement of 12,000 ton and the same draft of 30 m. For simplicity, A is used to denote the spar while B is used to represent our miniature platform in the following description.

The dimensions of these two platforms are summarized in Table 4.1.

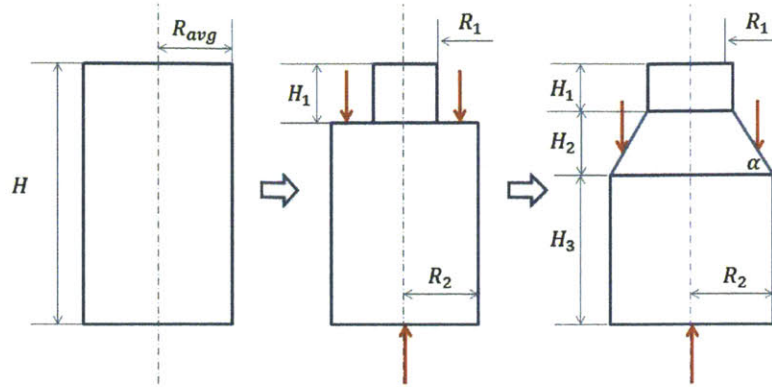


Figure 4-5: Sketch of the result of phase II of the hull evolution from a circular cylinder, to two cylinders with a high even shoulder, and to two cylinders connected by an oblique shoulder. Such a design utilizes the cancelling effect of the heave exciting force, and avoids an abrupt fluctuation in the cross section.

#	R_1/m	R_2/m	R_0/m	R_3/m	H/m
A	11.3	11.3	0	11.3	30
B	8	12.1	5	17.1	30
#	H_1/m	H_2/m	H_3/m	t/m	Δ/t
A	0	0	0	0	12,034
B	2	7	21	0.5	12,773

Table 4.1: Dimensions of the spar A and newly designed mini-platform B.

4.2.1 Comparison in the RAO's

We calculate the RAO's (with and without viscous effects) for both platforms according to equation (3.83) and (3.107). As for the determination of C_D , we let Ξ_{20} be 0.5 m, and then obtain $KC = 0.6$ from equation (3.81). Therefore, $C_D = 8.5$ from our DVRM code. The comparison of RAO's is shown in Figure 4-9.

Figure 4-9 shows that the resonance frequency for spar A falls into the range near 14s which is close to T_p for GoM (see Chapter 3, section 3.5.1), but our new design has a natural period greater than 20s. Also, the response for our design A at the resonance frequency with viscous effect included is reduced significantly compared to that without viscous effect.

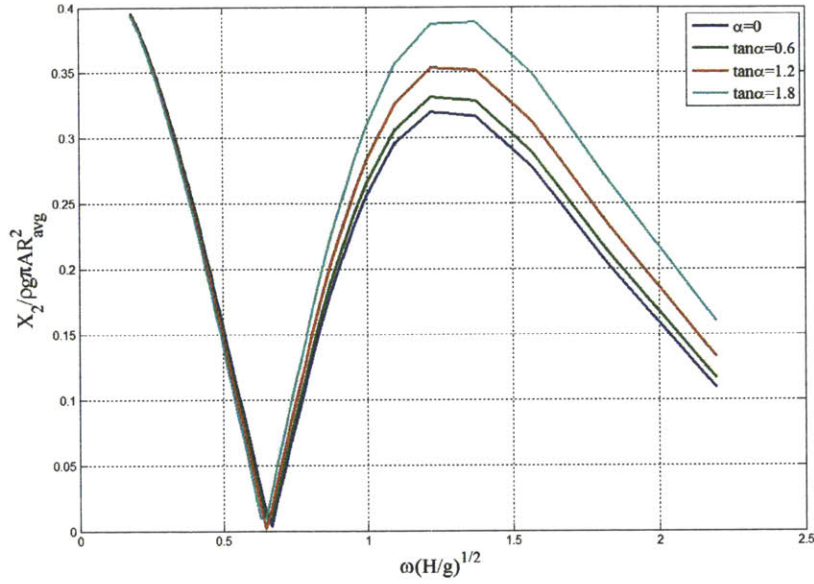


Figure 4-6: Variation of the heave exciting force coefficient for a floating body of two cylinders connected by a shoulder with different inclination α 's. The draft of the body H and the length of the lower cylinder H_3/H are fixed. The calculation results are from WAMIT.

4.2.2 Comparison in the response in various sea-states

We consider the two sea-states for design. One is the operation condition for 1-year term, and the other is the survival condition for 100-year term. For Gulf of Mexico, H_s and T_p characterizing these two design conditions usually are given in Table 4.2 (ITTC). We use the modified Pierson-Moskowitz (PM) spectrum for calculation (see equation (3.119)).

	Operation Condition	Survival Condition
H_s/m	4.0	12.0
T_p/s	10.0	14.0

Table 4.2: The characteristic parameters of the design condition of the sea-states. H_s is the significant wave height. T_p is the peak period of the wave spectrum. The data is retrieved from ITTC.

The modified PM wave spectrum for these two design conditions are shown in Figure 4-10. The heave motion responses of the spar A and the mini-platform B

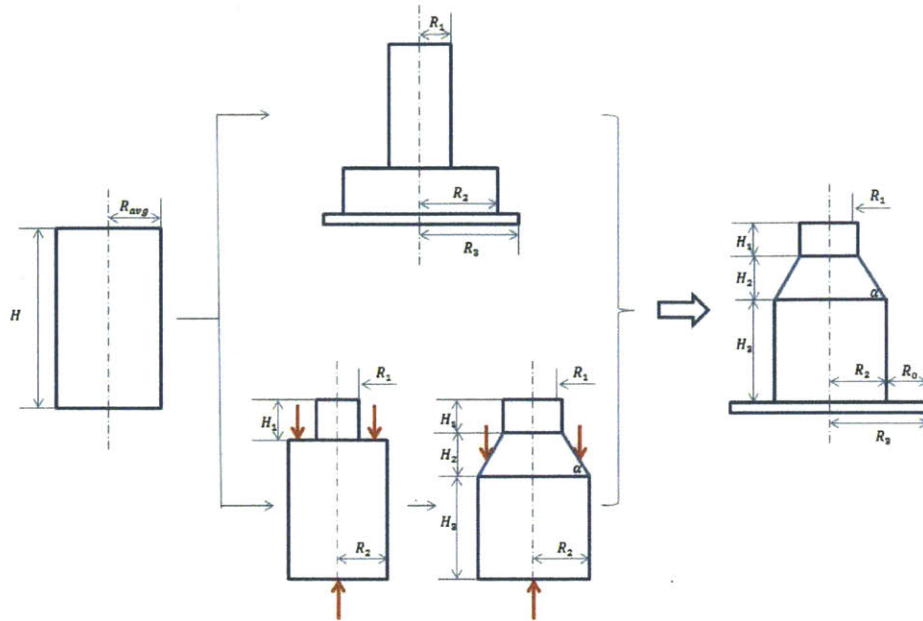


Figure 4-7: Summary of all the phases of the hull evolution from a circular cylinder to the final configuration of the mini-platform

under these two sea-states are shown in Table 4.3.

#	GM/m	T_n /s	1-year	100-year
			ξ_s /m	ξ_s /m
A	1.8354	12	4.6308	11.5016
B (w/o Damping)	1.0631	21.5	0.4122	2.5088
B (w/ Damping)	1.0631	21.5	0.4115	1.0298

Table 4.3: Comparison of the significant heave motion height ξ_s in various sea-states for spar A and mini-platform B, where GM denotes the hydrostatic metacentric height, and T_n is the natural periods in heave. The result is obtained from the combination of WAMIT and DVRM.

As can be seen in Table 4.3, our newly designed mini-platform not only satisfies the basic hydrostatic requirement (see equation (2.4)), but also has a satisfactory motion performance compared to the spar. The natural period is 21.5s, which is much larger than the peak periods of the wave spectra under operation and survival conditions. The significant motion height ξ_s in the two design conditions are significantly reduced

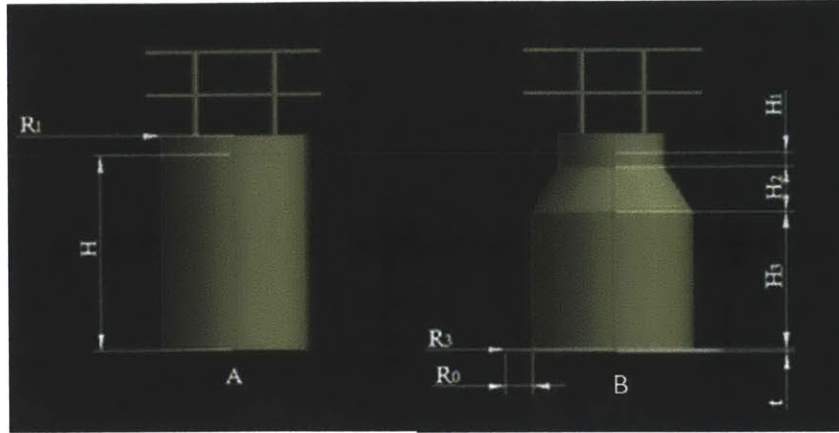


Figure 4-8: Sketch of the miniature platform and the spar with the same displacement $\Delta = 13,000 \text{ ton}$ and the same draft $H = 30 \text{ m}$.

in comparison with that of the spar with the same displacement.

4.3 Effect of the geometric parameters of the mini-platform on heave

The example provided in the last section is the conceptual design. In this section, emphasis will be placed on the effect of the ratios of different dimensions on the heave motion. This parameter analysis provides a guidance for the optimization of the hull in the next chapter.

In the following analysis, we use the (dimensionless) significant heave motion height ξ_s/H_s to quantify the heave response. The dimensions of the newly-designed mini-platform can be referred in Figure 4-7.

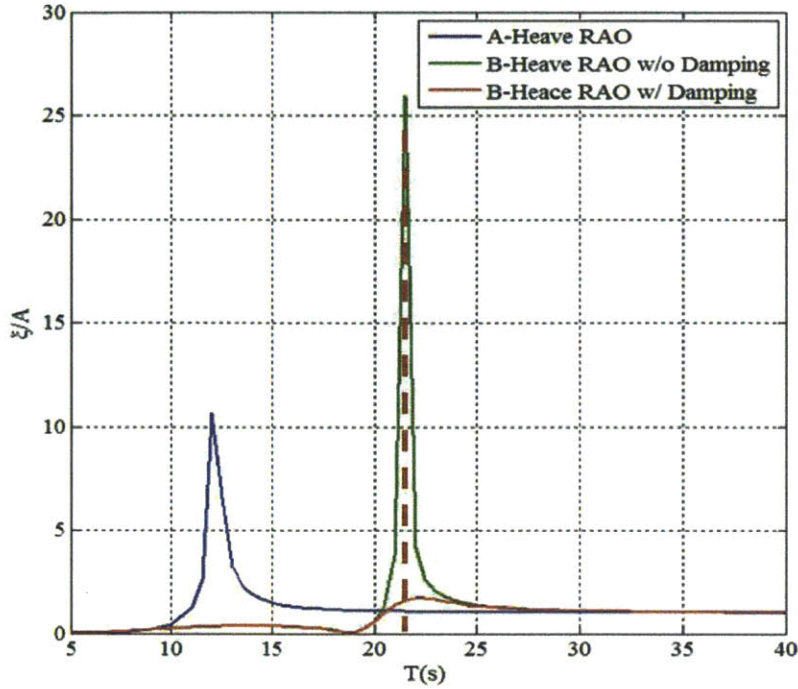


Figure 4-9: Comparison of the heave RAO of our mini-platform B and the spar A. The blue curve is the RAO without viscous damping for A. The green curve is the RAO without viscous damping for B. Both of these two curves are obtained from WAMIT. The red curve is the modified RAO with viscous damping defined in equation (3.107) based on the combination of WAMIT and DVRM. The red curve has a much smaller peak value compared with the other two curves.

4.3.1 Effect of the draft on heave

Let us first study the influence of the total draft H on the heave motion. Here we fix all the other geometric parameters.

$$H_1/H_2 = 1 \tag{4.3}$$

$$H_2/H_3 = 1 \tag{4.4}$$

$$R_2/R_1 = 1.5 \tag{4.5}$$

$$R_3/R_2 = 1.3 \tag{4.6}$$

The results of the heave performance versus the total draft are shown in Figure 4-

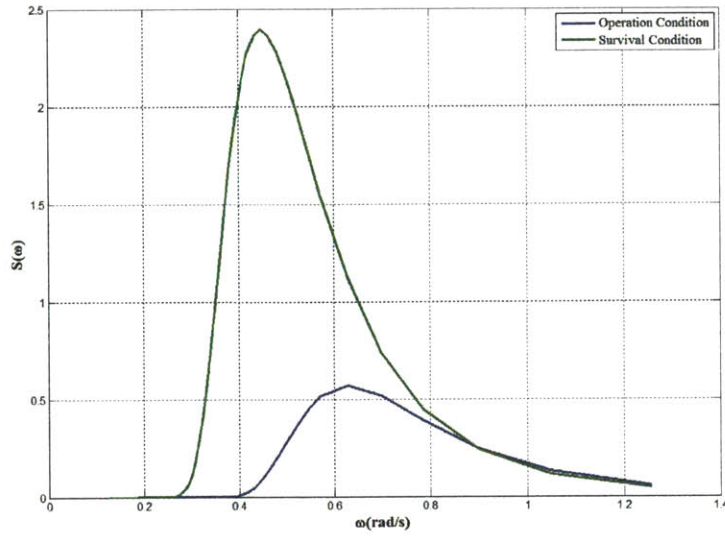


Figure 4-10: Modified Pierson-Moskowitz spectrum used for design. The blue curve is for the operation condition with $H_s = 4.0$ m and $T_p = 10.0$ s. The green curve is for the survival condition with $H_s = 12.0$ m and $T_p = 14.0$ s

11. Figure 4-12 shows the stiffness, added mass coefficients and resonance frequencies while Figure 4-13 gives the wave exciting force coefficients at the resonant frequency as a function of draft H. We can see that deeper draft corresponds to a smaller heave motion amplitude. This can be explained from Figure 4-12 and 4-13. One reason is that the wave effects decay exponentially with increasing submergence, resulting in smaller wave exciting force, as can be seen from Figure 4-13. This is exactly the principle behind the concept of deep draft floaters like spars. The other reason is that deeper draft with a fixed displacement leads to smaller water-plane area, thereby providing softer stiffness. This shifts the heave natural frequency further lower from the frequency range of high wave energy, as shown in Figure 4-12. Note that the resonance frequency does not decay as fast as the stiffness because the added mass is sacrificed while the draft increases.

In addition, deep draft is beneficial for lowering the gravity centre, ensuring the hydrostatic stability. However, increasing the draft of the system makes construction and installation more costly. Sometimes, transit routes may also limit the choice in draft. Therefore, we need to make proper tradeoffs between the choice of draft and

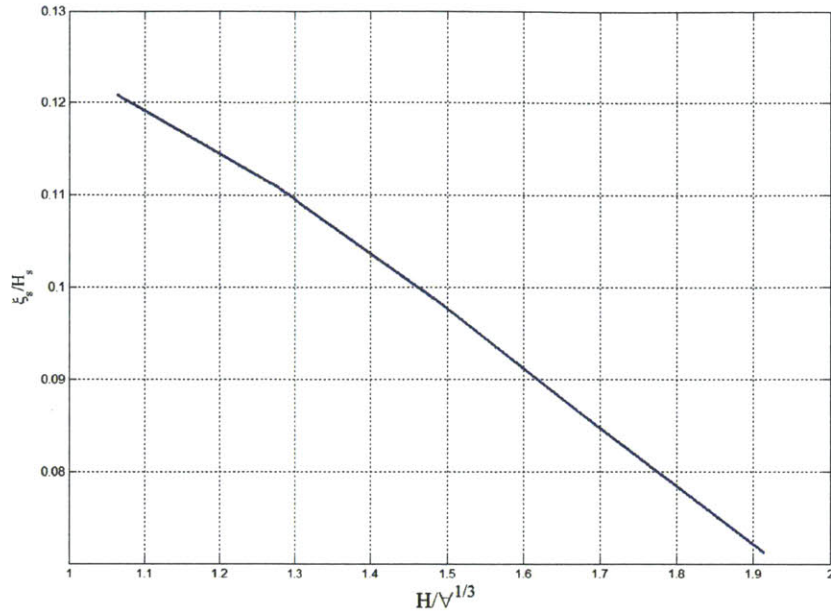


Figure 4-11: Variation of heave motion amplitude ξ_s/H_s for the mini-platform as a function of the total draft $H/\nabla^{1/3}$, where $\nabla = 13,000 \text{ m}^3$, $H_1/H_2 = H_2/H_3 = 1$, $R_2/R_1 = 1.5$ and $R_3/R_2 = 1.3$. The results are from equation (3.122) based on WAMIT and DVRM.

requirement of small heave response. For the optimization in Chapter 5, we will use these two parameters $H/\sqrt[3]{\nabla}$ and ξ_s/H_s as our objectives.

4.3.2 Effect of the axial distribution of the displacement on heave

This subsection will concentrate on investigating how the axial distribution of the displacement affects the heave motion. Variable controlling approach is applied again. The heights of the three sections of the platform can form two independent dimensionless parameters H_1/H and H_3/H which vary between $0 \sim 1$. All the other parameters are fixed at some moderate values to exclude extremely odd shapes.

$$\nabla = 13000 \text{ m}^3 \quad (4.7)$$

$$H/\sqrt[3]{\nabla} = 1.5 \quad (4.8)$$

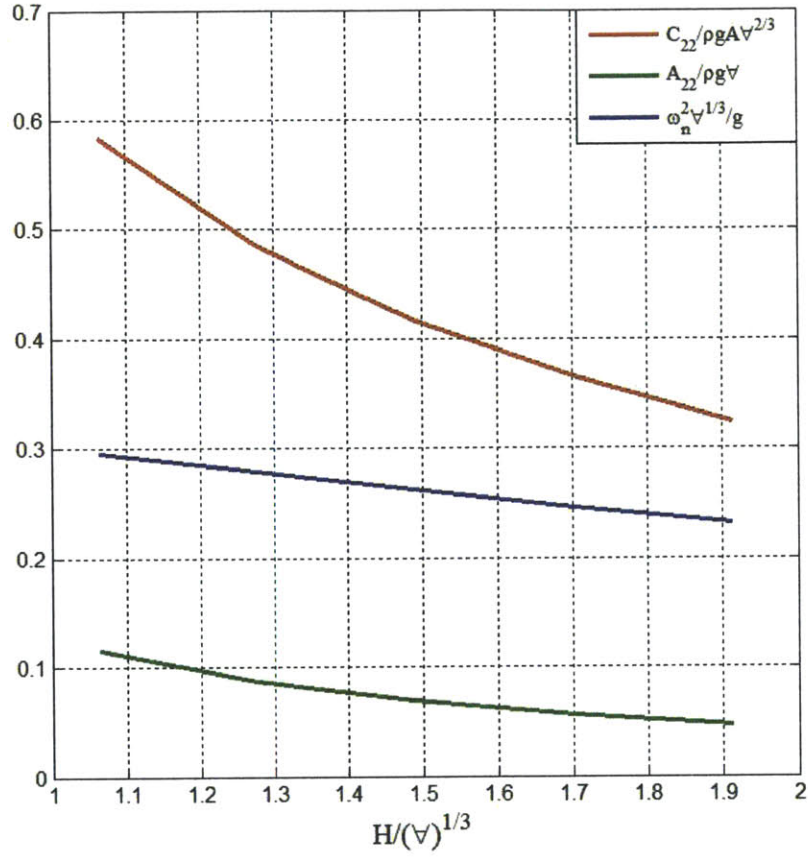


Figure 4-12: Variation of the stiffness, added mass coefficients and resonant frequencies for the mini-platform as a function of the total draft $H/\nabla^{1/3}$, where $\nabla = 13,000 \text{ m}^3$, $H_1/H_2 = H_2/H_3 = 1$, $R_2/R_1 = 1.5$ and $R_3/R_2 = 1.3$. The results are from WAMIT.

$$R_2/R_1 = 1.5 \quad (4.9)$$

$$R_3/R_2 = 1.5 \quad (4.10)$$

Figure 4-14 shows the contours of the significant heave motion amplitude ξ_s/H_s while H_1/H and H_3/H vary. As can be seen, there are two regions where ξ_s/H_s achieves the minimal values. One is the region where H_1/H is around 0.2, and H_3/H is around 0.7. This corresponds to a design of a high shoulder. The other region is on the opposite. With H_1/H about 0.5 ~ 0.6 and H_3/H about 0.1 ~ 0.3, this region provides another type of design with a low shoulder.

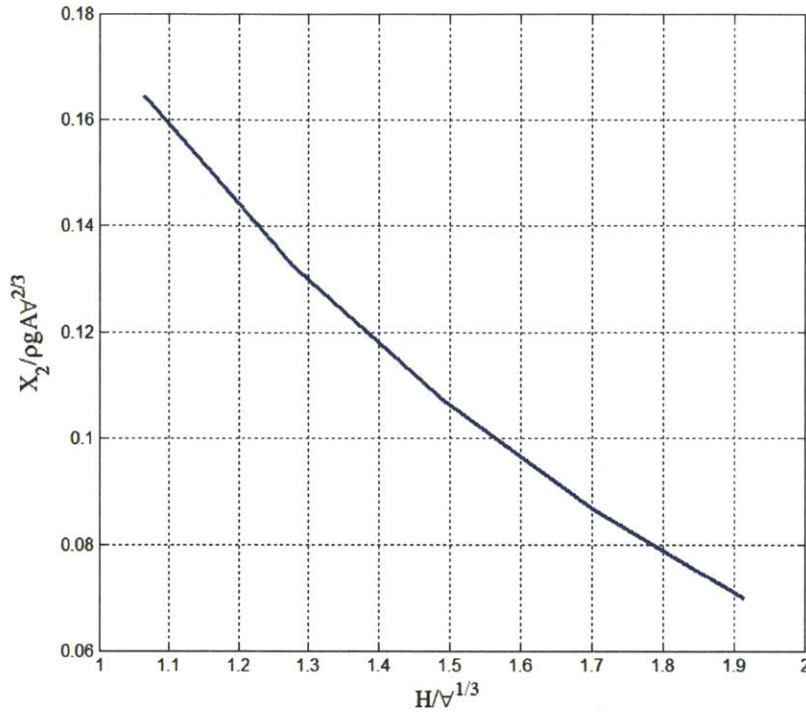


Figure 4-13: Variation of the wave exciting force coefficient for the mini-platform as a function of the total draft $H/\nabla^{1/3}$, where $\nabla = 13,000 \text{ m}^3$, $H_1/H_2 = H_2/H_3 = 1$, $R_2/R_1 = 1.5$ and $R_3/R_2 = 1.3$. The results are from WAMIT.

The results in Figure 4-15, 4-16 and 4-17 can help explain the features of the results in Figure 4-14. Let us discuss these two regions respectively.

Region I obtains a satisfactory motion response for the following reasons. Firstly, Since the draft of the mini-platform is only around 30 meters, much shallower compared to the spars (around 200 meters in draft normally), a significant vertical wave exciting force is exerted at the keel, especially in long waves. A high shoulder can counteract a fairly large portion of this exciting force in the long-wave frequencies (see section 4.1.3). As shown in Figure 4-17, the heave exciting force coefficient $X_2/\rho g \nabla^{2/3}$ decreases as the position of the shoulder rises. Secondly, a high shoulder moves much of the displacement downwards, so the stiffness $C_{22}/\rho g \nabla^{2/3}$ and hence the natural frequency of the heave motion are reduced, as can be seen in Figure 4-16. However, the raise of the shoulder is limited by two constraints in practice. On one hand, the

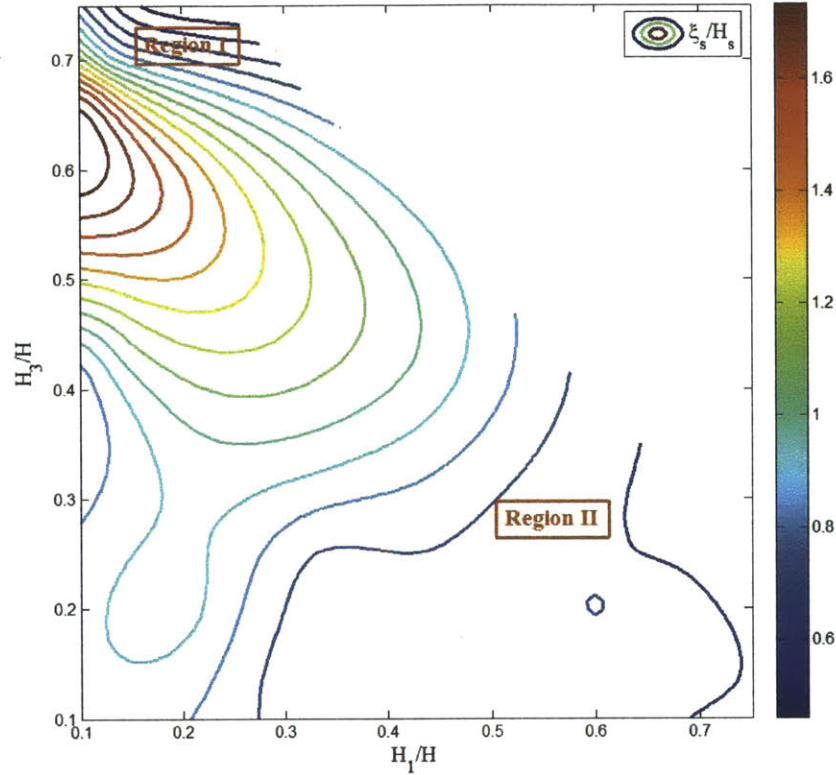


Figure 4-14: Contours of the dimensionless heave motion amplitude ξ_s/H_s for the mini-platform as a function of H_1/H and H_3/H , while $\nabla = 13000 \text{ m}^3$, $H/\sqrt[3]{\nabla} = 1.5$, $R_2/R_1 = 1.5$ and $R_3/R_2 = 1.5$. The results are from equation (3.122) based on WAMIT and DVRM.

water-plane radius R_1 should be larger than 7 m due to the presence of the moonpool (see Chapter 2, section 2.3). On the other hand, we should prevent the shoulder from penetrating the water surface during the motion (see section 4.1.3).

As for Region II, a lower shoulder may not reduce the heave exciting force and stiffness, but can result in a large heave added mass. Based on Figure 4-15, the added mass $A_{22}/\rho\nabla$ reaches the maximum when the shoulder is lowest. In addition, contrary to Region I, we do not need to concern about the shoulder penetrating the water surface. However, we need to ensure that the hydrostatic stability is satisfied while lowering the shoulder.

To sum up, based on the analysis of the above two regions, we see that the axial

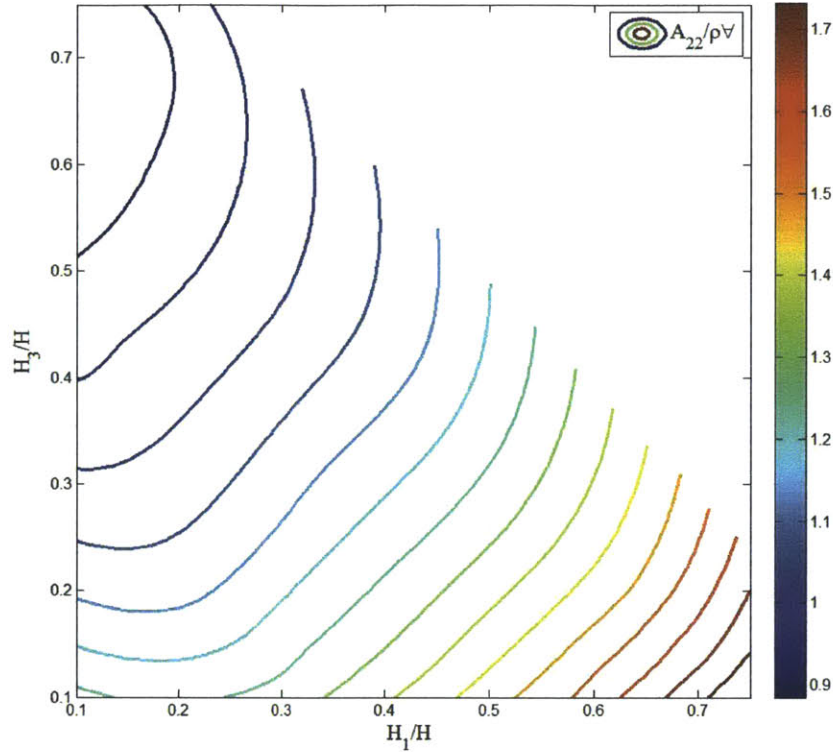


Figure 4-15: Contours of the heave added mass coefficients as a function of H_1/H and H_3/H , while $\mathcal{V} = 13000 \text{ m}^3$, $H/\sqrt[3]{\mathcal{V}} = 1.5$, $R_2/R_1 = 1.5$ and $R_3/R_2 = 1.5$. The data is obtained from WAMIT.

distribution of the hull determines the competition between the wave exciting force and added mass. In addition, attention should always be paid on different constraints. We could expect that the optimal design should fall into either of these two regions.

4.3.3 Effect of the radial distribution of the displacement on heave

We have narrowed down the optimal solution space in terms of the axial distribution, now let us investigate the effect of radial distribution on heave motion. The three radii for the three sections and the heaving plate form two independent non-dimensional parameters R_2/R_1 and R_3/R_2 . The basic geometric shape for our platform is narrow in top and wide at keel. Hence here we vary these two parameters from 1 to 2.

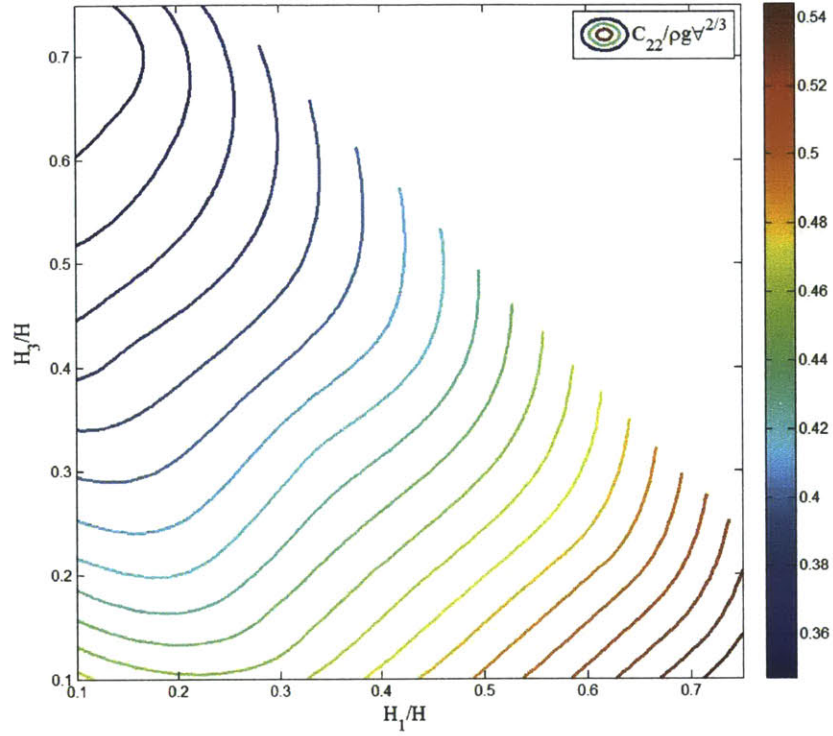


Figure 4-16: Contours of the dimensionless stiffness as a function of H_1/H and H_3/H , where $\nabla = 13000 \text{ m}^3$, $H/\sqrt[3]{\nabla} = 1.5$, $R_2/R_1 = 1.5$ and $R_3/R_2 = 1.5$. The results are from WAMIT.

Let us take Region II as an example. All the other parameters are fixed as follows.

$$\nabla = 13000 \text{ m}^3 \quad (4.11)$$

$$H/\sqrt[3]{\nabla} = 1.5 \quad (4.12)$$

$$H_1/H = 0.55 \quad (4.13)$$

$$H_3/H = 0.3 \quad (4.14)$$

As can be seen from Figure 4-18, for smaller values of the two radius ratios, the heave motion response decreases as both R_2/R_1 and R_3/R_2 increase. This is because large radius ratios shrink the water-plane area and enlarge the keel radius, resulting in a larger added mass (see Figure 4-19), more viscous damping (see Figure 4-20)

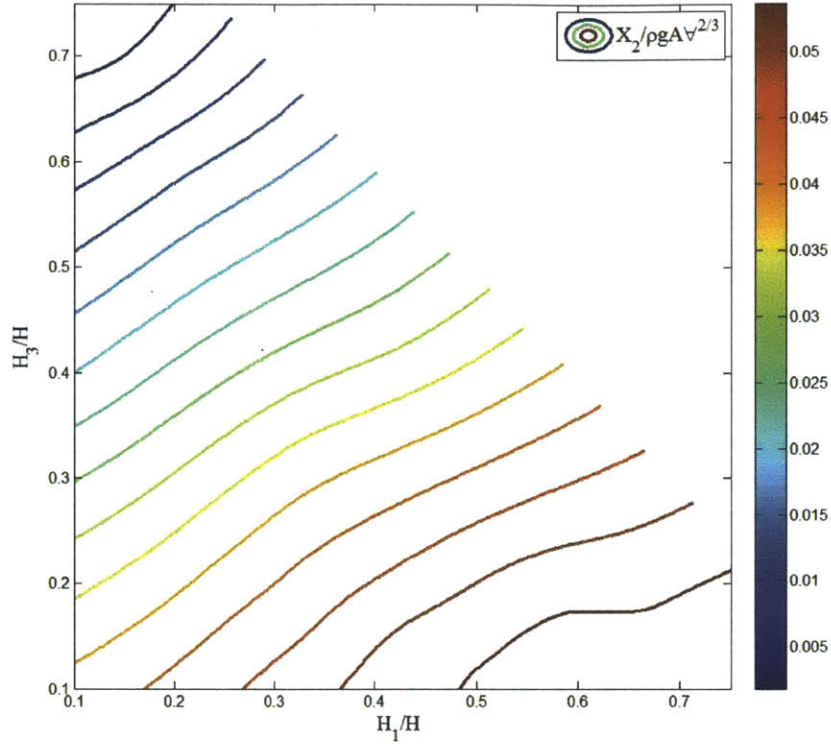


Figure 4-17: Contours of the wave exciting force coefficients as a function of H_1/H and H_3/H , while $\forall = 13000 \text{ m}^3$, $H/\sqrt[3]{\forall} = 1.5$, $R_2/R_1 = 1.5$ and $R_3/R_2 = 1.5$. The results are from WAMIT.

and softer stiffness (see Figure 4-21). Consequently, the resonance frequencies can be shifted into lower ranges for larger radius ratios (see Figure 4-22). However, we can also see from Figure 4-18 that for radius ratios greater than 1.5, increasing these two ratios may not mitigate the motion response further. This can be explained in terms of the wave exciting force. As can be seen from Figure 4-23, the wave exciting force coefficient generally has a small value for smaller radius ratios, and reaches the minimum value when R_2/R_1 and R_3/R_2 are around 1.5. Beyond this value, the wave exciting force increases significantly as the radius ratios increase, counteracting the contribution due to the larger added mass, more viscous damping and softer stiffness on suppressing the motion.

In addition, we should keep in mind that these radius ratios are limited by the following constraints. The first is that the water-plane area is restricted because of

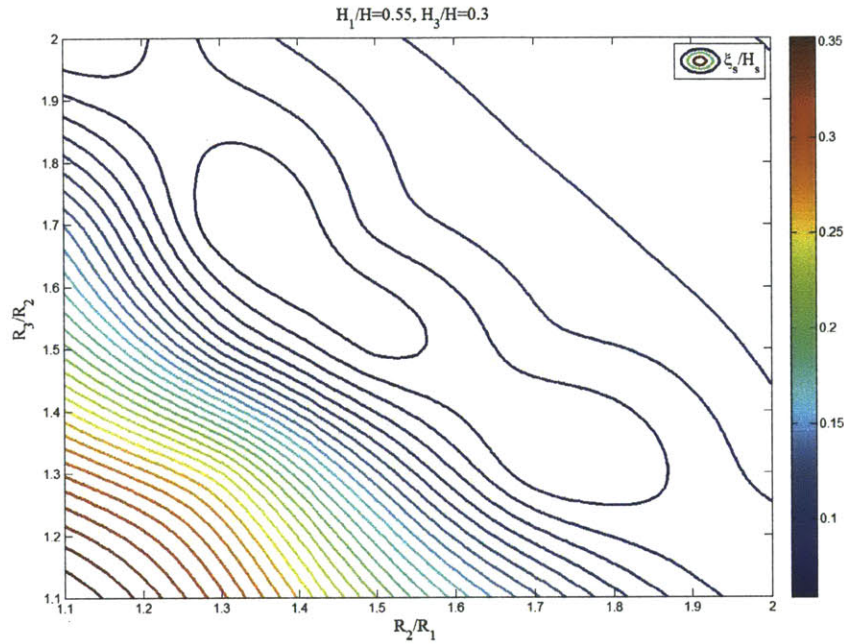


Figure 4-18: Contours of the dimensionless heave motion amplitude ξ_s/H_s for the mini-platform as a function of R_2/R_1 and R_3/R_2 , while $\nabla = 13000 \text{ m}^3$, $H/\sqrt[3]{\nabla} = 1.5$, $H_1/H = 0.55$ and $H_3/H = 0.3$. The results are from equation (3.122) based on WAMIT and DVRM.

the moonpool, as mentioned earlier. The next is that the centre of buoyancy should not be too low in order to guarantee the hydrostatic stability. Finally, a large heave plate may bring inconvenience to installation and transportation. Therefore, for the optimization in the next chapter, we need to examine these constraints.

Based on the above analysis, we expect that the final optimal design should have the radius ratios around 1.5.

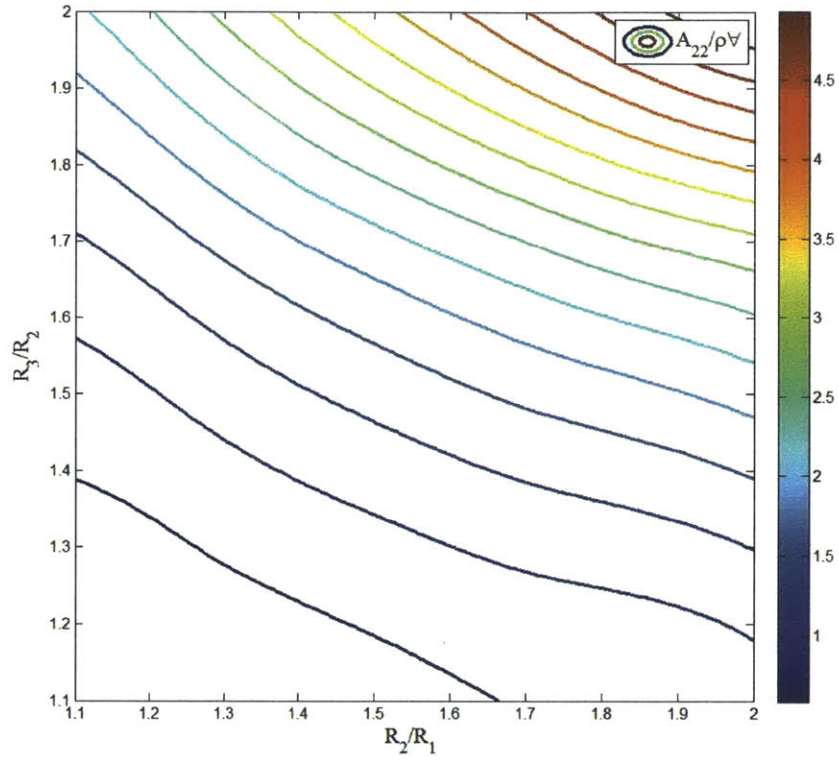


Figure 4-19: Contours of the added mass coefficient for the mini-platform as a function of R_2/R_1 and R_3/R_2 , while $\forall = 13000 \text{ m}^3$, $H/\sqrt[3]{\forall} = 1.5$, $H_1/H = 0.55$ and $H_3/H = 0.3$. The results are from WAMIT.

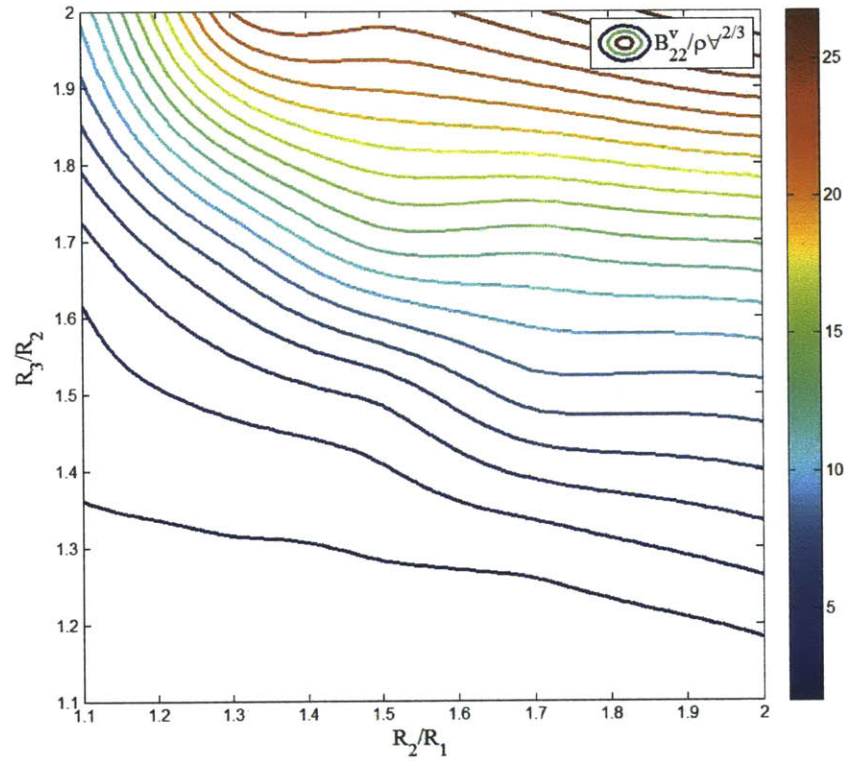


Figure 4-20: Contours of the viscous damping coefficients for the mini-platform as a function of R_2/R_1 and R_3/R_2 , while $\nabla = 13000 \text{ m}^3$, $H/\sqrt[3]{\nabla} = 1.5$, $H_1/H = 0.55$ and $H_3/H = 0.3$. The results are from DVRM.

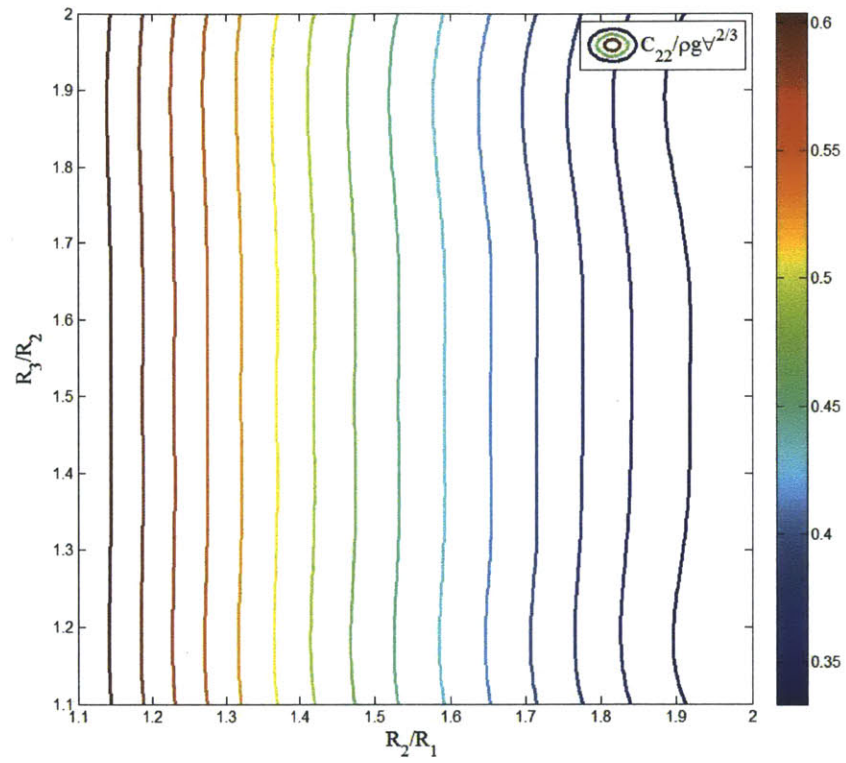


Figure 4-21: Contours of the dimensionless softness for the mini-platform as a function of R_2/R_1 and R_3/R_2 , while $\nabla = 13000 \text{ m}^3$, $H/\sqrt[3]{\nabla} = 1.5$, $H_1/H = 0.55$ and $H_3/H = 0.3$. The results are from WAMIT.

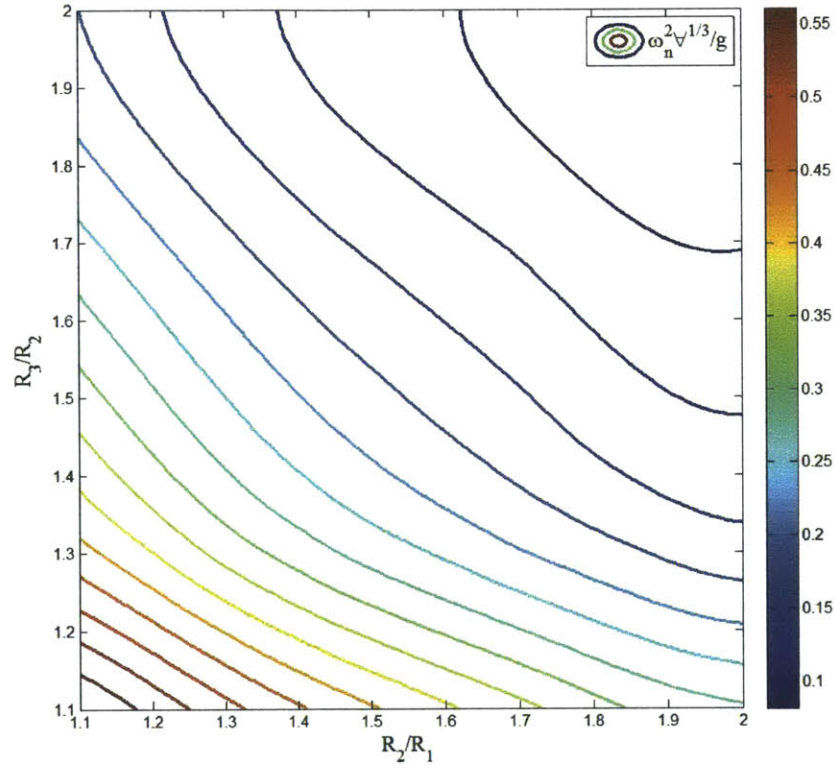


Figure 4-22: Contours of the dimensionless resonance frequencies in heave for the mini-platform as a function of R_2/R_1 and R_3/R_2 , while $\nabla = 13000 \text{ m}^3$, $H/\sqrt[3]{\nabla} = 1.5$, $H_1/H = 0.55$ and $H_3/H = 0.3$. The results are from WAMIT.

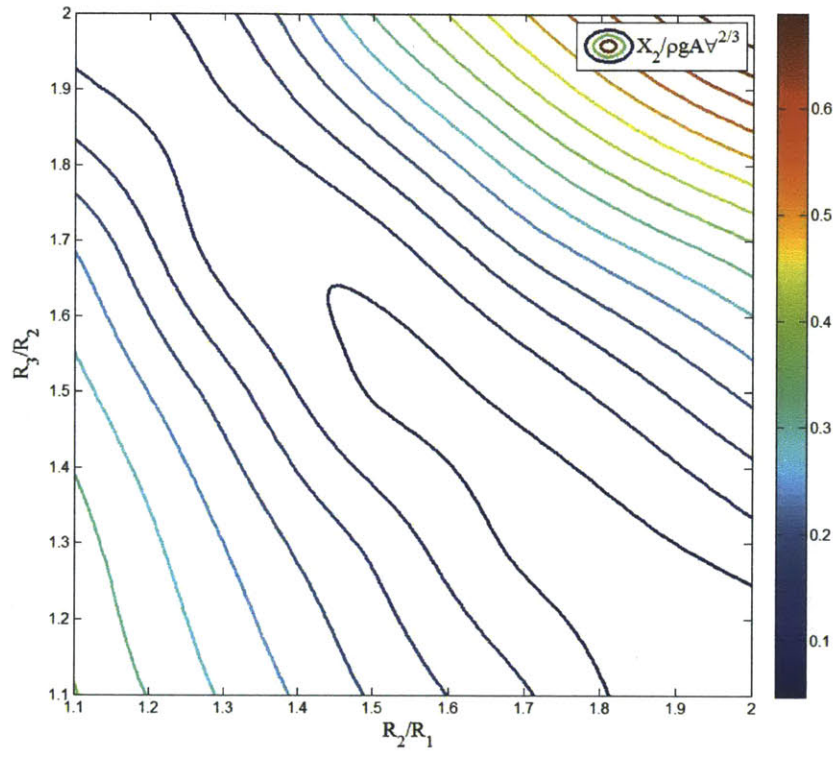


Figure 4-23: Contours of the wave exciting force coefficients for the mini-platform as a function of R_2/R_1 and R_3/R_2 , while $V = 13000 \text{ m}^3$, $H/\sqrt[3]{V} = 1.5$, $H_1/H = 0.55$ and $H_3/H = 0.3$. The results are from WAMIT.

Chapter 5

Hull Optimization for the Mini-platform

In this chapter, we will apply a genetic algorithm to seek for the optimal design of the miniature platform based on the analysis in the previous chapter. The effective application of optimization requires a completely automated evaluation of appropriate design criteria and their mathematical representations (objective functions). For the platform shape optimization, the following items must be provided (Birk, 2007):

- Flexible shape definition by forming parameters and an automated shape generation
- Hydrodynamic analysis of arbitrary hull geometry
- Definition of suitable objective functions

Therefore, design variables have to be chosen from the available form parameters. In addition, both objective functions and constraints must be formulated to guarantee that the resulting design is feasible with respect to all requirements imposed on the design.

Figure 5-1 illustrates the general optimization procedure used in this thesis. A subset of parameters describing the hull shape constitutes the vector of free variables \mathbf{x} . Some other parameters \mathbf{p} remain fixed for all the designs. The optimization loop starts when the initial data is provided. Constraints examination, hydrodynamic

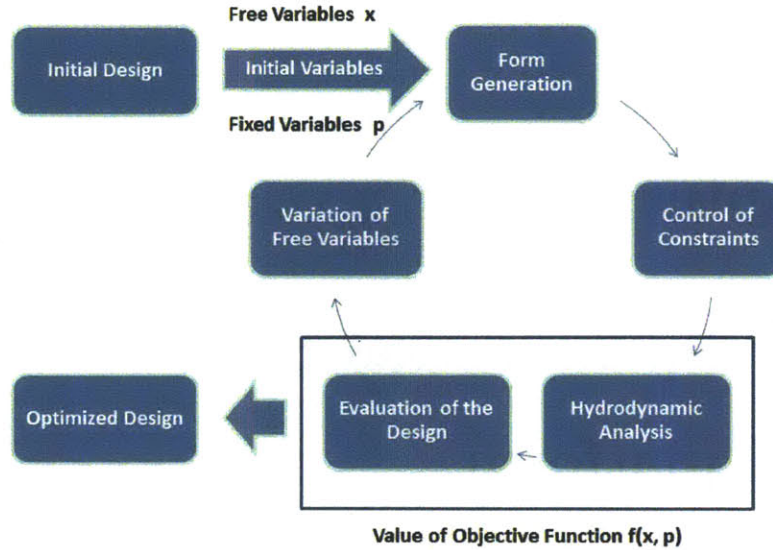


Figure 5-1: Framework of the parametric optimization of hull shape

analysis and the assessment of the designs are repeated with adjusting free variables until the minimum of the objective functions are achieved. Such control of the process is conducted by an optimization algorithm, and is completely automatic with no user interference. In the following sections, we will present this process in details.

5.1 Optimization parameters for automatic generation of the hull shape

Due to the automation of the optimization, we need to first define the parameters to create the hull shape. Our mini-platform is set up with two cylindrical parts which are connected by an intermediate part of variable length (see Figure 5-2). As a design premise, we fix the displacement of the platform to be $V = 13,000 \text{ m}^3$ (see Chapter 2, section 2.2.3) and the thickness of the heaving plate to be $th = 0.5 \text{ m}$ (see Chapter 2, section 2.3.5), i.e., $\mathbf{p} = (V, th)$. Therefore, five independent dimensionless parameters determine the shape of the hull entirely. They serve as the free variables

\mathbf{x} for the optimization. Their upper and lower limits are defined in table 5.1, which are consistent with the parameter analysis in Chapter 4 (see Chapter 4, section 4.3) . These limits are selected to provide a rather flexible space for designs but also avoid extremely odd shapes.

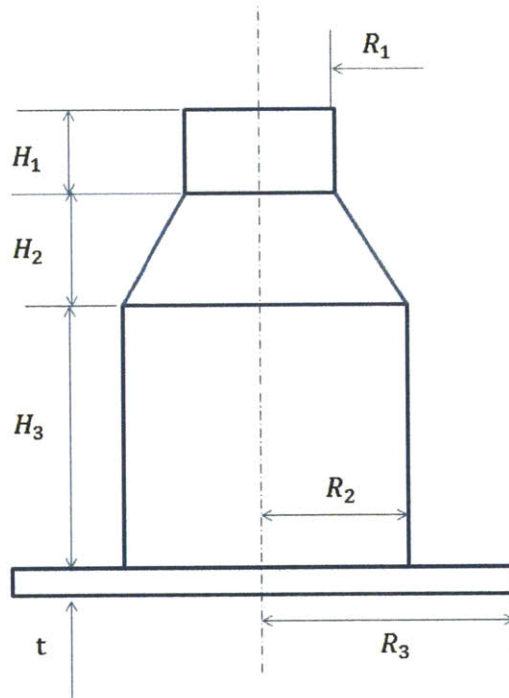


Figure 5-2: Setup of the mini-platform for the hull optimization.

Clearly the total draft is the sum of all the part heights.

$$H = \sum_{i=1}^{i=3} H_i \quad (5.1)$$

Substituting recursively the relation $H_i = H_{i,i+1} \cdot H_{i+1}$ yields an equation which can be solved for the unknown H_3 .

$$H_3 = \frac{H}{H_{12}H_{23} + H_{23} + 1} \quad (5.2)$$

No.	Definition	Symbols	Range
x_1	$H/\sqrt[3]{\forall}$	H^*	1.06 ~ 1.91
x_2	H_1/H_2	H_{12}	1/5 ~ 5
x_3	H_2/H_3	H_{23}	1/5 ~ 5
x_4	R_2/R_1	R_{21}	1 ~ 2
x_5	R_3/R_2	R_{32}	1.1 ~ 1.5

Table 5.1: Upper and lower limits of the five free optimization variables to describe the hull shape

Therefore,

$$H_1 = H_3 \cdot H_{12} \cdot H_{23} \quad (5.3)$$

$$H_2 = H_3 \cdot H_{23} \quad (5.4)$$

Calculation of the cross section radius follows a similar approach to the length calculation. The total displaced volume is the sum of two circular cylinders and a truncated cone. Here we ignore the volume of the heave plate.

$$\forall = \pi R_1^2 H_1 + \pi R_2^2 H_3 + \frac{\pi}{3} (R_1^2 + R_2^2 + R_1 R_2) \quad (5.5)$$

Utilizing the radius ratios R_{21} we substitute the radius $R_2 = R_1 \cdot R_{21}$ into equation (5.5) so that only R_1 is left. Then R_1 can be computed from:

$$R_1 = \sqrt{\frac{\forall}{\pi \{ H_1 + R_{21}^2 H_3 + \frac{1}{2} (1 + R_{21}^2) H_2 \}}} \quad (5.6)$$

Therefore,

$$R_2 = R_1 \cdot R_{21} \quad (5.7)$$

$$R_3 = R_1 \cdot R_{32} \cdot R_{21} \quad (5.8)$$

Thus the geometric shape of the hull can be generated with the free variables vector $\vec{x} = [x_1, x_2, x_3, x_4, x_5]$ and the fixed parameters vector $\vec{p} = [\forall, t]$.

5.2 Constraints for the mini-platform designs

As discussed in Chapter 1, the following constraints must be examined for each design.

1. Constraint for heave natural period

$$T_n \geq 19s \quad (5.9)$$

A heave resonance period of just 19 seconds would be considered low for both of the target operation areas (see Chapter 4, section 4.2.2). Since minimizing the motion amplitude is consistent with maximizing the resonance period, 19 seconds could be a compromise between eliminating unwanted designs and unnecessarily narrowing down the solution space.

2. Constraint for metacentric height

Metacentric height should satisfy the following condition based on the analysis in Chapter 2 (see Chapter 2, section 2.4):

$$GM = z_B - z_G + \frac{\frac{1}{4}\pi R_1^4}{\nabla} \geq 1.0m \quad (5.10)$$

3. Constraint for waterplane area

Based on the previous analysis, the water-plane radius should be consistent with the moonpool design (see Chapter 2, section 2.2).

$$R_1 \geq 7.0m \quad (5.11)$$

5.3 Objective functions for the hull shape optimization

The purpose is to find a design with a satisfactory seakeeping characteristic and a “not-too-deep” draft. However, these two goals cannot achieve the minimum at

the same time (see Chapter 4, section 4.3.1). Deeper draft increases the cost of construction and installation, but reduces the wave exciting force, thereby suppressing the heave response. Therefore, draft and heave motion amplitude are selected to be our objective functions. Our target is to find a compromised solution between these two objectives.

Mathematically, the two objective functions $F = [f_1, f_2]$ can be defined as follows:

$$f_1 = H/\sqrt[3]{V} \quad (5.12)$$

As for f_2 , we choose the dimensionless significant heave motion amplitude ξ_s/H_s under the survival sea-state condition (see Chapter 4, section 4.2.2).

$$f_2 = 4\sqrt{\int_0^\infty S(\omega)|RAO(\omega)|^2 d\omega}/H_s \quad (5.13)$$

where $S(\omega)$ is the given wave spectrum for the survival condition defined in Chapter 4 (see Table 4.2). RAO is the modified RAO defined in equation (3.107).

5.4 Optimization algorithm

Since we have two contradictory objectives, this is a multi-objective optimization. Here we use the so-called multi-objective genetic algorithm ($\epsilon - MOGA$) (Laumanns et al., 2002; Deb et al., 2003). Let us first introduce two concepts: Pareto frontier and ϵ -dominance.

5.4.1 Two concepts: Pareto frontier and ϵ -dominance

In this subsection, we follow Laumanns et al.s' paper (2002) and use two-objective optimization as an example to illustrate these two concepts, which is also the case in this thesis.

Multi-objective optimization aims at finding the set of **nondominated** solutions, which are called **Pareto frontier**. For design ① to dominate design ②, ① must

be better than ② in all the objectives, otherwise, they are non-dominated by each other. This is **usual-dominance** concept. As illustrated in Figure 5-4, solution P dominates the region PFCEP, and solution 1 and 2 are nondominated in terms of the above usual-dominance concept. Nondominated designs, or Pareto frontier, can only be improved in one objective by encumbering deterioration in at least one other objective. They themselves are the trade-off solutions we want to find (Laumanns et al., 2002) (see Figure 5-3).

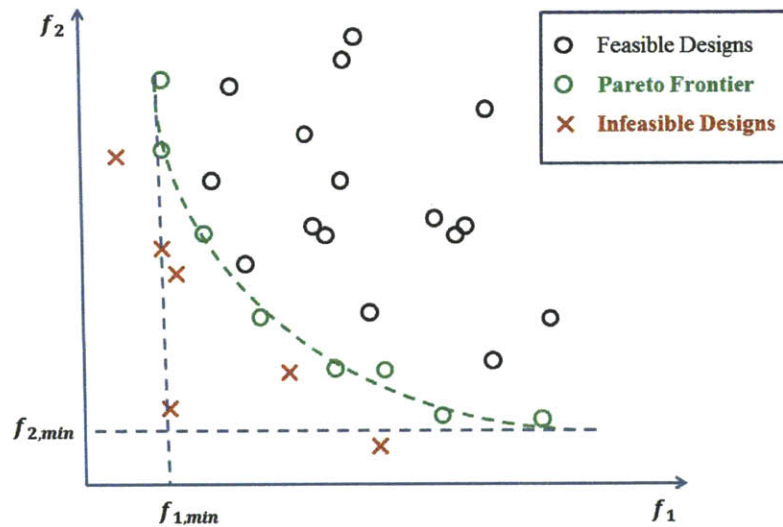


Figure 5-3: Illustration of the Pareto frontier. The black circles represent the feasible designs, the green circles are designs of Pareto frontiers, and the red crosses denote the infeasible designs violating the constraints.

In order to keep the number of designs in the Pareto frontier finite and small, we apply a concept of ϵ -dominance, where ϵ is a small positive number. Let us assign an identification array $\mathbf{B} = (B_1, B_2, \dots, B_M)$ to each solution, where M is the number of the objectives (in our case $M = 2$).

$$B_j(\mathbf{f}) = \text{floor}[(f_j - f_{j,\min})/\epsilon_j], \text{ for minimizing } f_j, j = 1, 2 \quad (5.14)$$

where $f_{j,\min}$ is the minimum possible value of the j -th objective, and ϵ_j is the allowable

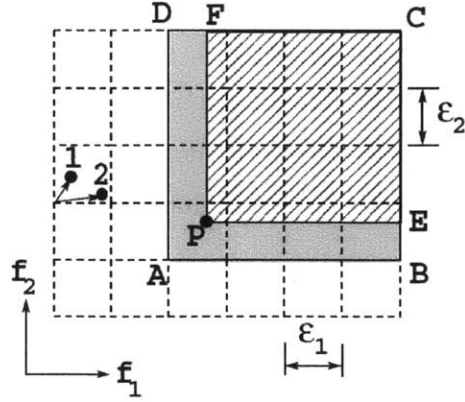


Figure 5-4: Illustration of the concept of usual-dominance and ϵ -dominance (from Deb et al., 2003)

tolerance in the j -th objective below which the values are insignificant to us. The determination of ϵ_j would be presented later.

Now we apply the above **usual-dominance** to the identification array B . If B of design ① dominates that of design ②, then we say design ① **ϵ -dominates** design ②. Otherwise, we call these two solutions ϵ -non-dominated by each other. As illustrated in Figure 5-4, solution P ϵ -dominates the region ABCDA, which is larger than the region PEFCP in the usual-dominance sense.

The value of ϵ can be determined as follows.

$$\epsilon = K' a^{1/m} - 1 \quad (5.15)$$

where a is the maximum size of the Pareto frontier archive; K' is set to be the current maximum relative range of the 2 objectives:

$$K' = \max_{i=1,2} \{u_i - l_i\} \quad (5.16)$$

where u_i and l_i : $u_i \geq l_i > 0$ are the current maximum and minimum values of objective function i .

As we can see, ϵ stands for the tolerance to the values of the objective functions. The bigger the ϵ , the greater the “tolerance”. In addition, ϵ decides the size of the

Pareto frontier archive.

5.4.2 Optimization flow based on ϵ – MOGA

Here we summarize the procedure for the hull shape optimization based on the ϵ – MOGA (Laumanns et al., 2002; Deb et al., 2003; Clauss & Birk, 1996; Birk et al., 2004; Birk, 2007; Birk & Clauss, 2008).

1. Generate the initial population

This algorithm uses a fixed size population and a separate archive of a variable size for the current set of nondominated solutions.

First we can generate enough initial designs, i.e., the population. Each free variable is picked up randomly within its own range. Then we calculate their objective functions and examine the constraints to keep the feasible ones to be the initial designs \vec{p} . Here we use 200 cases to serve as the initial feasible population \vec{p}_0 .

2. Generate the Pareto frontier based on ϵ -dominance concept

Using the ϵ -dominance concept, we extract the set of ϵ -dominated designs to be the initial Pareto frontier archive \vec{f}_0 .

3. Pick up parents for producing the new design

Next we need to select two solutions to be the “parents” to produce a new design “child”. First, we randomly select two parents from the current population \vec{p} for a competition. If one dominates or ϵ -dominates the other, it becomes the winner. If both are not dominated by the other, the winner is selected at random. The winner is the first parent. The second parent is randomly selected from the current Pareto frontier archive \vec{f} .

4. Cross over of the two parents

There are numerous ways to do the mating for the two parents selected in the last step. In this thesis, we use the so-called the “single point cross-over” tech-

nique. Each design is represented by five free variables $\vec{x} = [x_1, x_2, x_3, x_4, x_5]$. Each time, we select a point among the five free variables randomly. Then two children are generated by crossover of the values of these free variables of the selected parents around this point (see Figure 5-5). Here we only choose one of them, i.e., only one child is generated each time.

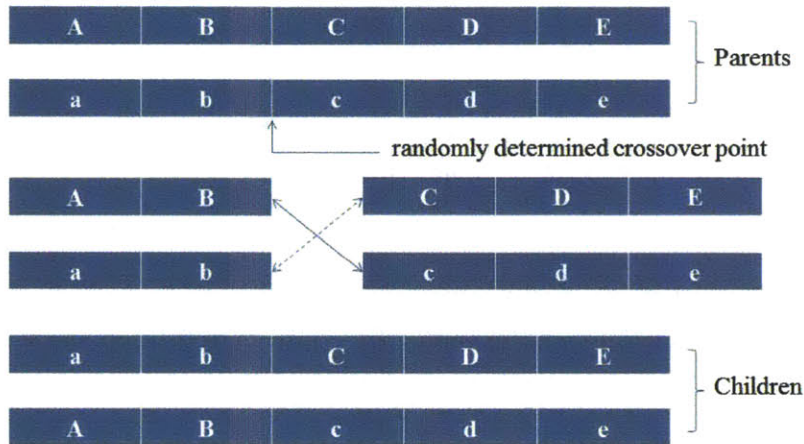


Figure 5-5: Illustration of the single point cross over for two parents to generate two children

5. Mutation of the child

If $random(0, 1) <$ a user defined mutation probability, we will apply a mutation step for the child. Mutation means that one randomly selected free variable is varied in this step, taking a new random value within its range. This mutation aims at introducing new design variations.

6. Update the Pareto frontier archive and population

Once the free variables of the child are defined, we can evaluate their objective functions using WAMIT and DVRM codes and also check the constraints. If this child is not feasible, then go back to step 3 to regenerate the child.

If this child is feasible, then do the following to update the archive. Compare

this child with the current archive member one by one. If the child is dominated or ϵ -dominated by all the archive members, then this child is not accepted. If this child dominates any archive member, this dominated archive member is deleted and the child is accepted. If neither of the above two cases occur, then this means the child is non- ϵ -dominated by any of the archive member. There are two situations for this case. One situation is that the child shares the same \mathbf{B} vector with an archive member, i.e., they belong to the same hyper-box. Then we first check their relations in the usual non-domination sense. If the child dominates the archive member or the child is non-dominated to the archive member, but is closer to the \mathbf{B} vector in terms of Euclidean distance than the archive member, then the child is retained. Solutions 1 and 2 in Figure 5-4 belong to this situation. They are in the same hyper-box (have the same \mathbf{B}), and they are non-dominated based on the definition of usual-dominance. Since solution 1 has a smaller distance to the \mathbf{B} vector, it is kept and solution 2 is deleted. The other situation is that the child does not share the same vector with any archive member. Then the child is selected into the Pareto frontier archive.

As for the population, we here use a different technique. Again, we compare the child with all the population member one by one. If the child dominates one or more population members in the usual-dominance sense, then the child replaces one of them (chosen by random). If the child dominates nobody, then the child is deleted. When both of the above two cases fail, the child replaces a randomly chosen member since the child is non-dominated to the population members.

In the update of the Pareto frontier archive and the population, if the child is not accepted, then we go back to step 3 to regenerate the child.

By applying the above two techniques, we can guarantee a fixed size for the population and a bound size of the Pareto frontier archive. In addition, the ϵ -dominance concept helps ensure a well-distributed frontier.

7. Repeat from step 3 to step 6

The above procedure from step 3 to step 6 is repeated for a specified number of iterations. The optimization stops when enough number of children designs are created. The current archive of nondominated designs represents the final estimate for the true Pareto Frontier. We can also compare the development of Pareto frontier during the final cycles. If the Pareto frontier changes little, we can stop the optimization.

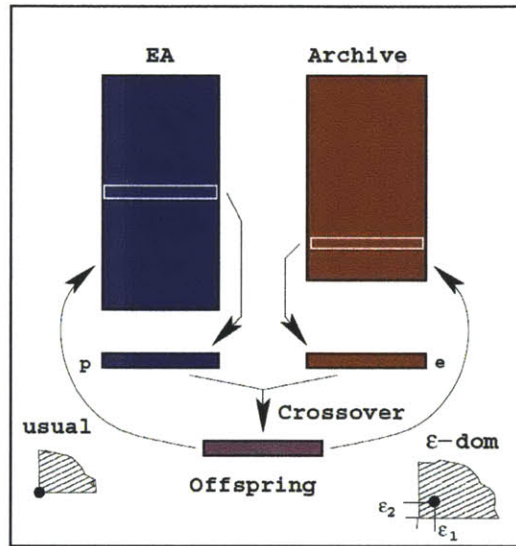


Figure 5-6: Illustration of the procedure of ϵ -MOEA (from Deb et al., 2003)

8. Determine the Final Result

There are several choices in the final Pareto frontier archive. They are all the optimal solutions theoretically. Therefore, it is our job to make the trade-off among them to make the final decision.

To sum up, the whole procedure of this ϵ -MOEA is indicated in Figure 5-6.

5.5 Final hull shape for the mini-platform

In our study, we start with an initial population of 200 cases, and do the optimization until the total number of the population reaches 350. A good variety of initial designs

has been created to guarantee that the process will not converge to a single design at last. The Pareto frontier for the population of 350 is shown in Figure 5-7.

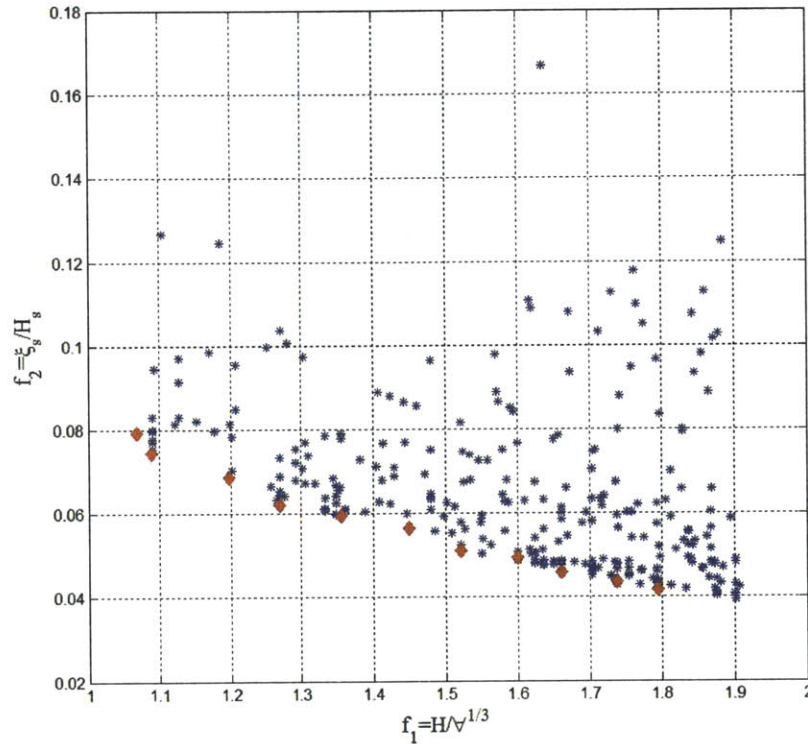


Figure 5-7: Final Pareto frontier of the Multi-objective optimization for the hull shape of the mini-platform when the population number reaches 350. The objective functions are evaluated based on the combination of WAMIT and DVRM.

As expected, there are more than one design falling into the Pareto frontier, and these optimal designs are well-spread. Here a few selected shapes are presented in Figure 5-8 and Table 5.5.

- Design 98 minimizes the first objective with a total draft of 25.12 m. Such a shallow draft can help reduce the cost for construction and installation. However, just because of such a small draft with a relatively large water-plane area, this design suffers a relatively large wave exciting force and a relatively large natural frequency. Hence it does not behave well in the second objective.
- Design 114, on the other hand, features the smallest heave response in the

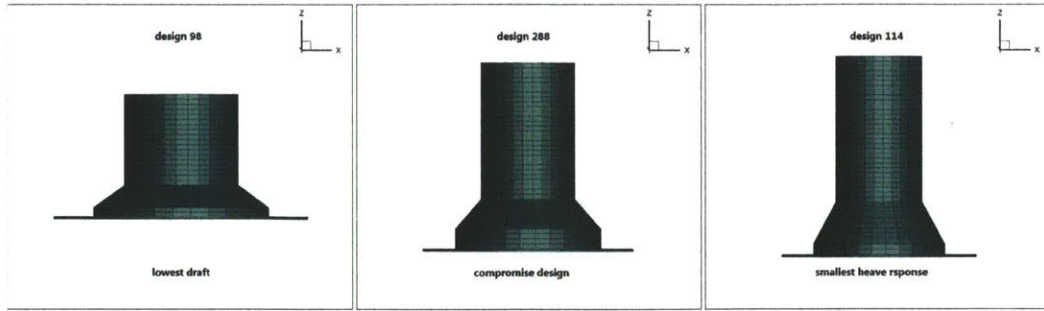


Figure 5-8: Hull shape of the selected designs from the final Pareto frontier of a population of 350.

Design	98	288	114
Draft $f_1 = H$ (m)	25.12	37.6	42.19
Heave response $f_2 = \xi_s$ (m)	0.9512	0.5926	0.5010
R_1 (m)	11.64	9.35	9.03
R_2 (m)	17.90	14.54	13.82
R_3 (m)	25.92	21.07	20.49
H_1 (m)	18.67	27.51	31.00
H_2 (m)	4.61	6.06	8.98
H_3 (m)	1.84	4.05	2.22
GM (m)	1.37	1.86	2.66
T_n (s)	21.4	21.7	22.1

Table 5.2: Dimensions and optimization objectives of the selected designs of the mini-platforms from the final Pareto frontier of a population of 350.

survival sea-state. But its draft is also deepest among these three selected designs. This again validates the contradictory of the two objectives.

- Finally, design 288 is represented as a compromised candidate. It has a moderate draft of 37.6 m and a natural period of 21.7 s. Its heave motion response is also satisfactory.

We can also see that all these optimal results have a relatively low shoulder with radius ratios around 1.5. This is consistent with the expectation in the parameter analysis in Chapter 4 (see Chapter 4, section 4.3).

However, due to the limited time, we stop the optimization when only 150 children are produced. The pareto frontier could be pushed forward further. A sensitivity test

needs to be conducted to see whether the Pareto frontier would change much as the population grows. In addition, here we do not consider the performance of the designs in pitch motion. In future work, we can also include the pitch motion as another optimization objective.

Chapter 6

Summary and Recommendations

6.1 Summary

Due to a large number of marginal oil fields discovered in Gulf of Mexico, and the high cost of the existing floaters, oil companies hope to seek for a design of a novel miniature floating platform with loose mooring systems. To be more specifically, the displacement for such a design should be around 10,000 ton to reduce the cost in construction and installation. In addition, the platform should behave well in hydrodynamic motion in waves. It is challenging to achieve the both goals at the same time. This thesis presents the procedure of the novel design and related models involved.

In Chapter 2, we discuss in details some necessary preliminary considerations for the design. This includes the estimation of the weight distribution, the main dimensions, the centre of gravity and radius of gyration. All of these are based on the standard codes and rules, and also consistent with the statistics of the existing miniature platforms. Such estimations provide a general frame for the following calculations.

For a concept design, we focus on the hydrodynamic performance of the platform. Therefore, Chapter 3 is mainly concerned with the hydrodynamic models and numerical methods involved in the calculation of the motion of a floating body in waves. Based on the equation of motion, this problem can be decomposed into two

sub-problems. One is the well-known wave-body radiation/diffraction problem. This sub-problem assumes the fluid to be completely inviscid, incompressible and irrotational. Therefore, the potential flow model is used to obtain the linear hydrodynamic coefficients in the motion equation. In this thesis, the standard 3D panel code WAMIT is adopted. The other sub-problem which involves the viscous effects, however, has not been well solved yet nowadays. Therefore, we develop a new model called Discrete Vortex Ring Model (DVRM) which can efficiently and accurately estimate the viscous drag coefficient. Such an efficiency in the calculations is appreciated in the following optimization. After obtaining all the hydrodynamic coefficients in the motion equation, we solve for the response of a floating body in regular waves in the combination of WAMIT and DVRM. The later part of Chapter 3 presents the derivation of the solution for a modified response amplitude operator (RAO) with viscous effects included. The prediction of the response of a floating body in irregular waves based on this modified RAO is also given.

Chapter 4 concentrates on applying the models and methods presented in Chapter 3 to the design of our mini-platform. We first qualitatively discuss the evolution of the hull shape of our platform on the basis of a spar with a fixed displacement and draft. The potential theory model is mainly used for this qualitative analysis, and a basic shape for our platform is obtained. Then we provide an example of an initial design of our platform, compared with the basis spar in the heave motion quantitatively in the combination of WAMIT and DVRM. The comparison shows that our platform behaves better in heave compared with the spar with the same displacement. It also shows the feasibility of our combined model between WAMIT and DVRM. Finally, we utilize this combined model to investigate the influence of different geometric parameters of the mini-platform on the heave motion, providing some expectations for the optimal designs.

In Chapter 5, we present how to integrate our combined model into an automatic optimization framework to obtain the optimal design of the hull form. A so-called ϵ -MOEA algorithm is used to solve the constrained multi-objective optimization problem. Finally, a compromised design with a moderate draft, a satisfactory motion

performance in waves and a small displacement of 13,000 ton is obtained.

6.2 Recommendations

The following are the recommendations that need to be further investigated in order to further improve the design of the effective mini-platform.

- For the DVRM, in this thesis, we only consider an infinitely thin circular plate for simplicity. We do not consider the effect of the hull on the plate. In the future, we can extend this model to a body with a disk to obtain a more accurate vortex induced drag coefficient.
- As discussed in Chapter 5, we stop the optimization when there are 350 cases in total. We do not examine the stability of the Pareto frontier obtained based on these 350 cases. A sensitivity test is required to see how much the Pareto frontier can be further pushed as the number of the optimization population grows.
- The whole thesis places the emphasis on the heave motion of the platform, but the pitch motion behaviour is not examined. In the future work, we should include this part into the analysis and optimization, to obtain a more reliable design.
- As mentioned in Chapter 2, there is a moonpool in the hull of our mini-platform. However, when we calculate the motion response for our platform, we do not take into account the effect of the moonpool. The effect of moonpool on the platform motion in waves should be examined.
- Nonlinear effects should also be examined. These include the mooring effects, Mathew instability, wave slamming, vortex-induced vibration (VIV) and wave-current interaction.

Bibliography

- [1] Christopher M. Barton. An overview of offshore concepts.
- [2] PW Bearman. Vortex shedding from oscillating bluff bodies. *Annual Review of Fluid Mechanics*, 16(1):195–222, 1984.
- [3] Robert F Beck. Time-domain computations for floating bodies. *Applied ocean research*, 16(5):267–282, 1994.
- [4] L. Birk and G.F. Clauss. Optimization of offshore structures based on linear analysis of wave-body interaction. pages 275–289.
- [5] L. Birk, G.F. Clauss, and J.Y. Lee. Practical application of global optimization to the design of offshore structures.
- [6] Lothar Birk. application of constraint multi objective optimization to the design of offshore structure hulls. 2007.
- [7] C.E. Brown and W.H. Michael Jr. On slender delta wings with leading-edge separation. 1955.
- [8] CA Cermelli, DG Roddier, and CC Busso. Minifloat: A novel concept of minimal floating platform for marginal field development.
- [9] Subrata Chakrabarti. *Handbook of Offshore Engineering (2-volume set)*. Elsevier Science, 2005.
- [10] GF Clauss and L. Birk. Hydrodynamic shape optimization of large offshore structures. *Applied ocean research*, 18(4):157–171, 1996.
- [11] H. Cozijn, R. Uittenbogaard, and E. ter Brake. Heave, roll and pitch damping of a deepwater calm buoy with a skirt.
- [12] B. De Bernardinis, JMR Graham, and KH Parker. Oscillatory flow around disks and through orifices. *Journal of Fluid Mechanics*, 102(1):279–299, 1981.
- [13] Kalyanmoy Deb, Manikanth Mohan, and Shikhar Mishra. A fast multi-objective evolutionary algorithm for finding well-spread pareto-optimal solutions. *KanGAL report*, 2003002, 2003.

- [14] Douglas G Dommermuth and Dick KP Yue. High-order spectral method for the study of nonlinear gravity waves. *Journal of Fluid Mechanics*, 184(1):267–288, 1987.
- [15] Odd M Faltinsen and M Chezhian. A generalized wagner method for three-dimensional slamming. *Journal of ship research*, 49(4):279–287, 2005.
- [16] Odd M Faltinsen and Bjrn Sortland. Slow drift eddy making damping of a ship. *Applied ocean research*, 9(1):37–46, 1987.
- [17] OM Faltinsen. Wave loads on offshore structures. *Annual review of fluid mechanics*, 22(1):35–56, 1990.
- [18] O.M. Faltinsen. *Sea loads on ships and offshore structures*, volume 1. Cambridge Univ Pr, 1993.
- [19] JMR Graham. Vortex shedding from sharp edges. 1977.
- [20] JMR Graham. The forces on sharp-edged cylinders in oscillatory flow at low keuleganarpenter numbers. *Journal of Fluid Mechanics*, 97(02):331–346, 1980.
- [21] H. Haslum and O. Faltinsen. Alternative shape of spar platforms for use in hostile areas.
- [22] H. He, A.W. Troesch, and M. Perlin. Hydrodynamics of damping plates at small kc numbers. pages 93–104. Springer.
- [23] John L Hess and AM Smith. 0.,” calculation of potential flow about arbitrary bodies,” progress in aeronautical sciences, vol. 8, 1966.
- [24] TY Hou, VG Stredie, and T.Y. Wu. A 3d numerical method for studying vortex formation behind a moving plate. *Communications in Computational Physics*, 1(2):207–228, 2006.
- [25] Yifeng Huang. *Nonlinear ship motions by a Rankine panel method*. PhD thesis, 1997.
- [26] W. Hudson and J. Vasseur. A small tension leg platform for marginal deepwater fields.
- [27] IACS. Requirements concerning mobile offshore drilling units. Technical report, 2007.
- [28] ITTC. <http://ittc.sname.org/>.
- [29] F. John. On the motion of floating bodies ii. simple harmonic motions. *Communications on pure and applied mathematics*, 3(1):45–101, 1950.
- [30] M.A. Jones. The separated flow of an inviscid fluid around a moving flat plate. *Journal of Fluid Mechanics*, 496:405–441, 2003.

- [31] G.H. Keulegan, L.H. Carpenter, United States. National Bureau of Standards, and United States. Office of Naval Research. *Forces on cylinders and plates in an oscillating fluid*. US Department of Commerce, National Bureau of Standards, 1956.
- [32] S. Kibbee, J. Chianis, K. Davies, and B. Sarwono. The seastar tension-leg platform.
- [33] S. Kibbee, S. Leverette, K. Davies, and R. Matten. Morpeth seastar mini-tlp.
- [34] S. Kibbee and D. Snell. New directions in tlp technology.
- [35] Bradley King. Time-domain analysis of wave exciting forces on ships and bodies. Technical report, University of Michigan, 1987.
- [36] J. Koon, B. Heijermans, and P. Wybro. Development of the prince field.
- [37] ROBERT KRASNY. Vortex sheet computations: Roll-up, wakes, separation. 1991.
- [38] Matthew Lake, Haiping He, Armin W Troesch, Marc Perlin, and Krish P Thiagarajan. Hydrodynamic coefficient estimation for tlp and spar structures. *Journal of Offshore Mechanics and Arctic Engineering*, 122:118, 2000.
- [39] Horace Lamb. *Hydrodynamics*. Cambridge University Press, 1993.
- [40] C.H. Lee. Wamit theory manual. 1995.
- [41] CH Lee and JN Newman. Computation of wave effects using the panel method, 2005.
- [42] B. Li and J. Ou. Concept design of a new deep draft platform. *Journal of Marine Science and Application*, pages 1–9, 2010.
- [43] Woei-Min Lin and D Yue. Numerical solutions for large-amplitude ship motions in the time domain. 1991.
- [44] Yuming Liu, Ming Xue, and Dick KP Yue. Computations of fully nonlinear three-dimensional wave-wave and wave-body interactions. part 2. nonlinear waves and forces on a body. *Journal of Fluid Mechanics*, 438:41–66, 2001.
- [45] R. Longbin Tao, Krish Thiagarajan Barreira. Low kc w regimes of oscillating sharp edges i. vortex shedding observation.
- [46] G Pawlak M Canals. Three-dimensional vortex dynamics in oscillatory flow separation. *Journal of Fluid Mechanics*, 674:408, 2011.
- [47] C.C. Mei, M. Stiassnie, and K.P.Y. Dick. *Theory and applications of ocean surface waves: linear aspects*, volume 2. World Scientific, 2005.

- [48] Walter H Michel. Sea spectra revisited. *MAR TECHNOL*, 36(4):211–227, 1999.
- [49] J Nicholas Newman. Panel methods in marine hydrodynamics. In *Proc. Conf. Eleventh Australasian Fluid Mechanics-1992*.
- [50] J.N. Newman. *Marine hydrodynamics*. The MIT press, 1977.
- [51] JN Newman. Distributions of sources and normal dipoles over a quadrilateral panel. *Journal of Engineering Mathematics*, 20(2):113–126, 1986.
- [52] JN Newman and C.H. Lee. Boundary-element methods in offshore structure analysis. *Journal of Offshore Mechanics and Arctic Engineering*, 124:81, 2002.
- [53] JN Newman and PD Scлавounos. The computation of wave loads on large offshore structures. In *Proc. Intl Conf. on the Behaviour of Offshore Structures, BOSS'8, Trondheim*.
- [54] M. Nitsche and R. Krasny. A numerical study of vortex ring formation at the edge of a circular tube. *Journal of Fluid Mechanics*, 276:139–162, 1994.
- [55] J Pawlowski. A nonlinear theory of ship motion in waves. 1994.
- [56] B. Ronalds. Deepwater facility selection.
- [57] N. Rott. Diffraction of a weak shock with vortex generation. *J. Fluid Mech*, 1(part 1), 1956.
- [58] P. Scлавounos. 2.24 ocean wave interactions with ships and offshore energy systems (lecture notes), 2013.
- [59] Manley St Denis and Willard J Pierson Jr. On the motions of ships in confused seas. Technical report, DTIC Document, 1953.
- [60] M. Stiassnie, E. Naheer, and I. Boguslavsky. Energy losses due to vortex shedding from the lower edge of a vertical plate attacked by surface waves. *Proceedings of the Royal Society of London. A. Mathematical and Physical Sciences*, 396(1810):131–142, 1984.
- [61] L. Tao and S. Cai. Heave motion suppression of a spar with a heave plate. *Ocean Engineering*, 31(5-6):669–692, 2004.
- [62] Longbin Tao and Krish Thiagarajan. Low k_c/k_i flow regimes of oscillating sharp edges. ii. hydrodynamic forces. *Applied ocean research*, 25(2):53–62, 2003.
- [63] Lindsey Wilhoit. 2010 offshore worldwide survey of tlps, tlwps. *Offshore Magazine*, 2010.
- [64] Pieter Wybro. Floating production system deepwater development option. In *MTS Field Development Workshop*.